Tbilisi State University
High Energy Physics Institute

Studies of the neutron-proton charge-exchange amplitudes at COSY using the ANKE spectrometer

Ph.D. Thesis of
David Mchedlishvili

Supervisors	Prof. Dr. M. Nioradze (TSU)
	Dr. M. Tabidze (TSU)
Advisers	Prof. Dr. H. Ströher (FZ Jülich)
	Dr. A. Kacharava (FZ Jülich)
	Dr. M. Tabidze (TSU)

Ph.D. work carried out at the Institut für Kernphysik,
Forschungszentrum Jülich GmbH, Germany
September 13, 2013

Abstract

A good understanding of the Nucleon–Nucleon interaction (NN) remains one of the most important goals of nuclear and hadronic physics. Experiments at COSY, using a polarised deuteron beam and/or target, can lead to significant improvements in the np database by studying the quasi–free reaction on the neutron in the deuteron - $dp \to \{pp\}_s n$. The impulse approximation links the observables of this reaction with those for the $np \to pn$ process.

The unpolarised differential cross section and the two deuteron tensor analysing powers A_{xx} and A_{yy} of the $\vec{d}p \to \{pp\}_s n$ charge-exchange reaction have been measured with the ANKE spectrometer at the COSY storage ring. Using deuteron beams with energies 1.2, 1.6, 1.8, and 2.27 GeV, data were obtained for small momentum transfers to a $\{pp\}$ system with low excitation energy, so that the final diproton is mainly in $^1S_0$ state. The results at the three lower energies are consistent with impulse approximation predictions based upon the current knowledge of the neutron-proton amplitudes. However, at 2.27 GeV, where these amplitudes are far more uncertain, agreement requires a reduction in the overall spin-flip contribution, with an especially significant effect in the longitudinal direction. These conclusions are supported by measurements of the deuteron-proton spin-correlation parameters $C_{x,x}$ and $C_{y,y}$ that were carried out at 1.2 and 2.27 GeV. The values obtained for the proton analysing power A_y^p also suggest the need for a radical re-evaluation of the neutron-proton elastic scattering amplitudes at the higher energy. It is therefore clear that such measurements can provide a valuable addition to the neutron-proton database in the charge-exchange region.

Experiments have extended these studies into the pion-production regime in order to investigate the excitation of the $\Delta(1232)$ isobar in the $dp \to \{pp\}_s\Delta^0$ reaction. These data have proven to provide useful information on the elementary $np \to p\Delta^0$ process.

This thesis introduces the experimental np program at ANKE/COSY, describes the facility, where the measurements were conducted, gives a detailed description of the analyses technique involved in these studies and, finally, presents the achieved physics results.

Contents

Chapter 1

Introduction

A huge progress has been made in different fields of physics, as well as in other natural sciences, in the past century. The "driving force" for this was human's curiosity, arising from the questions: "How was the world created?", "What is it made of?". The more we know about the surrounding world, the more clearly we realise that much more knowledge is necessary to explain the laws of nature and finally, answer the most important questions of the mankind.

The Big Bang theory, which managed to describe the evolution of the universe starting from a very early stage, does not give any hint about how the Big Bang was actually induced. The Standard Model, which is considered as the most advanced model nowadays, still has some deficiencies. One of these is to why there is no experimental observation of the CP violation in the strong interactions while the quantum chromodymanics does not restrict this. Another concern is the neutrino oscillation, a well observed experimental fact that can not be properly explained within the Standard Model. Furthermore, the mystery of the antimatter still remains unsolved. All these suggest that there must be physics beyond the Standard Model that needs to be explored.

In the process of searching for the solutions for the world's puzzles scientists were looking deeper and deeper into the structure of matter, and our understanding of matter was changing from molecules to atoms, from nuclei to nucleons and, finally, quarks were discovered. The nucleon-nucleon interaction appears to be a consequence of the strong interaction between quarks. Since quarks are not accessible directly, investigating the nuclear forces, we acquire knowledge about the quark-gluon interaction *i.e.* about the strong force and are preparing to make the next step towards a better understanding of the world, that surrounds us.

Apart from their intrinsic importance for the study of nuclear forces, "nucleon-nucleon" data are necessary ingredients in the modelling of meson production and other nuclear reactions at intermediate energies. The phase shift analysis is one of the main tools used here to interpret the NN observables. The SAID ('Scattering Analysis Interactive Dial-In') database and analysis program [1] have proved to be truly invaluable tools over many years for researchers working in this area. The SAID program uses NN experimental elastic scattering data in order to perform a phase shift analysis up to a certain orbital angular momentum $L_{\rm max}$ and uses a theoretical model for higher L. $L_{\rm max}$ can be increased as new significant experimental data become available. By assuming that the phase shifts vary smoothly with beam energy, predictions can be made for observables at a particular energy, where no experimental data might even exist, and it is in this way that the SAID program is most commonly used.

Clearly any amplitude analysis can only be as good as the data used in its implementation. Lots of proton-proton observables, such as differential and total cross sections, single and multi-spin observables, have been measured up to high energies and this has allowed the construction of reliable isospin $I = 1$ phase shifts up to at least $T_N \approx 2$ GeV, but our knowledge is still poor at higher energies, especially at small angles. The situation is even more serious for the isoscalar $I = 0$ case of neutron-proton scattering where very little is known above about 1 GeV and data that do exist are not necessarily very well reproduced by the SAID program. For example, the only differential cross section data for large angle np scattering [2], in the so-called charge-exchange region, seem to be consistently over-predicted in the SAID analysis. Hence, more precise experimental data on neutron-proton scattering are essential to perform reliable phase shift analysis at higher energies. The primary aim of these studies at ANKE is to provide useful experimental np data at intermediate energies.

Experiments with neutron beams are complicated due to additional problems associated with the quality of neutron beams and/or the detection of neutrons. The deuteron is often used successfully as a substitute target or beam. For example, it has been shown that the spin correlation and transfer parameters in pp quasi-elastic scattering in the 1.1 to 2.4 GeV range are very close to those measured in free pp collisions [3].

The backward amplitudes can be studied by comparing the quasi-free (p, n) or (n, p) reactions on the deuteron to the free backward elastic scattering on a nucleon target. It was suggested over 60 years ago, that the reaction on the deuteron, is suitable kinematic region, could be used as a spin filter that selects the spin-dependent contribution to the np elastic cross section [4]. This sensitivity arises from the Pauli principle, which blocks any spin-1 component in the low energy nn or pp system. Using this, Bugg and Wilkin developed a single scattering (impulse) approximation methodology for the $(d, 2p)$ reaction and linked the observables of this reaction with those for backward or so called charge-exchange np-elastic amplitudes [5].

This thesis is devoted to the study of the $dp \to \{pp\}_s n$ reaction spin observables at different energies that, together with existing pp elastic scattering data, give valuable information about the np elastic amplitudes at large angles.

Chapter 2

Neutron-proton database

Experiments providing useful data on neutron-proton scattering that have been carried out up to now, together with achieved results, are described in detail in Ref. [6]. Unfortunately, not all of these experimental data (relatively older) are implemented in phase shift analyses (PSA). However, other data provide a useful check of PSA solutions. These data are summarised in this chapter and also the comparison with SAID phase shift analysis is demonstrated for different observables.

2.1 Unpolarised observables

The charge-exchange of neutrons or protons on the deuteron has a very long history. Apart from Coulomb effects, by charge symmetry the cross section for $d(n,p)$ and $d(p,n)$ reactions should be identical. The proton and neutron bound in the deuteron are in a superposition of $^3S_1$ and $^3D_1$ states with parallely aligned spins. On the other hand, if the four-momentum transfer $t = -q^2$ between the incident neutron and final proton in the $nd \to p\{nn\}$ reaction is very small, due to the Pauli principle, the two emerging neutrons are required to be in the spin-singlet states $^1S_0$ and $^1D_2$. In impulse (single-scattering) approximation the transition amplitude is expected to be proportional to a spin-flip isospin-flip nucleon-nucleon scattering amplitude times a form factor, representing the overlap of the initial spin-triplet deuteron wave function with that of the unbound (scattering-state) nn wave function.

The energy spectrum of the proton from the $d(n,p)nn$ reaction would clearly depend upon the deuteron and nn wave functions, *i.e.*, upon low energy nuclear physics. However, Dean showed that, if one integrated over all the proton energies, there was a closure sum rule where all the dependence on the nn wave function vanished [7].

$$\left(\frac{d\sigma}{dt}\right)_{nd\to p\{nn\}} = [1 - F(q)]\left(\frac{d\sigma}{dt}\right)^{\mathrm{SI}}_{np\to pn} + [1 - \tfrac{1}{3}F(q)]\left(\frac{d\sigma}{dt}\right)^{\mathrm{SF}}_{np\to pn}, \tag{2.1}$$

where $F(q)$ is the deuteron form factor. Here the neutron-proton differential cross section consists of two parts. The first part corresponds to the contribution that is independent of any spin transfer (SI) between the initial neutron and final proton and the second one to a spin flip (SF).

When the beam energy is high enough, then in the forward direction $q \approx 0$, $F(0) = 1$, and Eq. (2.1) reduces to

$$\left(\frac{d\sigma}{dt}\right)_{nd\to p\{nn\}} = \frac{2}{3}\left(\frac{d\sigma}{dt}\right)^{\mathrm{SF}}_{np\to pn}. \tag{2.2}$$

There are modifications to Eq. (2.1) through the deuteron D-state though these do not affect the forward limit of Eq. (2.2) [7, 5]. As a consequence, the ratio

$$R_{np}(0) = \left(\frac{d\sigma}{dt}\right)_{nd\to p\{nn\}} \Bigg/ \left(\frac{d\sigma}{dt}\right)_{np\to pn} = \frac{2}{3}\left(\frac{d\sigma}{dt}\right)^{\mathrm{SF}}_{np\to pn} \Bigg/ \left(\frac{d\sigma}{dt}\right)_{np\to pn} \tag{2.3}$$

should be to two thirds of the fraction of spin flip in $np \to pn$ between the incident neutron and proton outgoing in the beam direction. Hence, the ratio of two unpolarised cross sections can give information about the spin dependence of neutron-proton scattering. Due to this, many groups have made experimental studies in this direction, starting from very low energies and extending up to 2 GeV [8]. Note that such an interpretation of the cross section ratio is useful when the energy is sufficiently high for the Dean sum rule to converge before any phase space limitations become important. The longitudinal momentum transfer must be negligible and terms other than the $np \to pn$ impulse approximation should not contribute significantly to the evaluation of the sum rule. Although the strong NN FSI helps with these concerns, all the caveats indicate that Eq. (2.3) would provide at best only a qualitative description of data at the lower energies.

Alternatively, one can measure the excitation energy (E_{pp}) in the outgoing dineutron or diproton with good resolution and then evaluate the impulse approximation directly by using deuteron and NN scattering wave functions. This avoids problems with convergence of the sum rule and so might provide useful results down to lower energies. A second important feature of the $d(p,n)pp$ reaction in these conditions is that the polarisation transfer between the initial proton and the final neutron is expected to be very large.

Bugg and Wilkin [5, 9] showed that, in the small E_{pp} limit, the deuteron tensor analysing powers in the $p(\vec{d},\{pp\})n$ reaction should also be large and sensitive to the differences between the neutron-proton spin-flip amplitudes. This realisation provided an impetus for the study of high resolution $p(\vec{d},\{pp\})n$ experiments.

2.2 Unpolarised data

Data are available on the R_{np} and R_{pn} parameters in, respectively, inclusive $d(n,p)nn$ and $d(p,n)pp$ reactions at energies that range from tens of MeV up to 2 GeV, while polarisation transfer data are well investigated only up to 800 MeV.

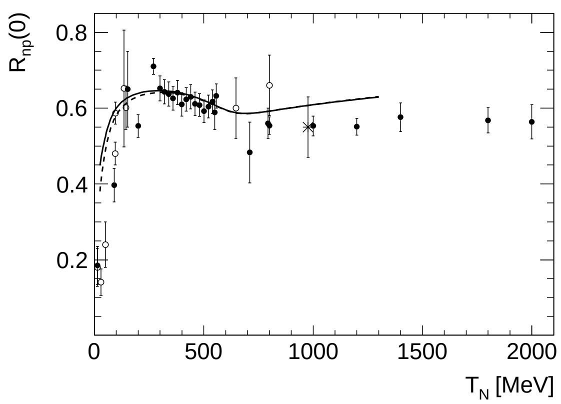

Figure 2.1: Experimental data on the $R_{np}(0)$ ratio taken in the forward direction. The closed circles are from the (n,p) data, the open circles from the (p,n) data, and the cross from the $(d,2p)$ datum. These results are compared to the predictions of Eq. (2.6) using the current SAID solution [1], which is available up to a laboratory kinetic energy of 1.3 GeV. The dashed curve takes into account the limited phase space available at the lower energies.

Four experimental programmes have been devoted to the study of the cross section and tensor analysing powers of the $p(\vec{d},\{pp\})n$ reaction using very different experimental techniques. In general impulse approximation gives a reasonable description of the data out to a three-momentum transfer of $q \approx m_\pi$ by which point multiple scatterings might become important. These data are however only available in an energy domain where the neutron-proton database is extensive and reliable.

The values of $R_{np}(0)$ and $R_{pn}(0)$ from different experiments are shown in Fig. 2.1. These data are compared with predictions from the current GW/VPI [10] phase shift analysis obtained on the basis of Eq. (2.6). They are also shown in Fig. 2.1 up to the limit of their validity at 1.3 GeV. At low energies the spin-independent contribution dominates and the $R_{np}(0)$ ratio gets small, as indicated by the phase shift predictions. A dashed curve shows a slight effect from limited phase space. A much more important effect is the cut in the experimental data analysis, put onto the emerging neutron or proton in order to isolate the charge-exchange contribution from that of other mechanisms. At low energies this procedure becomes far more ambiguous, because relatively severe cuts have to be imposed.

The data in Fig. 2.1 seem to be largest at around the lowest PSI point [11], which is very close to the allowed limit of 0.67. In fact, if the Glauber shadowing effect is taken into account [12], this limit might be reduced to perhaps 0.63. As phase shift analysis show, the contribution from the spin-independent term is very small in this region. On the other hand, in the region from 1.0 to 1.3 GeV the phase shift curve lies systematically above the experimental data. Since the conditions for the Dean sum rule seem to be best satisfied at high energies, this suggests that the SAID solution underestimates the spin-independent contribution above 1 GeV. It has to be noted that the experimental *np* database is far less rich in this region.

2.3 Polarised observables

An input necessary for the evaluation of the forward charge exchange observables can be expressed as combinations of *pure* linearly independent $np \to np$ observables evaluated in the backward direction [13]. The NN formalism gives two series of polarisation transfer parameters that are mutually dependent [14]. If the polarisation is transferred from the beam (b) to recoil (r) particles, or from the target (t) to the scattered (s) particle, then

$$\begin{aligned}
\frac{d\sigma}{dt}K_{0rb0} &= \frac{1}{4}Tr\left\{\sigma_{2r}M\sigma_{1b}M^{\dagger}\right\},\\
\frac{d\sigma}{dt}K_{s00t} &= \frac{1}{4}Tr\left\{\sigma_{1s}M\sigma_{2t}M^{\dagger}\right\}.
\end{aligned} \tag{2.4}$$

Here σ_{1s}, σ_{1b}, σ_{2t}, and σ_{2r} are the corresponding Pauli matrices and M is the scattering matrix. The unpolarised invariant elastic scattering cross section

$$\frac{d\sigma}{dt} = \frac{\pi}{k^2}\frac{d\sigma}{d\Omega} = \frac{1}{4}Tr\left\{MM^{\dagger}\right\}, \tag{2.5}$$

where k is the momentum in the CM frame and $t = -q^2$ is the four-momentum transfer.

A first series of parameters describes the scattering of a polarised neutron beam on an unpolarised proton target, where the polarisation of the final outgoing protons is measured by an analyser through a second scattering. The spins of the incident neutrons can be oriented either perpendicularly or longitudinally with respect to the beam direction and the final proton polarisations are measured in the same directions. At $\theta_{\mathrm{CM}} = \pi$ there are two independent parameters, $K_{0nn0}(\pi)$ and $K_{0ll0}(\pi)$, referring respectively to the transverse (n) and longitudinal (l) directions. It was shown in Ref. [13] that the forward $d(n,p)n/p(n,p)n$ cross section ratio can be written in terms of these as

$$R_{np}(0) = \frac{1}{6}\left\{3 - 2K_{0nn0}(\pi) - K_{0ll0}(\pi)\right\}. \tag{2.6}$$

A second series of parameters describes the scattering of an unpolarised neutron beam on a polarised proton target, where it is the polarisation of the final outgoing neutron that is determined. This leads to the alternative expression for $R_{pn}(0)$:

$$R_{np}(0) = \frac{1}{6}\left\{3 - 2K_{n00n}(\pi) + K_{l00l}(\pi)\right\}, \tag{2.7}$$

where $K_{n00n}(\pi) = K_{0nn0}(\pi)$ but $K_{l00l}(\pi) = -K_{0ll0}(\pi)$.

In plane wave impulse approximation, the one non-vanishing deuteron tensor analysing power in the $p(d,\{pp\})n$ reaction in the forward direction, assuming that the excitation energy in the pp system is very small such that it is in the $^1S_0$ state [5, 13], can be expressed in terms of the same spin-transfer parameters:

$$A_{NN}(0) = \frac{2(K_{0ll0}(\pi) - K_{0nn0}(\pi))}{3 - K_{0ll0}(\pi) - 2K_{0nn0}(\pi)}\,. \tag{2.8}$$

From now on the nucleon-deuteron observables will be labelled with capital letters and only carry two subscripts.

In the same approximation, the longitudinal and transverse spin-transfer parameters between the initial proton and the final neutron in the $d(\vec{p},\vec{n})pp$ are similarly given by

$$\begin{aligned} K_{LL}(0) &= -\left[\frac{1 - 3K_{0ll0}(\pi) + 2K_{0nn0}(\pi)}{3 - K_{0ll0}(\pi) - 2K_{0nn0}(\pi)}\right], \\ K_{NN}(0) &= -\left[\frac{1 + K_{0ll0}(\pi) - 2K_{0nn0}(\pi)}{3 - K_{0ll0}(\pi) - 2K_{0nn0}(\pi)}\right]. \end{aligned} \tag{2.9}$$

Independent of any theoretical model, these parameters are related by [15, 16]

$$K_{LL}(0) + 2K_{NN}(0) = -1. \tag{2.10}$$

Equally generally, in the $^1S_0$ limit the forward longitudinal and transverse deuteron tensor analysing powers are trivially related;

$$A_{LL}(0) = -2A_{NN}(0). \tag{2.11}$$

These are then connected to the spin-transfer coefficients through [16]

$$A_{LL}(0) = -(1 + 3K_{LL}(0))/2 \qquad \text{or} \qquad A_{NN}(0) = -(1 + 3K_{NN}(0))/2. \tag{2.12}$$

Note that the model-independent equations (2.10), (2.11), and (2.12) are exact if the final *pp* system is in the $^1S_0$ state.

The variation of the *np* backward elastic cross section with energy and the values of $R_{np}(0)$, $A_{NN}(0)$, and $K_{LL}(0)$ have been calculated using the energy dependent GW/VPI PSA solution SP07 [1]. The relations between the observables used in Refs. [1] and [14] are to be found in the SAID program.

The GW/VPI PSA for proton-proton scattering predictions, according to the authors, are at best qualitative below 2.5 GeV [1]. Besides, one cannot use the SAID program to estimate the errors of any observable. Although the equivalent

PSA for neutron-proton scattering was carried out up to 1.3 GeV, very few spin-dependent observables have been measured above 1.1 GeV.

2.4 Polarised data

The values of $K_{NN}(0)$ and $K_{LL}(0)$ measured in various experiments are presented in Fig. 2.2. The results are compared with the predictions of the pure ${}^1S_0$ plane wave impulse approximation of Eq. (2.9) that used the SAID phase shifts [1] as input. Wherever possible the data are extrapolated to $E_{pp} = 0$. This is especially important at low energies and, if this causes uncertainties or there are doubts in the calibration standards, such data are indicated with open symbols.

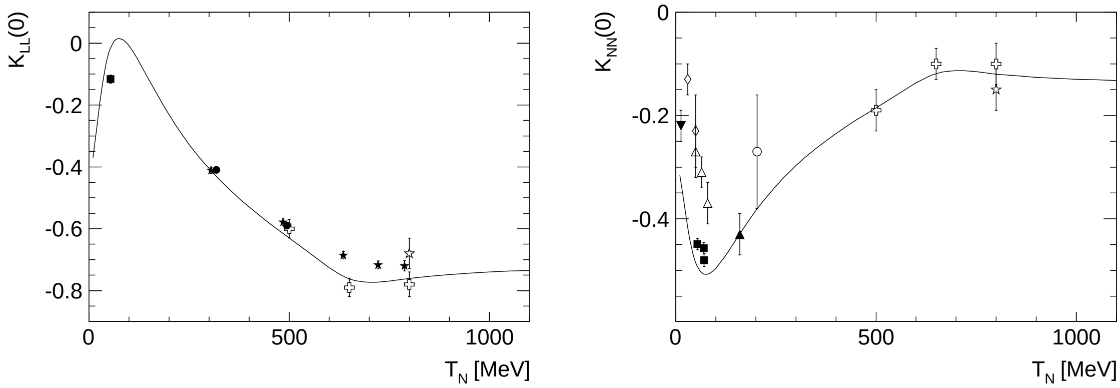

Figure 2.2: Forward values of the longitudinal and transverse polarisation transfer parameters $K_{LL}(0)$ and $K_{NN}(0)$ in the $d(\vec{p},\vec{n})pp$ reaction as functions of the proton kinetic energy T_N. Data of greater confidence, which are from Refs. [17] (stars), [18] (circles), [19] (triangle), [20, 21] (squares), and the average of the five TUNL low energy points [22] (inverted triangle) are represented by closed symbols. The open symbols corresponds to Refs. [23] (diamonds), [24] (triangle), [25] (circle), [26] (crosses), and [27] (star). The curve is the plane wave ${}^1S_0$ prediction of Eq. (2.8).

The description of the data by the impulse approximation curve is semi-quantitative, especially for the more "reliable" results. At high energies this approach is expected to perform better but it is probably significant that the curve falls below the McNaughton *et al.* results [17] in the 500 to 800 MeV range. The Glauber correction [12, 5] is not expected to be a solution to make up this difference. Therefore, this suggests that the current values of the SAID neutron-proton charge-exchange amplitudes [1] might require some slight modifications in this energy region. Similar evidence is found from the measurements of the deuteron analysing power, to which we now turn.

It was already demonstrated through Eq. (2.12) that in the $^1S_0$ limit the deuteron $(\vec{d}, 2p)$ tensor analysing power in the forward direction can be directly evaluated in terms of the $(\vec{p}, \vec{n})$ polarisation transfer coefficient. Therefore, instead of measuring beam and recoil polarisations, much of the same physics can be investigated by measuring the analysing powers with a polarised deuteron beam without any need to detect the polarisation of the final particles. This is the approach advocated by Bugg and Wilkin [9, 5]. One of the benefits in this case is that one does not need a large acceptance detector, because only a small part of the $p(\vec{d}, 2p)n$ final phase space, where E_{pp} is at most a few MeV, needs to be recorded. Four separate groups have undertaken major programmes using different electronic equipment.

In Fig. 2.3 the experimental values of the deuteron tensor analysing power in the $\vec{d}p \to \{pp\}n$ reaction extrapolated to the forward direction are shown. The error bars include some attempt to take into account the uncertainty in the angular extrapolation. The excitation energy in the final diproton in all experiments is below 1 MeV [28, 29, 30, 31] so that it is in the $^1S_0$ state. In such conditions the plane wave impulse approximation predictions of Eq. (2.8) in the forward direction should be quite reliable. The description the experimental data is better in regions where the neutron-proton phase shifts are well determined.

The values of A_{NN} deduced using Eq. (2.12) from some of the $d(\vec{p}, \vec{n})pp$ measurements are also shown in Fig. 2.3. The consistency between the $(\vec{d}, pp)$ and $(\vec{p}, \vec{n})$ data is striking and it is interesting to note that they both suggest values of A_{NN} that are slightly lower in magnitude at high energies than those predicted by the np phase shifts of the SAID group [1]. The challenge now is to continue measuring these data in the range of even higher energies, where much less is known.

Let us summarise the present status of the np database at intermediate energies. About 2000 spin-dependent np elastic scattering data points were determined at SATURNE over large angular intervals mainly between 0.8 and 1.1 GeV [33, 34]. A comparable amount of np data in the region from 0.5 to 0.8 GeV was measured at LAMPF [35] and in the energy interval from 0.2 to 0.56 GeV at PSI [36]. The TRIUMF group also contributed significantly up to 0.515 GeV [37]. Except for these, none of the $R_{np}(0)$ nor the analysing power data presented here have so far been included in any of the existing phase shift analyses.

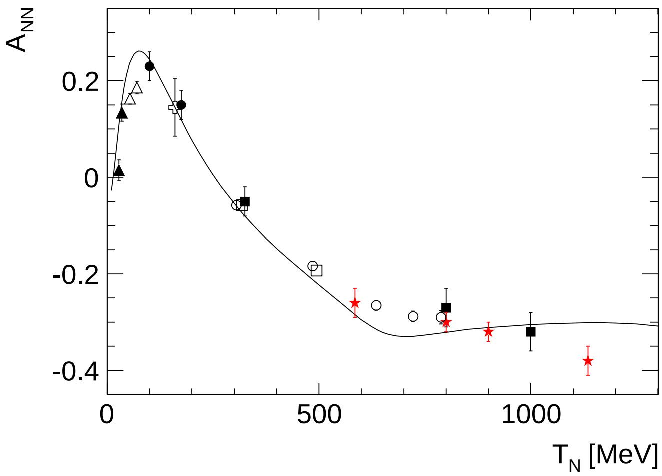

Figure 2.3: Forward values of the deuteron tensor analysing power in the $\vec{d}p \to \{pp\}n$ reaction as a function of the kinetic energy per nucleon T_N. The directly measured experimental data (closed symbols) from SPES IV (squares) [28], EMRIC (closed circles) [30], ANKE (stars) [31, 32], and RCNP (triangles) [29] were all obtained with a pp excitation energy of 1 MeV or less. The error bars include some estimate of the uncertainty in the extrapolation to $\theta = 0$. The open symbols were obtained from measured values of the polarisation transfer parameter in $d(\vec{p},\vec{n})pp$ by using Eq. (2.12). The data are from Refs. [17] (circles), [18] (squares), [19] (cross), and [20, 21] (triangles). The curve is the plane wave $^1S_0$ prediction of Eq. (2.8).

The SATURNE and the PSI data were together sufficient to implement the PSA procedure and even perform a direct amplitude reconstruction at several energies and angles. The existing spin-dependent intermediate energy data are more or less sufficient for this procedure only up to 0.8 GeV, while there is a lack of np differential cross section data at higher energies, mainly at intermediate angles. In addition, very little is known about np spin observables above 0.8 GeV.

Chapter 3

Deuteron charge-exchange on hydrogen

Deuteron-proton charge-exchange reaction can be employed to investigate different spin observables of the $np \to pn$ charge-exchange reaction. In the impulse approximation, when the momentum transfer between incident neutron and target proton is low, two fast protons emerge in the forward direction (small polar angles). By choosing the pp pairs with very small relative momenta, only the transitions from spin-triplet states of the deuteron to spin-singlet states of the diproton are selected. The data are thus sensitive to spin-flip, isospin-flip transitions and provide valuable information about the spin-dependent np charge-exchange amplitudes. Together with the pp elastic data, these will allow the reconstruction of the $I = 0$ elastic amplitudes. This chapter gives a theoretical description of the $dp \to \{pp\}_s n$ reaction in the impulse approximation and demonstrates the connection between the dp and np observables. The impulse approximation methodology has been checked experimentally at ANKE, which proved this to be a valuable tool for the np amplitude studies. The main achievements of this experiment are presented at the end of the chapter.

3.1 The $dp \to \{pp\}_s n$ reaction in impulse approximation

The elementary $np \to pn$ charge-exchange amplitude may be written in terms of five scalar amplitudes in the cm system as

$$\begin{aligned} f_{np} &= \alpha(q) + i\gamma(q)(\vec{\sigma}_1 + \vec{\sigma}_2)\cdot\vec{n} + \beta(q)(\vec{\sigma}_1\cdot\mathbf{n})(\vec{\sigma}_2\cdot\vec{n}) \\ &+ \delta(q)(\vec{\sigma}_1\cdot\vec{m})(\vec{\sigma}_2\cdot\vec{m}) + \varepsilon(q)(\vec{\sigma}_1\cdot\vec{l})(\vec{\sigma}_2\cdot\vec{l}), \end{aligned} \tag{3.1}$$

where q is the three-momentum transfer and 2×2 Pauli matrices $\vec{\sigma}$ are sandwiched between neutron and proton spinors. α, β, δ, γ and ε are complex invariant amplitudes, which are functions of energy and momentum transfer q. Here α is the spin-independent amplitude between the initial neutron and final proton, γ is a spin-orbit contribution, and β, δ, and ε are three spin-spin terms.

The orthogonal unit vectors used in Eq. (3.1) are defined in terms of the initial neutron ($\vec{k}_i$) and final proton ($\vec{k}_f$) cm momenta;

$$\vec{n} = \frac{\vec{k}_i\times\vec{k}_f}{|\vec{k}_i\times\vec{k}_f|}\,,\quad \vec{m} = \frac{\vec{k}_f - \vec{k}_i}{|\vec{k}_f - \vec{k}_i|}\,,\quad \vec{l} = \frac{\vec{k}_f + \vec{k}_i}{|\vec{k}_f + \vec{k}_i|}\,. \tag{3.2}$$

There are three spin-correlated total cross-sections defined by

$$\sigma_{tot} = \sigma_0 - \tfrac{1}{2}\Delta\sigma_L P_n^L P_p^L - \tfrac{1}{2}\Delta\sigma_T \vec{P}_n^T\cdot\vec{P}_p^T\,, \tag{3.3}$$

where P^L and $\vec{P}^T$ are the longitudinal and transverse components of the polarisation of either the initial neutron or proton. In the forward direction, when $q\approx 0$, $\beta(0) = \delta(0)$ and the following relations between the imaginary parts of the amplitudes and total cross sections hold:

$$\begin{aligned} \Im[\alpha(0)] &= \frac{1}{4\sqrt{\pi}}(\sigma_0(np) - \sigma_0(pp)), \\ \Im[\beta(0)] &= -\frac{1}{8\sqrt{\pi}}(\Delta\sigma_T(np) - \Delta\sigma_T(pp)), \\ \Im[\varepsilon(0)] &= \frac{1}{8\sqrt{\pi}}(\Delta\sigma_L(np) - \Delta\sigma_L(pp)). \end{aligned} \tag{3.4}$$

The magnitudes of the charge-exchange amplitudes in the forward direction are given in terms of the backward elastic np differential cross section and spin-transfer parameters K_{0nn0} and K_{0ll0}, which we have already introduced in chapter 2, through

$$\begin{aligned}
|\alpha(0)|^2 &= \tfrac{1}{4}[1 + 2K_{0nn0}(\pi) + K_{0ll0}(\pi)]\left(\frac{d\sigma}{dt}\right)_{np\to np}, \\
|\beta(0)|^2 &= \tfrac{1}{4}[1 - K_{0ll0}(\pi)]\left(\frac{d\sigma}{dt}\right)_{np\to np}, \\
|\varepsilon(0)|^2 &= \tfrac{1}{4}[1 - 2K_{0nn0}(\pi) + K_{0ll0}(\pi)]\left(\frac{d\sigma}{dt}\right)_{np\to np}.
\end{aligned} \tag{3.5}$$

and the cross section ratio is then

$$R_{np}(0) = \left.\frac{\mathrm{d}\sigma(nd \to pnn)/\mathrm{dt}}{\mathrm{d}\sigma(np \to pn)/\mathrm{dt}}\right|_{q=0} = \frac{2}{3}\frac{2|\beta(0)|^2 + |\varepsilon(0)|^2}{|\alpha(0)|^2 + 2|\beta(0)|^2 + |\varepsilon(0)|^2}. \tag{3.6}$$

In the single-scattering (impulse) approximation, the $dp \to \{pp\}_s n$ charge-exchange reaction on proton is thought of as a $np \to pn$ reaction with a spectator proton. Initially the neutron-proton pair is bound in the deuteron and the two emerging protons are subject to a final-state interaction. This is illustrated diagrammatically in Fig. 3.1. If the relative momentum $\vec{k}$, and hence the excitation energy $E_{pp} = k^2/m$, are small, the final pp system is in the $^1S_0$ state. The reaction therefore acts as a spin-isospin filter going from the $(^3S_1,^3D_1)$ of the deuteron to the final $^1S_0$ of the diproton. Furthermore, if the momentum transfer $\vec{q} = \vec{k_f} - \vec{k_i}$ between the initial proton and final neutron is also small, other final states are weakly excited. Under such conditions the spin independent amplitude α of Eq. (3.1) contributes very weakly in the differential cross section of the $dp \to \{pp\}_s n$ reaction.

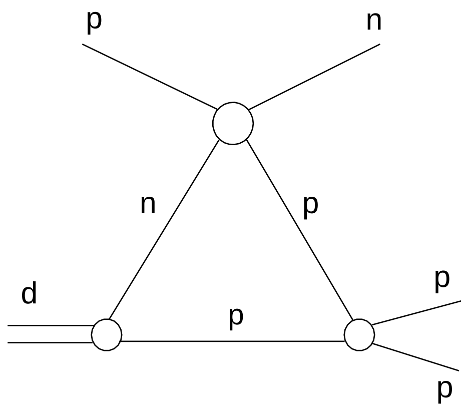

Figure 3.1: Impulse approximation diagram for the deuteron charge-exchange on hydrogen.

The matrix element of the $dp \to \{pp\}_s n$ transition is of the form [38]

$$F(\vec{k_f}, \vec{k_i}; S, \nu_f, M, m_p, m_n) = \langle \psi^{(-)}_{pp,\vec{k}}; S, \nu_f, m_n | f_{np}(\vec{k_f}, \vec{k_i}) \exp(\tfrac{1}{2} i\vec{q} \cdot \vec{r}) | \Phi^M_d; m_p \rangle, \quad (3.7)$$

where $\psi^{(-)}_{pp,\vec{k}}(\vec{r})$ describes the outgoing pp wave function with relative momentum $2k$, total spin S (0 or 1) and projection ν_f. $\Phi^M(\vec{r})$ is the deuteron initial wave function of spin projection M. The m_p and m_n represent magnetic quantum numbers of the initial proton and final neutron respectively. These wave functions have argument $\vec{r} = \vec{r}_1 - \vec{r}_2$, where particles 1 and 2 are the initial neutron and proton in the deuteron and 3 the target proton. In order to simplify Eq. (3.7) authors have decomposed the deuteron wave function into S and D-states. Therefore, the final form factor describing the transition from a deuteron to a ${}^1S_0$-state of the final pp pair contains two terms

$$\begin{aligned} S^+(k, \tfrac{1}{2}q) &= F_S(k, \tfrac{1}{2}q) + \sqrt{2} F_D(k, \tfrac{1}{2}q)\,, \\ S^-(k, \tfrac{1}{2}q) &= F_S(k, \tfrac{1}{2}q) - F_D(k, \tfrac{1}{2}q)/\sqrt{2}\,. \end{aligned} \quad (3.8)$$

The S^+ and S^- are longitudinal ($\lambda = 0$) and transverse ($\lambda = \pm 1$) form factors, where λ is the spin-projection of the deuteron. The matrix elements F_S and F_D are related to the S and D-state components of the deuteron wave functions $\Phi_S(\vec{r})$ and $\Phi_D(\vec{r})$ and the pp wave function $\psi^{(-)}_k$ in the following way

$$\begin{aligned} F_S(k, \tfrac{1}{2}q) &= \langle \psi^{(-)}_k | j_0(\tfrac{1}{2}qr) | \Phi_S(\vec{r}) \rangle\,, \\ F_D(k, \tfrac{1}{2}q) &= \langle \psi^{(-)}_k | j_2(\tfrac{1}{2}qr) | \Phi_D(\vec{r}) \rangle\,. \end{aligned} \quad (3.9)$$

If the amplitudes are normalised such that the $np \to pn$ differential cross section has the form

$$\left(\frac{\mathrm{d}\sigma}{\mathrm{d}t}\right)_{np\to pn} = |\alpha(q)|^2 + |\beta(q)|^2 + 2|\gamma(q)|^2 + |\delta(q)|^2 + |\varepsilon(q)|^2\,, \quad (3.10)$$

then the observables involving only the initial spins that are accessible at ANKE are linked to the amplitudes through [38, 39]:

$$\begin{aligned}
\frac{d^4\sigma}{dtd^3k} &= \tfrac{1}{3}I\left\{S^-(k,\tfrac{1}{2}q)\right\}^2\,, \\
I\,A_y^d &= 0\,, \\
I\,A_y^p &= -2Im(\beta^*\gamma)\,, \\
I\,A_{xx} &= |\beta|^2+|\gamma|^2+|\varepsilon|^2-2|\delta|^2R^2\,, \\
I\,A_{yy} &= |\delta|^2R^2+|\varepsilon|^2-2|\beta|^2-2|\gamma|^2\,, \\
I\,C_{y,y} &= -2Re(\varepsilon^*\delta)R\,, \\
I\,C_{x,x} &= -2Re(\varepsilon^*\beta)\,, \\
C_{yy,y} &= -2A_y^p\,,
\end{aligned} \tag{3.11}$$

where the spin-flip intensity

$$I = |\beta|^2+|\gamma|^2+|\varepsilon|^2+|\delta|^2R^2\,. \tag{3.12}$$

The function

$$R = S^+(k,\tfrac{1}{2}q)\big/\,S^-(k,\tfrac{1}{2}q) \tag{3.13}$$

is the ratio of two transition form factors that involve the S- and D-states of the deuteron wave function. In the forward direction $R = 1$.

Although the formulae given here describe the general features of our data, detailed comparisons with theory are made using a program that takes higher final pp waves into account. These can, in particular, dilute the polarisation signals [38].

3.2 "Proof-of-principle" experiment at ANKE

The $\gamma(q)$ amplitude vanishes in the forward direction. The contributions of $|\gamma(q)|^2$ to the cross section and the Cartesian tensor analysing powers A_{xx} and A_{yy} in Eq. (3.11) are negligible under the conditions of the ANKE experiment. Measurements of the unpolarised cross section and the two transverse analysing powers can therefore determine separately the values of $|\beta(q)|^2$, $|\varepsilon(q)|^2$, and $|\delta(q)|^2$ at fixed momentum transfer q. The two deuteron-proton spin correlations that are measurable at ANKE,

$C_{x,x}$ and $C_{y,y}$, fix two of the relative phases. The proton analysing power A_y^p gives mainly information on the spin-orbit amplitude $\gamma(q)$.

The ANKE collaboration has embarked on a systematic programme to measure the differential cross section, analysing powers, and spin–correlation coefficients of the $\vec{d}p \to \{pp\}_s n$ deuteron charge–exchange breakup reaction. The aim is to deduce the energy dependence of the spin–dependent np elastic amplitudes.

The first experiment in the deuteron charge–exchange programme at ANKE, which then was followed by subsequent experiments discussed in this thesis, was carried out at a deuteron beam energy of $T_d = 1170$ MeV (585 MeV per nucleon). The main goal of this run was to check the methodology to be used in np charge–exchange studies. The results shown in Fig. 3.2 [40] are compared with the predictions of the impulse approximation program [38] using as input the neutron–proton amplitudes taken from the SAID analysis [41].

The precision of these data is such that one can derive ratios of the magnitudes of amplitudes that are comparable in statistical accuracy with those that are in the current database [41]. Thus, at $T_n = 585$ MeV per nucleon, we find

$$\begin{aligned} |\beta(0)|/|\varepsilon(0)|^{\mathrm{ANKE}} &= 1.86 \pm 0.15\,, \\ |\beta(0)|/|\varepsilon(0)|^{\mathrm{SAID}} &= 1.79 \pm 0.27\,. \end{aligned}$$

Note, that the uncertainty of 0.27 in SAID prediction was deduced from looking at the experimental data in the neighbourhood. It seems therefore that, in cases where the amplitudes are well known, one can get reliable results.

In order to extract full information about the neutron–proton amplitudes, and not merely their ratios, one has to measure absolute cross sections as well as analysing powers. The obtained charge–exchange cross section and the tensor analysing powers are shown in Fig. 3.2. The agreement with the calculation of the unpolarised cross section in impulse approximation [38] is very encouraging.

The success of the method and results achieved suggest one should continue the study of the observables of the $dp \to \{pp\}_s n$ reaction at higher energies, where much less is known about the np scattering amplitudes, and therefore, such studies might provide valuable information in this direction.

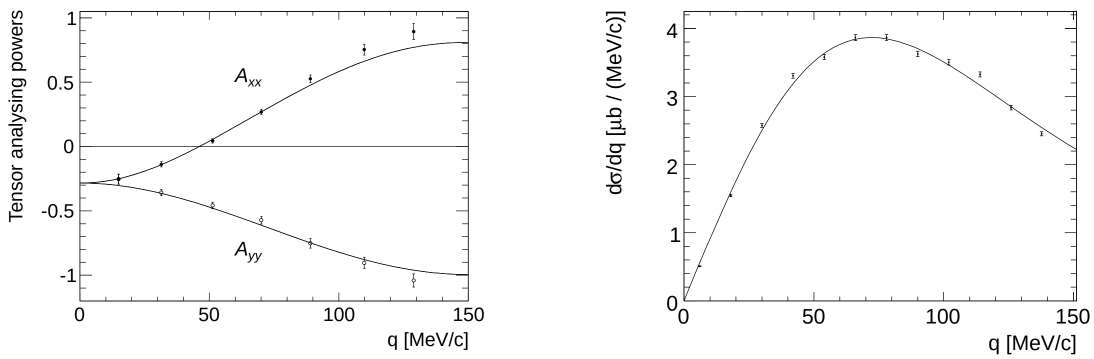

Figure 3.2: Tensor analysing powers (left) and unpolarised differential cross section (right) of the $dp \rightarrow \{pp\}_s n$ reaction for excitation energies $E_{pp} < 3$ MeV [31, 40] compared with impulse approximation predictions [38].

Chapter 4

ANKE/COSY facility

The experiments reported in this thesis were carried out using the ANKE magnetic spectrometer [42] that is placed at an internal position of the COoler SYnchrotron (COSY) [43] of the Forschungszentrum Jülich (Germany). The following sections describe the ANKE setup and the COSY accelerator. The polarised ion beam source at COSY and the polarised internal target at ANKE are also described in detail.

4.1 COoler SYnchrotron

The COSY accelerator and storage ring, shown schematically in Fig. 4.1, delivers deuteron and proton beams up to the momentum of 3.7 GeV/c. The available energy ranges for deuterons and protons are from 23 MeV to 2.27 GeV and from 45 MeV to 2.83 GeV, respectively.

Initially the H^- and D^- ion beams are developed in the ion source. COSY has two sources; one for polarised and another for unpolarised beams. The ions are pre-accelerated in the cyclotron JULIC up to 295 MeV/c and then injected into the storage ring via a charge-exchanging stripper carbon foil.

The circumference of COSY is 184 m. Two straight sections with lengths of 40 m each are used to implement internal experiments (ANKE, WASA, COSY-11, EDDA). In addition, they also contain accelerator-specific components such as the accelerating RF-cavity, the electron cooler, scrapers, the stochastic pick-up and kicker tanks, Schottky pick-ups and beam current monitors. In addition, COSY has also three extraction beam lines serving external experimental areas (TOF, BIG

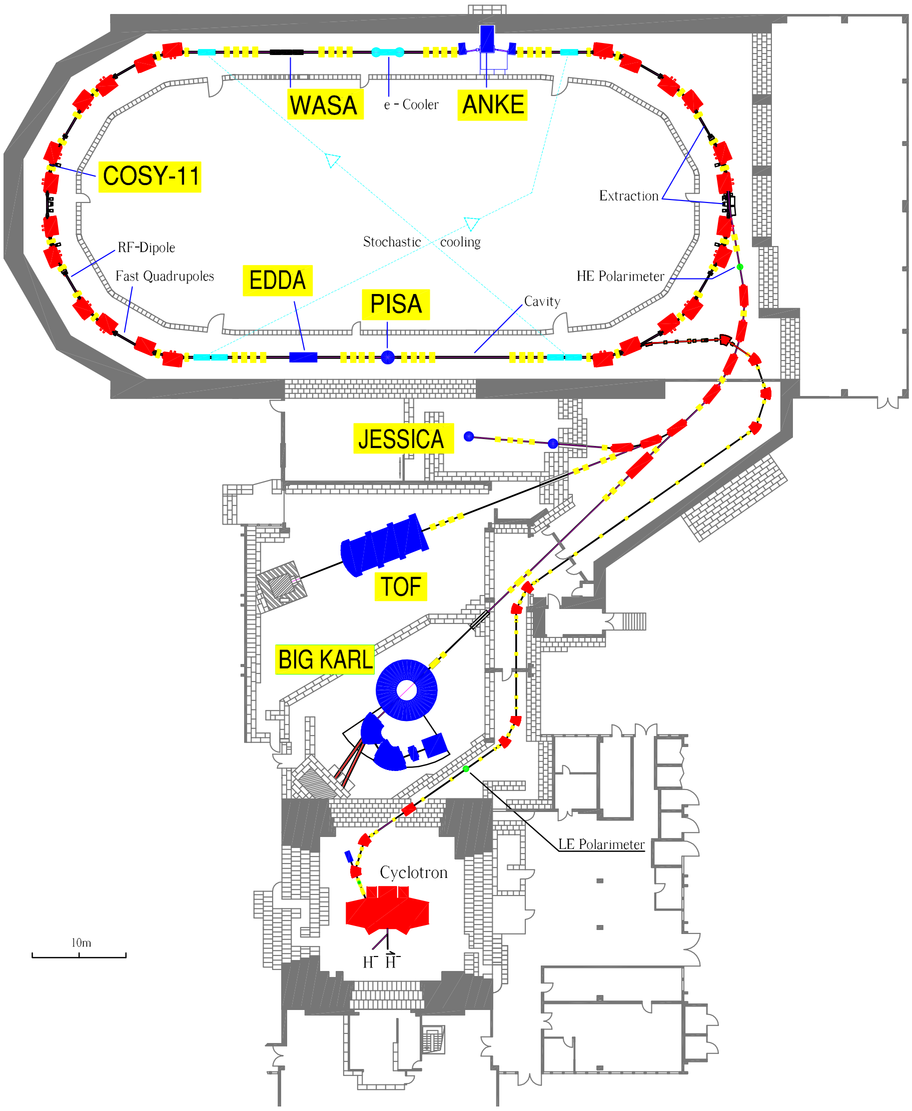

Figure 4.1: The COoler SYnchrotron COSY at the Forschungszentrum Jülich.

KARL).

Two different cooling techniques are implemented at COSY to shrink the beam phase space. Electron cooling [44, 45] is successfully used up to a momentum of 600 MeV/c and is complemented by a stochastic cooling system [46] that covers the upper momentum range from 1.5 GeV/c to 3.3 GeV/c. These cooling techniques significantly reduce the momentum spread of the COSY beam, such that a momentum resolution down to $\Delta p/p = 10^{-3} - 10^{-5}$ has been achieved. Numerous experiments at COSY show that the number of stored protons/deuterons in the COSY ring can be as high as 6×10^{10} (space charge limit is $\approx 2 \times 10^{11}$ particles). Taking the beam revolution frequency into account, which is of order 1 MHz, COSY is able to provide up to 10^{17} particles per second on the target.

4.1.1 Polarised ion source at COSY

The polarised ion source at COSY [47, 48] produces negatively charged H^- and D^- ions that are then injected into the cyclotron. The scheme of the source is shown in Fig. 4.2.

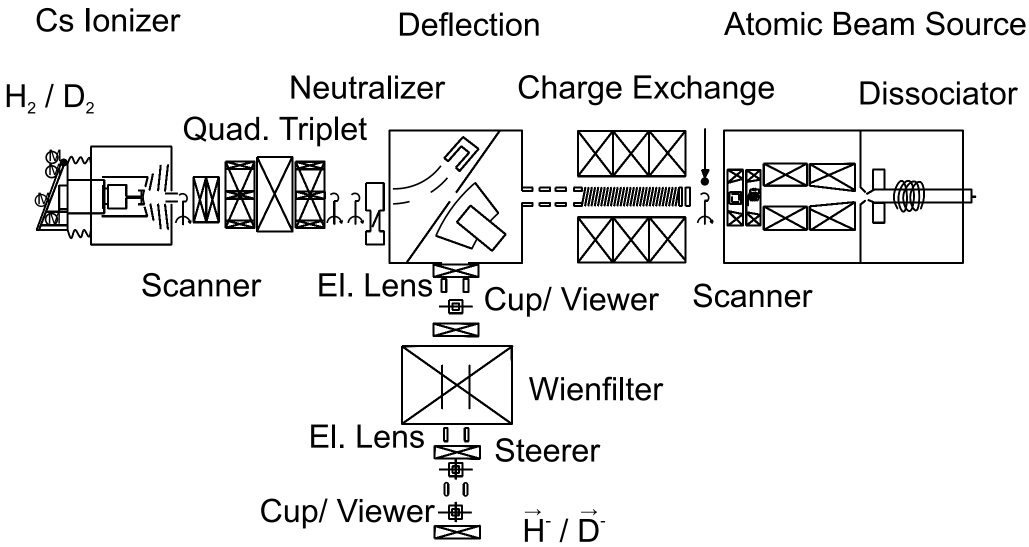

Figure 4.2: The polarised ion source at COSY.

The source consists of several groups of components: the pulsed atomic beam source, the cesium beam source, and the charge-exchange and extraction region. At first, the neutral and unpolarised hydrogen and deuterium gas molecules are dissociated in a RF discharge and, in order to maintain a high order of dissociation, small amounts of nitrogen and oxygen is added. This reduces surface and volume recombination. Passing though the sextupole magnet system the residual molecules are separated from the atomic beam. The first sextupole defocuses atoms with the electron spin state $m_j = -1/2$ and only atoms with $m_j = +1/2$ are retained in the beam [49]. A second sextupole magnet acts as an achromatic lens focusing the atomic beam into the ionizer region. The nuclear polarisation is provided by two radio frequency transitions changing the relative populations between the hyperfine substates of the hydrogen atoms. A different combinations of the vector and tensor polarisations for the D^- beams is achieved by employing more rf transitions and sextupoles that allow the exchange of occupation numbers of the different hyperfine states in the deuteron [47].

Passing through the charge-exchange region, the beam then collides with the neutral Cs atoms. Since the electro-negativity of the Hydrogen is significantly higher than that for the Cesium, hydrogen atoms asquire an additional electron and become negatively charged in the process $\vec{\mathrm{H}}^0 + \mathrm{Cs}^0 \rightarrow \vec{\mathrm{H}}^- + \mathrm{Cs}^+$.

The acceptance of the first sextupole magnet of the atomic beam source increases in inverse proportion to the beam temperature. Furthermore, the dwell time in the charge-exchange region, which directly affects the charge-exchange process efficiency, is inversely proportional to the beam velocity. Hence, in order to benefit from this, the atomic beam is cooled to about 30 K, while passing an aluminium nozzle of 20 mm length and 3 mm diameter. Though passing through the sextupole magnet system, scattering in the vicinity of the nozzle takes place that therefore partially reduced these beneficial effects.

The fast Cs^0 beam is produced in two-step process. First, the cesium vapour is thermally ionized on a hot (1200°C) tungsten surface at an appropriate beam potential of $40 - 60$ kV, where the ionization probability is the highest, and the beam is then focused by a quadrupole triplet to the neutraliser. The neutraliser is filled with cesium vapour only during the injection period of COSY. The fast Cs^+ beam becomes neutralized and enters the charge-exchange region, where it collides with the polarised hydrogen ion beam from the atomic beam source. The remaining Cs^+ beam is deflected in front of the solenoid to the Faraday cup. A typical efficiency of the neutraliser is about 90%.

In the final stage, the produced H^- and D^- beams are deflected by a 90° electrostatic, toroidal deflector into the injection beam line of the cyclotron. In this final phase a Wien filter separates the negatively charged ions from electrons and other background. It is rotatable around the beam axis so that every orientation of the polarisation axis can be provided. In practice, the spin axis is oriented in parallel to the cyclotron magnetic field. Therefore, no polarisation is lost during the acceleration.

4.1.2 Polarised deuteron and proton beams at COSY

The polarised H^- or D^- ion beam delivered by the source is pre-accelerated in the cyclotron JULIC and injected by charge exchange into the COSY ring, where it is further accelerated to the final energy. A cavity with E–field is used for the acceleration, which is passed by the COSY beam by a million times per second. The main problem during the acceleration is to maintain the beam polarisation. This is much more complicated for proton beams rather then for deuterons. Details on the acceleration process and techniques employed for vertically polarised protons and deuterons at COSY can be found in Refs. [50, 51].

4.2 ANKE spectrometer

The Apparatus for Studies of Nucleon and Kaon Ejectiles (ANKE) [42] is an internal experiment in one of the straight sections of COSY (see Fig. 4.1). It was designed and built between 1994 and 1997 and was first used in an experiment in 1998.

4.2.1 Overview

The ANKE spectrometer, shown in Fig. 4.3, consists of a magnetic system and different types of detection systems, both for positively and negatively charged particles.

The primary aim of the magnetic system of the ANKE spectrometer is to separate the ejectiles from the circulating COSY beam in order to identify them and analyse their momentum. It comprises three dipole magnets. D1 is responsible for deflecting the beam by an angle α from its straight path onto a target. A large spectrometer dipole magnet D2 is used to analyse the momentum of the reaction products that originate from beam-target interactions, including 0° in the forward direction. Its maximum field strength is 1.57 T. The beam is deflected by an angle -2α in the D2 field. This is then compensated by D3, which returns the beam back to the nominal orbit.

For a given COSY beam momentum the α angle is directly related to the D2 field strength. Depending on the requirements, a variety of experimental conditions can

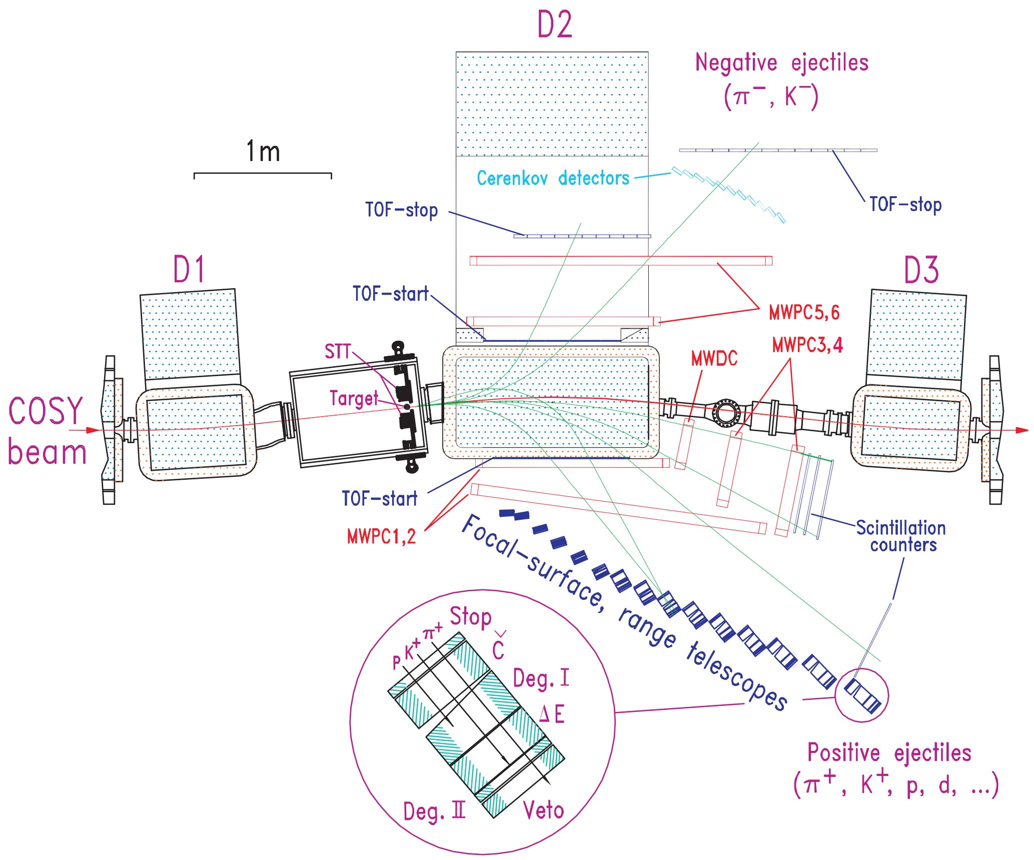

Figure 4.3: Layout of the ANKE detection system showing the alignment of the D1-D3 magnets and different types of detectors.

by realised by using different combinations of α and the D2 field strength. But for each of the settings the magnet D2 needs to be displaced horizontally perpendicular to the nominal beam direction. For this purpose, D2 is installed on rails.

The ANKE detection system consists of several main parts:

- The forward detector (FD), which is capable of measuring high momentum particles close to the COSY beam orbit.
- The positive detector (PD) for the detection of positive projectiles, covering much higher angles than the forward part.
- The negative detector (ND), which located on the opposite side to the positive detection system, partially inside the D2 magnet frame, is responsible for measuring negatively charged pions and kaons.

- The silicon strip counters, also called Spectator Tracking Telescopes (STTs), which are located close to the target position. They are used to measure low energy spectator protons.

All these detectors, except the STT, use multiwire proportional chambers (MWPC) for track reconstruction and plastic scintillator counters to obtain the time information. In the PD and ND the time of flight (TOF) is measured between start and stop counters. In order to maximally increase the flight path for TOF measurement, start detectors are placed immediately behind the exit window of D2.

The energy loss of the ejectiles can also be used for particle identification. In order to increase the difference in the energy losses of pions, kaons and protons, the scintillators of the PD stop counters include tapered copper degraders of variable thickness (see Fig. 4.3).

The momentum acceptance of the positive and negative detectors is in the range of $0.3 - 0.8$ GeV/c, while the forward part allows one to detect positively charged particles in momentum range $0.8 - 3.7$ GeV/c.

4.2.2 The forward detector

The forward part of ANKE detector is located in the gap of 1.6 m between the D2 and D3 dipole magnets. The closeness of the FD part to the COSY beam pipe introduces the requirement for the system to operate at rather high counting rates of 10^5 s^{-1} and more. Furthermore, high spatial resolution of less than 1 mm is required from the MWPCs, in order to achieve momentum resolution of about 1%, which is essential for distinguishing proton-proton pairs with low excitation energy.

The FD consists of multiwire proportional and drift chambers for track reconstruction, two layers of scintillation hodoscope and Cherenkov counters, which are placed behind the hodoscope. The MWPCs have two wire planes each, with horizontally (X) and vertically (Y) aligned wires at a distance of 1 mm as well as two strip planes, which are inclined by $\pm 18°$ with respect to the wires. The MWPCs are mounted on a common support frame with the forward hodoscope.

The forward hodoscope is composed of two planes of vertically aligned scintillators from polystyrene. The first and second planes contain 8 and 9 scintillators, respectively. In each plane, counters which are placed close to the COSY beam pipe, have smaller thickness (15 mm) and width (varying between 40 and 60 mm) compared to those responsible for lower momentum region (20 mm thick, 80 mm wide). The height of all scintillators is 360 mm. Each of the scintillators is read out by two photomultiplier tubes placed on both ends. They provide timing as well as the amplitude signal. The timing signal can be used to form a trigger and also to measure the differences of the arrival times of particle pairs. A typical time resolution for events with two registered particles is around 0.5 ns. The amplitude signal from photomultipliers provides information about the energy loss in the scintillator, which can be measured with 10% accuracy.

The 16 Cherenkov counters, used in some specific experiments, can be placed behind the forward hodoscope. They have been developed and constructed at the *High Energy Physics Institute, Tbilisi State University* (HEPI) and tested at the *Joint Institute of Nuclear Research* (JINR), Dubna. They are 80 mm wide, 50 mm thick and 300 mm long and are made of lucite. The inclination angle of the Cherenkov detectors with respect to the vertical axis can be adjusted in such a way as to discriminate deuterons against protons of the same momentum [52].

The angular acceptance of the FD is about 12° in the horizontal plane and about 3.5° in the vertical.

4.3 Target types

Two different target types are used at ANKE. The cluster target provides only unpolarised hydrogen and deuterium jets with high target density, while the Atomic Beam Source (ABS), in conjunction with the storage sell, can provide polarised/unpolarised H and D targets with moderate density. The main purpose of the experiment determines which target type has to be employed.

4.3.1 Unpolarised cluster target

Cluster beams are of high interest for accelerator experiments. They can be used as windowless targets of very high purity. If produced in Laval nozzles, their density can easily be varied by over orders of magnitude by changing the nozzle temperature or the gas input pressure. Unlike gas-jet beams, the cluster beams have a homogeneous density distribution.

The cluster-target device at ANKE consists of three main parts: the cluster source, the analysing chamber and the beam dump [53]. Clusters with a typical size of 10^3-10^4 atoms are produced in the Laval nozzle, which is cooled down to ≈ 20 K. The produced cluster beam, surrounded by a gas beam, hits a conical aperture with an opening of 700 μm, acting as a skimmer. As consequence, only a well-formed cluster beam passes this vacuum stage and nearly the whole of the gas remains in the skimmer and is pumped by a roots pump. There is also an additional conical aperture with diameter 900 μm, which defines the cluster beam diameter and holds the residual gas back. After this stage, the cluster beam with a constant angular divergence enters the analysing chamber.

The analysing chamber is equipped with a scanning rod with a thickness of 1.0 mm, which is controlled by a stepper-motor and can be positioned in units of 1/24 mm. When the rod is placed inside the cluster beam, a part of the beam is stopped and converted into a gas load which can be recorded by an ionization vacuum meter. Information on the cluster beam size and position can be obtained in such a way. Furthermore, if the rod is placed at a fixed position inside the cluster beam, this system allows the density of the beam to be monitored.

Passing the analyser chamber, the cluster beam enters the beam dump, where the clusters are destroyed. The large fraction of the formed gas is directly pumped by the turbo pump. In order to further reduce the remained gas pressure in the analyser chamber, the beam dump consists of differentially pumped vacuum chambers which are separated by small apertures.

As was already mentioned, the cluster beam density can be varied over a wide range. The density increases when the temperature of the nozzle decreases and the pressure increases. It reaches its maximum when the gas is already in a supersaturated state before passing the nozzle. Under such conditions, hydrogen cluster beam densities of up to $2 - 5 \times 10^{14}$ atoms/cm^2 have been achieved. The density is equally distributed within the cluster beam, which can be well approximated by a homogeneous cylinder with typical width of around 9 mm.

4.3.2 The Polarised Internal Target (PIT)

A windowless cluster target at ANKE, which was described in the previous section, produces stable cluster beams with high density and small divergence, providing highly localised beam-target overlap in transverse and longitudinal beam directions. This therefore creates a perfect condition for the track reconstruction process in the subsequent analyses. The main disadvantage of this type is that it is limited to unpolarised targets only. In order to carry out double-polarised experiments a polarised internal target (PIT) [54] was developed and implemented at ANKE in 2005. The Atomic Beam Source (ABS) of the PIT provides polarised hydrogen and deuterium jet beams with different vector and tensor polarisations. It has the ability to change the polarisation state in a short time, which is very important feature, allowing one to significantly simplify the asymmetry evaluation between two polarised states in the analyses, as we will see in later sections. But unlike the cluster target, the ABS provides much lower target densities (around three orders of magnitude). This is partially compensated by employing a long storage cell, which is fed from the ABS.

The ABS is mounted between the D1 and D2 dipole magnets of the ANKE spectrometer (see Fig. 4.3). Due to the limited space it is mounted vertically. The ABS is shown schematically on Fig 4.4. It consists of a dissociator, where hydrogen and deuterium molecules dissociate to H and D atoms, and sets of sextupole magnets and radio-frequency (rf) transitions, where the atomic beam is polarised. This setup is aligned in five different chambers. Each of them has separate system of pumps, consisted of membrane pumps, turbo-molecular pumps and cryopumps, to remove all unnecessary gas from the chamber. The vacuum pressure is different in each chamber, reaching 5×10^{-8} mbar in the final stage, at the exit of the polarised gas.

The dissociator employs an rf discharge to dissociate molecular hydrogen or deuterium. It forms a resonant LC-circuit, which is fed by a 13.560 MHz generator delivering up to 600 W into a 50 Ω resistance. Dissociation degrees of about 0.8 are typically achieved.

Atomic hydrogen and deuterium exits from the dissociator via a nozzle, which is cooled down to 60 K. It is made from 95.5% Al and has a simple conical shape with the tip cut. After exiting the dissociator, the supersonic atomic beam passes a stainless steel beam skimmer, a Cu diaphragm, and enters the magnetic system of the ABS.

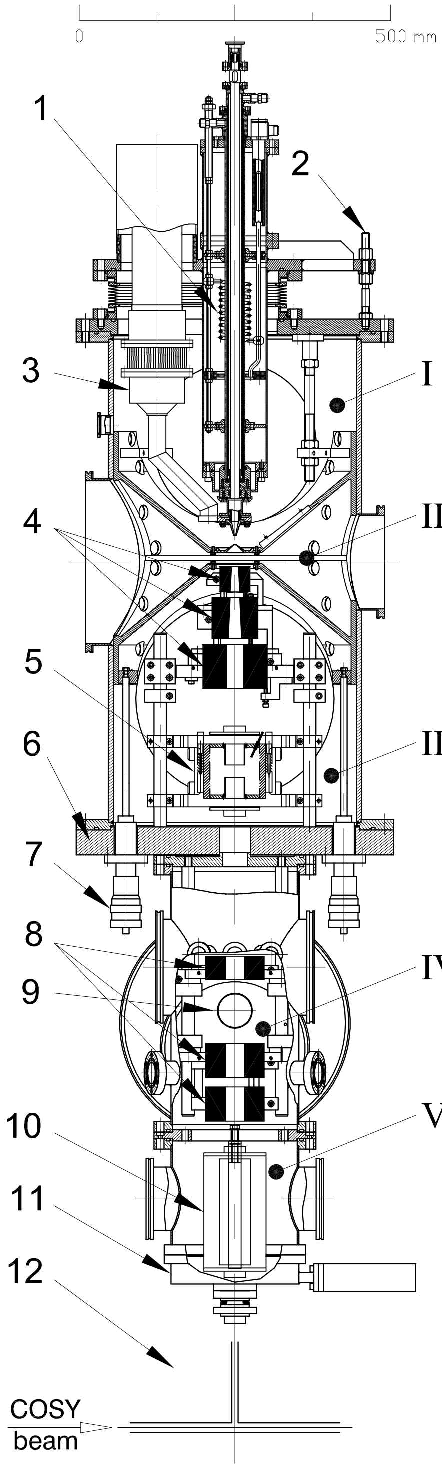

Figure 4.4: The schematic drawing of the Atomic Beam Source:

1. Dissociator
2. Adjustment screw
3. Cu heat-bridge for nozzle cooling
4. First set of sextupole magnets
5. Medium field rf transition (MFT)
6. Support plate
7. Rotational feed-through
8. Second set of sextupole magnets
9. Beam chopper
10. Weak (WFT) and strong (SFT) field rf transitions
11. Vacuum gate valve separating ABS and ANKE target chambers
12. Storage cell

The magnetic system uses six sextupole magnets consisting of permanently magnetised segments, delivering pole-tip fields around 1.5 T. The sextupole magnet field acts on atoms with a radial force $\vec{F}_r = -\mu_{\text{eff}} \cdot \bigtriangledown \vec{B}$, where μ_{eff} is the effective magnetic moment. The $\mu_{\text{eff}} > 0$ for atoms in the hyperfine states with the electron spin parallel to $\vec{B}$ and $\mu_{\text{eff}} < 0$ if antiparallel. Hence, in the first case atoms are deflected towards the beam axis and the sextupole acts as a focusing magnet, focusing the atomic beam into a feeding tube of the storage cell. In the second case the magnet has a defocusing effect and atoms are deflected away from the beam axis. In such case the magnet acts as a filter, removing unnecessary hyperfine states.

The rf transition units are used to change the relative occupation numbers of the states. The ABS is equipped with three types of transition units, a weak field (WFT), a medium field (MFT), and a strong field (SFT) rf transition units. Together with the sextupole magnets, they allow one to achieve all possible vector and tensor polarisations of the atomic hydrogen and deuterium gas. When the atomic gas passes a static magnetic field $\vec{B}_{\text{stat}}$, hyperfine states split according to the Breit-Rabi diagram [49]. Change in population numbers of the hyperfine states are induced by a rf field $\vec{B}_{\text{rf}}$. In all transition units the $\vec{B}_{\text{stat}}$ field is produced by parallel homogeneous and gradient magnetic fields, both orthogonal to the atomic beam direction. It is of order $B_{\text{stat}} \leqslant 10$ G for deuterium and $B_{\text{stat}} \leqslant 5$ G for hydrogen in WFT and is slightly higher for MFT and SFT. Unlike WFT and MFT units, where the $\vec{B}_{\text{rf}}$ is produced by rf solenoids with axis along the atomic beam direction, the SFT unit operates at much higher frequencies and works as a rf cavity. It produces the $\vec{B}_{\text{rf}}$ in the Cu box, tuned at $\lambda/4$ resonance.

At weak magnetic fields, the total atomic spin F is a good quantum number. In hydrogen $F = 1$, which forms three states $|1\rangle$, $|2\rangle$ and $|3\rangle$, corresponding to magnetic quantum numbers $m_f = +1$, 0 and -1, respectively, which are equally spaced in energy. In deuterium the total atomic spin $F = 3/2$ forms four states $|1\rangle$, $|2\rangle$, $|3\rangle$ and $|4\rangle$ ($m_f = +3/2$, $+1/2$, $-1/2$, $-3/2$). The WFT transition unit induces transitions between hyperfine states with $\Delta m_f = \pm 1$. $|\Delta m_f| = 2$ transitions are forbidden. The MFT unit operates at higher values of $\vec{B}_{\text{stat}}$, where the difference in energy spacings of neighbouring hyperfine states allows one to select single transitions. Furthermore, consecutive transitions are also possible, by adjusting the gradient field. The SFT unit is used to induce transitions between states in the upper and lower hyperfine multiplets.

The ABS achieves maximum atomic beam intensities of $(7.5 \pm 0.2) \times 10^{16}$ particle/s for hydrogen (states $|1\rangle$ and $|2\rangle$) and $(3.9 \pm 0.2) \times 10^{16}$ particle/s for deuterium (states $|1\rangle$, $|2\rangle$ and $|3\rangle$). The vector and tensor polarisation of the atomic beam can be monitored by a Lamb-shift polarimeter [55]. The following maximum numbers have been observed in the deuteron case: vector polarisation of $88 - 96\%$ and tensor polarisation of $85 - 90\%$ of the maximum theoretically allowed values. But unfortunately, as we will see in chapter 8, these numbers are further diluted due to the inevitable polarisation losses when the atomic beam exits the ABS and enters into a storage cell.

The polarised atomic hydrogen and deuterium jets have an azimuthal symmetry around the beam direction. Its profiles are well approximated by Gaussian, with $\sigma_\perp \approx 3$ mm, which leads to much lower areal target density (around three orders of magnitude), compared to the cluster target. In order to increase the density of the polarised target, a storage cell [56] is used. It consists of a feeding and beam tubes, as shown in Fig. 4.5. The beam tube may have a circular or rectangular cross section. The gas density distribution in a storage cell has a maximum at the feeding tube location and drops approximately linearly towards the edges of the cell [57]. Under such conditions the areal target density ρ (cm^{-2}) is a function of the length of the cell:

$$\rho = \frac{1}{2}(L_1 + L_2)n_0 \propto \frac{1}{d^3}\,, \tag{4.1}$$

where n_0 is a target density at feeding tube position (cm^{-3}) and L_1 and L_2 are cell lengths of the left and right parts of the cell, respectively. The central density n_0 is determined by the total conductance of the cell. When the beam tube of the cell is approximated to have a circular cross section, then the central density is proportional to d^{-3}, where d is its diameter. Therefore, in order to achieve highest areal target densities in the storage cell, it should be as long as possible and have reasonably small transverse dimensions. The length of the cell is limited by the dimensions of the ANKE target chamber where it is placed, and cannot exceed 400 mm. Minimum transverse dimensions are limited by the size of the COSY beam, which should pass the cell without touching its walls. Otherwise, due to the much higher material density compared to the gas target, the cell can produce very high background in the experiment, which is not acceptable. Due to this, a special experiment was carried out to study the beam size at different energies and determine the optimal cell dimensions [57]. As was found out, the particle density distribution in the COSY beam can be well approximated by a two-dimensional Gaussian, with σ varying from

1.2 mm to 7.6 mm, depending on the transverse direction and energy. In addition, the COSY orbit deviates from the nominal during the acceleration, leading to some losses in the beam intensity if the cell walls are touched. Taking all these into account, optimal dimensions of $20 \times 15 \times 370$ mm^3 (Width$\times$Height$\times$Length) were found for the storage cell. In a subsequent commissioning experiment such a cell achieved maximum target density of about 10^{13} cm^{-2} [58]. For comparison, the areal density of the ABS jet itself is around 1.5×10^{11} cm^{-2} [59].

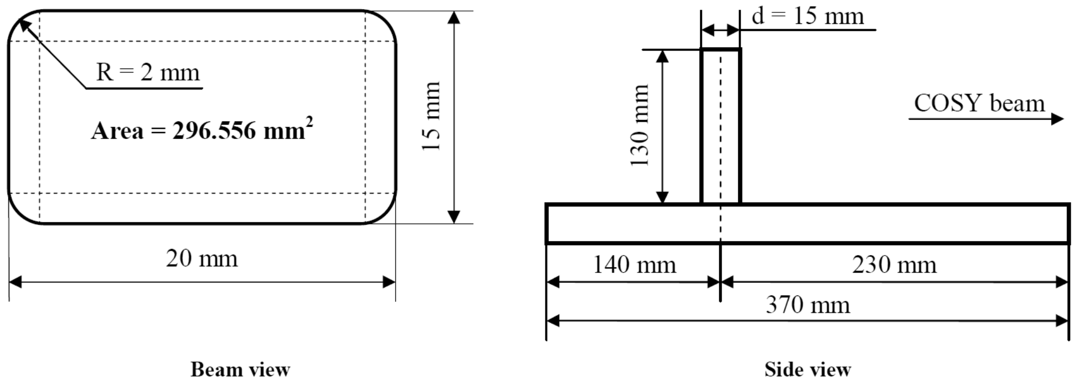

Figure 4.5: Schematic drawing of a storage cell.

Openable cells, which are currently being developed at COSY, can be opened during beam injection and acceleration and closed during the data taking. Thus, the beam losses at injection and from the motion of the beam orbit during acceleration can be avoided altogether. Therefore, it can have transverse dimensions less than that for the fixed cell, yielding an significant increase in the density.

Chapter 5

Experiments

The experiments reported here were carried out over three different time periods using the ANKE-COSY experimental facility of the Forschungszentrum Jülich. Initially a polarised deuteron beam was used in conjunction with an unpolarised hydrogen cluster target [53]. In 2005 the $\vec{d}p \to \{pp\}_s n$ reaction was studied at deuteron beam energies $T_d = 1.2$, 1.6 and 1.8 GeV. The following year, the beam energy was increased to 2.27 GeV, with 1.2 GeV being repeated for polarimetry purposes. However, for the study of the spin-correlation parameters in 2009 [60], a double-polarised experiment was carried out at 1.2 and 2.27 GeV, involving the newly developed polarised internal target [56, 54].

5.1 Single-polarised experiments

In 2005 two sequential COSY cycles were organised for 1.6 GeV (first) and 1.8 GeV (second) energies, by combining them with the 1.2 GeV flat top. Such measures allowed us to use the polarisation export technique described in Section 5.3. The injected beam was first accelerated to 1.2 GeV, where a part of the experimental data was taken and then, without an additional injection, to one of the higher energies. In 2006 only one super-cycle was used, which combined 1.2 GeV and 2.27 GeV flat tops in a similar way. The polarised deuterium ion source at COSY was set up to provide a variety of states with different tensor and vector polarisations but, as listed in Table 5.1, the selections differed for the experiments with cluster or polarised cell target.

Experiment	State	I_0	P_z	P_{zz}
unpolarised target	1	1	0	0
	2	1	$+\frac{1}{3}$	+1
	3	1	$-\frac{2}{3}$	0
	4	1	$+\frac{1}{3}$	−1
	5	1	$-\frac{1}{3}$	+1
	6	$\frac{2}{3}$	0	+1
	7	$\frac{2}{3}$	0	−2
	8	$\frac{2}{3}$	−1	+1
	9	$\frac{2}{3}$	+1	+1
polarised target	1	1	0	0
	3	1	$-\frac{2}{3}$	0
	8	$\frac{2}{3}$	−1	+1

Table 5.1: The different configurations of the polarised deuteron ion source used in experiments, showing the nominal (ideal) values of the vector (P_z) and tensor (P_{zz}) polarisations and relative beam intensities (I_0).

5.2 Double-polarised experiment

In 2009 a double-polarised experiment was carried out. Three different combinations of vector and tensor polarised deuterons, with states listed in Table 5.1, were injected in consecutive cycles into the COSY ring to interact with a polarised hydrogen cell target, which was fed by a polarised Atomic Beam Source (ABS). A cell with dimensions $20 \times 15 \times 370$ mm^3 was used in order to increase target density up to 10^{13} cm^{-2}.

A dedicated beam development was required to ensure that the COSY beam passed successfully through the cell. Electron cooling and stacking injection [61] were employed, with hundreds of injections per cycle to increase the number of stored deuterons in the beam. In order to avoid excessive background coming from the interactions of the beam halo particles with the cell wall, scrapers were installed upstream of the target region.

The ABS was configured to produce two polarised states with equal gas densities.

The polarisation of the hydrogen target was flipped between hyperfine state $|1\rangle$ (spin-up $\uparrow$) and hyperfine state $|3\rangle$ (spin-down $\downarrow$) every five seconds throughout the whole COSY cycle, which lasted for one hour. Such a procedure simplifies the later analyses by obviating the need to consider the luminosities while calculating the asymmetries between these states. In order to have a possibility to measure the target spin-up $\uparrow$ and spin-down $\downarrow$ polarisations separately, runs with an unpolarised hydrogen cell-target were also undertaken.

The storage cell introduced additional complications in the analysis. The scattering of the beam halo particles on the cell walls produces extra background that dilutes the analysing power signal. Ideally one could record data with an empty cell and use them for background subtraction, but as mentioned earlier, the dedicated beam development enabled the bulk of the beam to pass through the cell without hitting the walls. For this reason, recording data with an empty cell would take much more time to collect sufficient statistics to determine the shape of the background. Additional runs were therefore recorded where nitrogen gas was injected into the cell to simulate the shape of the background (see details in Ref. [56]).

The determination of the scattering angles was also complicated due to the spread of the interaction points along the cell axis. The reconstruction of the longitudinal vertex coordinate Z is therefore required for each event. The vertex reconstruction procedure as well as the background subtraction in the double-polarised data are described in Section. 8.4.

5.3 Polarisation export technique

In all above mentioned experiments COSY cycles were configured to provide beam first at 1.2 GeV and then, without an additional injection, accelerate the deuterons to one of the higher energies. This procedure allows the use of the polarisation export method, which is crucial in the measurement of spin observables at higher energies. This technique involves undertaking the polarimetry measurements at the lowest $T_d = 1.2$ GeV flat top energy, where the analysing powers are precisely known, and assuming that the beam polarisation is unchanged at the higher energy. This procedure is viable because there are no depolarising resonances for deuterons in the COSY energy range.

In order to verify the polarisation export with a circulating deuteron beam at COSY, the scheme illustrated diagrammatically in Fig. 5.1 was implemented.

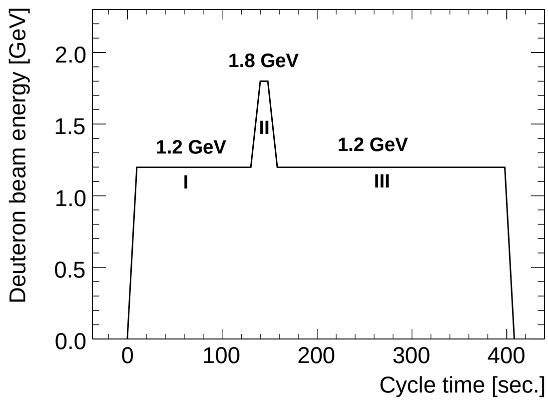

Figure 5.1: Schematic diagram illustrating the three different flat-top regions used in a single COSY cycle. The identity of the deuteron polarisation measured in regions I and III means that the 1.2 GeV polarisation could be exported to 1.8 GeV.

Using the *dp*–elastic reaction, which is sensitive to both vector and tensor polarisations of the beam, the asymmetries (β_y, β_{yy}) were measured in regions I and III of Fig. 5.1. The results are presented in Table 5.2. Given that, within the small error bars, $\beta^{I}_{y/yy} = \beta^{III}_{y/yy}$, no significant depolarisation can have taken place.

Flat top	β_y	β_{yy}
I	-0.213 ± 0.005	0.057 ± 0.003
III	-0.216 ± 0.006	0.059 ± 0.003

Table 5.2: Results of the asymmetry measurements for regions I and III of Fig. 5.1. β_y and β_{yy} represent the asymmetries for the vector and tensor components of the polarisation, respectively.

5.4 Data-taking

In the 2006 and 2009 experiments around $2 - 5 \times 10^9$ deuterons were stored in the COSY ring, while in 2005 it was significantly higher, up to 3×10^{10}. Such a high intensity caused an additional accidental background, slightly complicating the determination of the luminosity for the cross section measurement at $T_d = 1.6$ and 1.8 GeV. This background was successfully subtracted from the data and the details are described in Section. 7.2.

The beam intensity was monitored by the Beam Current Transformer (BCT) at COSY. When N particles with charge e are stored in the COSY ring and the beam circulating frequency is f, then the amplitude of the BCT signal is given by $U_{\mathrm{BCT}} = I_{\mathrm{beam}}R = NfeR$, where R is the total resistance of the COSY BCT ($R = 100\,\Omega$). The BCT signal is known to about 1%. It is a very simple and effective tool to monitor the beam intensity over time and, if the target density is assumed to be constant, then the BCT signal strength becomes directly related to the luminosity of the experiment.

The stored beam circulates in the COSY ring with frequencies of the order of 1 MHz, passing the target a million times per second. This led to intensities of about 4×10^{16} s^{-1} in the 2005 experiment. Assuming the unpolarised cluster target density of $2 - 3 \times 10^{14}$ atoms/cm^{-2}, this therefore resulted in the luminosity of $\approx 10^{31}$ cm^{-2} s^{-1}. The luminosity in 2006 was lower due to the beam intensity and even lower in 2009, where the polarised cell target was used. The experimental data were collected for a total of about 8 weeks of measurement over all three experiments.

Several triggers were set up and used in the experiments. The main trigger (Tr1), which was used in all three experiments, consisted of a coincidence between the different layers in the hodoscope of the FD. A special trigger (Tr2), based on energy loss in the forward hodoscope, was set during single-polarised experiments to easily identify heavy atoms, such as ^{3}He. In 2009 silicon detectors (STTs) were also involved in the experiment for commissioning purposes. A separate trigger (Tr3) has been used to handle the STT data. For each trigger signal (Tr1, Tr2, or Tr3) all subsystems of ANKE were read out by the Data Acquisition system (DAQ), converted into digital format and written in the data file for later analysis. The average readout time for one event is approximately 100 μs at ANKE, which leads to some dead time for the DAQ. For example, at a total trigger rate of 10 kHz, only approximately 50 % of the events are written in the data file. In order to correctly account for the DAQ efficiency in the later analyses, trigger rates were separately counted by scalers. A special trigger (Tr4) was used to read out scalers periodically every 100 ms. In such a way, the original trigger rate information was retained, which was then used to determine the DAQ efficiency.

The data taking lasted two and one week in 2005 and 2006, respectively, while, due to the much lower luminosity and complicated scenario, it lasted around five weeks in 2009. In such conditions it is very important to monitor the quality of the data obtained. In order to make a first check on the experimental data, some part of the events during experiments was redirected to the data stream and analysed. In such a way all the raw spectra from different detectors were being monitored during the experiments. Furthermore, a track reconstruction was also performed to obtain the momentum distribution of the scattered particles and, by identifying some of the reactions, missing-mass distributions were also built. All this information helped to ensure the stability of the experimental conditions and quality of the obtained data. In addition, the background conditions, which is a crucial point in the experiment involving a storage cell, could be easily identified in such a way. In order to monitor the polarisations of the beam and target a significantly higher counting rate was required. Therefore, it was preferred to measure the polarisations in offline analyses by using the set of runs obtained during a day-night cycle.

Chapter 6

Data analysis steps

Prior to any physics study, there are some mandatory steps in the data analysis that have to be managed first. This chapter describes the track reconstruction in the FD, by using hit information from multiwire proportional and drift chambers. In order to obtain a precise timing information of two fast proton tracks from the forward hodoscope, it is necessary to calibrate time delays between all 17 counters of the FD hodoscope. The final step is the geometry calibration of the ANKE setup, which fine tunes the precision of the momentum and angle reconstruction.

6.1 Track reconstruction

The information from multiwire proportional (MWPC) and drift (MWDC) chambers (see Fig. 4.3) are used for track reconstruction at ANKE. The existence of the strong magnetic field of the D2 spectrometer, ensures a good spatial separation of tracks with different mass-to-charge (m/q) ratio. Using the hit information from different layers of the MWPC and MWDC and the geometrical position of the target, tracks are found from the overall fit procedure. Details on the track-finding algorithm and the track-reconstruction software can be found in Refs. [62, 63].

6.2 Forward hodoscope calibration

The main objective of the experiments reviewed in this thesis, was to measure $dp \to \{pp\}_s n$ reaction. As we will see in the next section, at ANKE the fast two-proton events are separated from the contamination of deuteron-proton pairs on the basis of arrival time differences between the two tracks. A high time resolution (of the order of 1 ns) is required in this case. Such a precise time information can be provided only by the hodoscope of the forward detector. Since the time differences of the order of few nanoseconds are to be measured, delays that are introduced by the electronics and the setup become very important.

As was already mentioned in section 4.2, the forward hodoscope consists of 17 independent scintillator counters, each containing two photomultiplier tubes (PMTs). For hit detection the coincidence of the two signals is taken, but this is sensitive to the vertical coordinate of the particle hit. To correct for this effect, the electronic signals from each pair of PMTs (per scintillator) are processed with special electronics, including constant fraction discriminators and mean timers. By delaying the coincidence signal by a constant amount of time, the mean timer rejects its dependence on the vertical coordinate of the hit. However, this delay might significantly vary from one channel to another, leading to systematic relative delays between different counters. For instance, if a particle hits two counters simultaneously, two signals will be produced, one of which will be delayed in time compared to other.

The second source of such relative delays are the PMTs themselves, which always have some spread of the parameters. To gain match the PMTs of the same counter, as well as PMT pairs for the different counters, the high voltage (HV) is adjusted for each of them, separately. Since, the PMT response time generally depends on the HV, this also introduces the relative delays between different counters. In addition, the differences in lengths of the cables, which connect PMTs with electronics modules, are also sources of relative delays.

Measuring these delays and making appropriate correction on the hardware level is very hard task. In contrast, it can be easily performed in the analysis stage, as was done in our case. The relative delays between the neighbouring counters can be easily measured using the tracks hitting both of them simultaneously. The number of such events are severely limited, leading to insufficient measurement accuracy. Instead, by selecting the tracks that produced hits in both layers of the forward hodoscope, we measured time differences ($\Delta t_{k,l}$) between the hit counters in the first (k, $k = 1, ..., 8$) and second ($l = k$ or $l = k + 1$) layers. The time difference between each two neighbouring counters (Δt_k) was taken as a difference of the time differences between corresponding counters in different layers:

$$\Delta t_k^1 = \Delta t_{k,k} - \Delta t_{k+1,k} \tag{6.1}$$

for the first layer, and

$$\Delta t_k^2 = \Delta t_{k,k} - \Delta t_{k,k+1} \tag{6.2}$$

for the second. The obtained Δt_k^1 and Δt_k^2 values were then used for the hodoscope calibration.

6.3 Identification of different reactions

Figure 6.1 shows the experimental yield of ANKE for single charged particles at $T_d = 1.2$ GeV in terms of the laboratory production angle in the horizontal plane and the magnetic rigidity. The kinematic curves for some of the possible nuclear reactions are also illustrated.

Among the reactions observed, there are two that are of particular interest, namely the deuteron charge-exchange $dp \to \{pp\}_s n$ and the quasi-free $dp \to p_{\rm sp} d\pi^0$, where the proton, $p_{\rm sp}$, has about half the beam momentum. The latter reaction is used to measure both the vector polarisation of the deuteron beam or hydrogen target and also the luminosity. After recording two charged particles, deuteron-proton pairs are separated from the remaining two-track events (mainly proton pairs) in the subsequent analysis by using the time information from the hodoscope. As demonstrated in Fig. 6.2 (left panel), if one assumes that both detected particles in the pair are protons, the calculated time of flight difference from the target (ΔT_c) do not match with the measured difference between the arrival times (ΔT_m) for non pp-pairs. By building the ($\Delta T_m - \Delta T_c$) difference (right panel of Fig. 6.2) particle pairs with correctly assumed types were clearly identified at zero. After recognising the two charged particles, the missing-mass distributions allowed us to identify corresponding reactions.

The dp elastic process, which is kinematically well separated from other reactions (see Fig. 6.1), is clearly identified on the momentum spectrum, with no background.

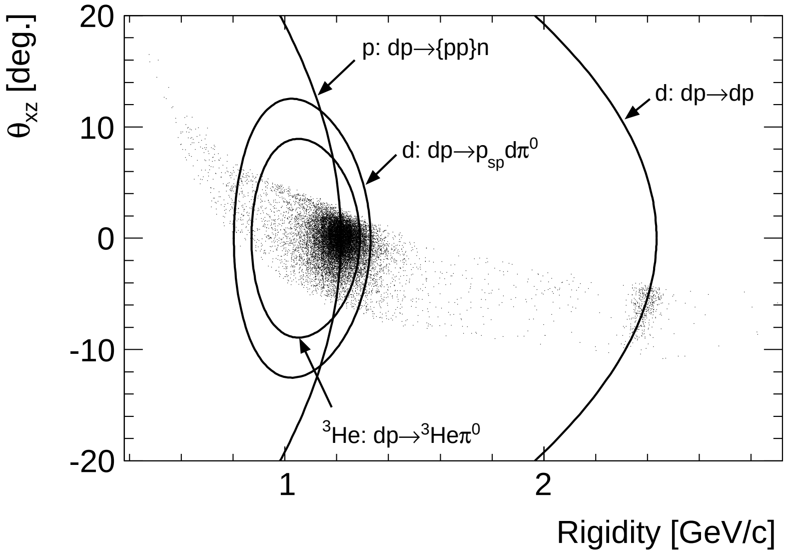

Figure 6.1: Scatter plot of singly charged particles detected in ANKE from the interaction of 1.2 GeV deuterons with a hydrogen cluster-jet target in terms of the laboratory production angle in the horizontal plane and the magnetic rigidity. The loci corresponding to four common nuclear reactions are also shown. These include the $dp \to \{pp\}_s n$ reaction at zero E_{pp}.

This process was used several times to cross check the final results on polarimetry and luminosity. Furthermore, this is also an useful reaction for the geometry calibration procedure.

6.4 Geometry calibration

The precision of the momentum and angle reconstruction is directly related to the accuracy of the ANKE geometry measurement. Positions and sizes of different parts of the ANKE spectrometer are well defined and fixed, but there are some parameters in the track reconstruction software that change from one beam time to another and it is not possible to measure them directly with enough precision. One is the beam-target overlap point position transverse to the beam. Another important parameter is the beam inclination angle from the nominal COSY orbit (see section 4.2). Of course, the inclination angle α of the ANKE platform is always measured, but the actual beam angle can slightly differ from α, due to the displacement of the COSY

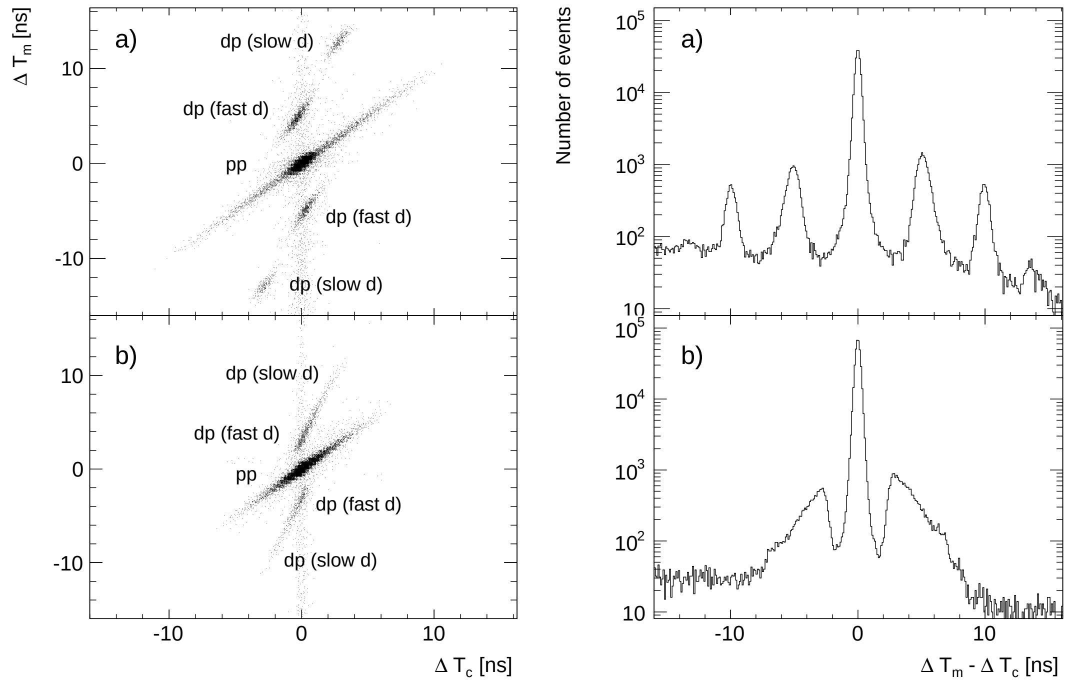

Figure 6.2: Scatter plot (left) of measured (ΔT_m) and calculated (ΔT_c) time differences between pairs of charged particle registered in the ANKE forward detector at a) T_d = 1.2 GeV and b) T_d = 2.27 GeV. ΔT_c was calculated assuming that both particles were protons, which resulted in ($\Delta T_m - \Delta T_c$), shown in the right panel.

beam orbit. Uncertainties in these parameters shift the reconstructed particle momenta, which therefore result in shifts in mass distributions of the missing particles. For example, in the 2009 data the beam was moved by 2 mm in the transverse direction, which resulted in a 15 MeV/c^2 shift in the neutron mass in the $dp \to \{pp\}_s n$ reaction at 1.2 GeV. Hence, the only way to correctly determine these parameters is to fit them, using the kinematics of different reactions. The fitting software takes preselected events (including track hit information) for different reactions as an input. For every iteration of the fitted parameters, the program reconstructs tracks from scratch and looks at the displacement of the missing masses from their nominal values for every reaction. In reactions with no missing particles, total energy and three-momentum conservation laws are employed separately. In our data the following reactions were used for the geometry calibration: $dp \to \{pp\}_s n$, $dp \to p_{\rm sp} d\pi^0$ (with fast and slow deuteron branches) and $dp \to dp$. The calibration was performed for each flat top separately.

Chapter 7

Cross section determination

This chapter describes the cross section determination procedure for the $dp \to \{pp\}_s n$ reaction at $T_d = 1.2$, 1.6, 1.8 and 2.27 GeV. The cross section analysis requires a precise normalisation to obtain absolute values. The luminosity was determined by using the $dp \to p_{\rm sp} d\pi^0$ (quasi free $np \to d\pi^0$) reaction at all energies. Monte Carlo simulations were performed for both reactions to account for the limited acceptance of the ANKE FD.

7.1 Basic concept

The cross section σ for a given physical process is given in terms of the corresponding counting rate R and the luminosity L through:

$$\sigma = \frac{R}{L}\,. \tag{7.1}$$

The luminosity, which is the product of the target density and beam intensity, can be measured in various ways. In the current analysis we relied on the measurement in parallel of the rate for a process with a well-known and sizeable cross section. Once the luminosity is known, absolute values of cross sections for other reactions can be deduced from the count rates measured in the experiment.

The measured count rate of any reaction is affected by several factors. In most cases detector geometry and electronics do not allow one to detect all events produced from the beam-target interactions. Therefore, in order to measure luminosity and/or the cross section of a reaction, one needs to reconstruct the total number of events by taking into account all the effects listed below:

1. Track reconstruction efficiency - the ratio of a number of reconstructed tracks to the number of hit particles. Although, the track reconstruction efficiency is close to unity, it should be taken into the account.

2. The data acquisition system introduces some dead time, which limits the system efficiency by rejecting some part of produced triggers (see Section 5.4). This effect increases with the total trigger rate. The average DAQ efficiency is usually determined by comparing the number of all written triggers with the total number of produced triggers, which are separately counted by scalers.

3. Detector geometric acceptance determination - the most difficult part. For reactions with two and more tracks a Monte Carlo simulation is used, which requires detailed detector geometry and an exact description of the experimental conditions as input.

7.2 The $dp \to p_{\rm sp} d\pi^0$ reaction

7.2.1 Reaction identification and background estimation

The $dp \to p_{\rm sp} d\pi^0$ reaction was used in the luminosity determination in our experiments. This reaction is identified in the ANKE forward detector by detecting both charged particles (see Figures 6.1 and 6.2). After recognising the dp pairs, the reaction is finally isolated on the basis of the missing-mass distributions [31].

At intermediate energies, soft deuteron collisions are generally dominated by the interaction of one of the nucleons in the nucleus, the other nucleon being a spectator. When the proton acts as a spectator, $p_{\rm sp}$, the $dp \to p_{\rm sp} d\pi^0$ reaction can be interpreted in terms of quasi-free $np \to d\pi^0$ pion production. To confirm the spectator hypothesis, a Monte Carlo simulation has been performed within PLUTO [64] using the Fermi momentum distribution from the Paris deuteron wave function [65]. As is demonstrated in Fig. 7.1, the data are consistent with quasi-free production on the neutron leading to a spectator proton. However, in order to reduce further

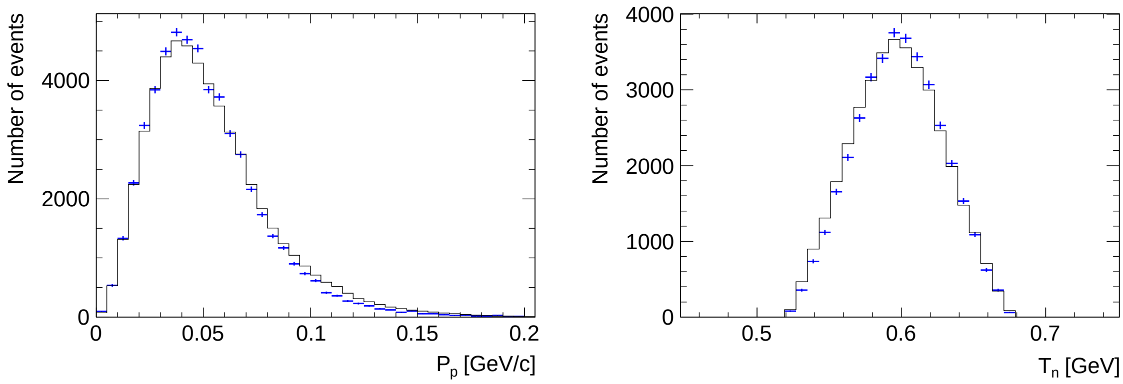

Figure 7.1: The momentum distribution of the fast proton from the $dp \to p_{sp} d\pi^0$ reaction at $T_d = 1.2$ GeV (left panel), transformed into the rest frame of the incident deuteron, and the resulting kinetic energy of the incident neutron in the laboratory system (right panel). The corresponding Monte Carlo simulations are shown as solid histograms.

possible contributions from multiple scattering and other mechanisms, only events below 60 MeV/c were retained for the luminosity evaluation.

Isospin invariance requires the cross section for $np \to d\pi^0$ to be half of that for $pp \to d\pi^+$, for which there are numerous measurements [66]. An additional advantage of using this reaction for normalisation is that the typical 5% shadowing effect in the deuteron (where one nucleon hides behind the other) should be broadly similar in the $dp \to \{pp\}X$ and $dp \to p_{sp} d\pi^0$ reactions.

The determination of the angles for the quasi-free $np \to d\pi^0$ reaction is complicated by the Fermi motion of the nucleons inside the deuteron. Due to this effect, the effective neutron beam energy, T_n, is spread around half the deuteron beam energy with a width arising from the Fermi momentum. At a beam energy of 600 MeV per nucleon, the FWHM is 90 MeV for a $p_{sp} < 60$ MeV/c cut. Furthermore, the neutron direction is not precisely aligned along that of the beam, but is spread over some solid angle. Since this introduces an incident angle, which is several degrees in the laboratory system (depending on the beam energy), it has to be taken into account. These considerations apply to both the polar and azimuthal angles. In order to correct for this effect, the three-momentum of the incident neutron was reconstructed using the information from the spectator-proton momentum. The deuteron polar angle was measured from the neutron momentum instead of the beam direction. The azimuthal angle was defined between the normals to the COSY ring and deuteron scattering plane.

The missing-mass spectra in Fig. 7.2 (left panel) of detected fast deuterons from the $np \to d\pi^0$ reaction clearly show the existence of some background, especially at high energies. This is an accidental background at very small $|\Delta T_c|$ that is randomly distributed in ΔT_m (see Figure 6.2). This is caused by fast particles, mainly protons, that are produced in a different beam-target interaction. The contribution from such accidental events in the vicinity of the fast deuteron branch of the $dp \to p_{\text{sp}} d\pi^0$ reaction increases rapidly with energy. It varies between 18% and 30% for $T_d \geq 1.6$ GeV, whereas it is less then 3% at 1.2 GeV. The analogous background is negligible at all energies for the slow deuteron branch.

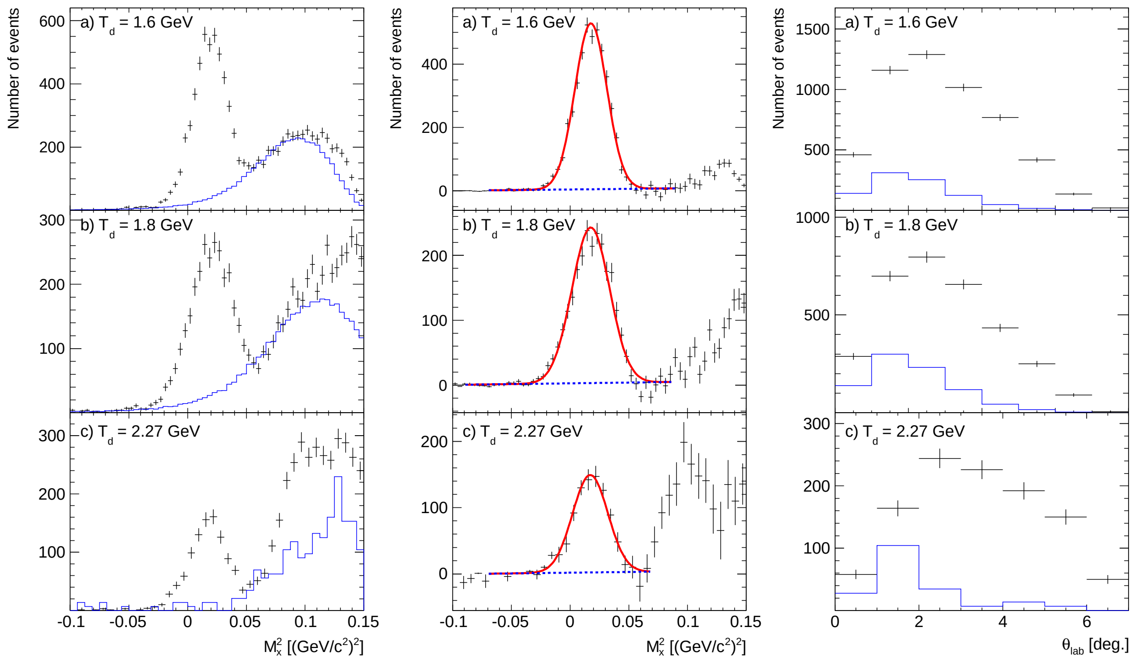

Figure 7.2: Missing-mass distributions for the dp (fast deuteron) events at three different energies before (left) and after (middle) background subtraction. Background distributions are shown as solid histograms. Right panel shows the angular distribution of the background events.

The properties of the background were studied using the data for which $|\Delta T_c| <$ 2 ns and $|\Delta T_m| >$ 12 ns. As can be seen in Fig. 6.2, no true coincidence two-track events are expected in this region. These data were analysed with exactly the same analysis procedure as used for $dp \to p_{\text{sp}} d\pi^0$, to obtain the shape of background in the distributions of the missing mass and the deuteron laboratory scattering angle in the $dp \to p_{\text{sp}} d\pi^0$ reaction. As demonstrated in Fig. 7.2 (right panel), the background shows a rather strong dependence on the laboratory scattering angle. Hence, it is necessary, not only to account for the total level of the background, but for its shape also. The normalisation for the background was found by comparing the background missing-mass spectra with those for the identified dp pairs. In order to check the reliability of the normalisation, the background was subtracted from the missing-mass spectrum, which was then fitted with the sum of Gaussian and Polynomial, as shown in the middle panel of Fig. 7.2. The remaining background at a percent level was included as an uncertainty in the remaining data. The normalised background was also subtracted from the $dp \to p_{\rm sp} d\pi^0$ angular distributions.

7.2.2 Monte Carlo simulation

In order to investigate the acceptance of the ANKE forward detector for different reactions, a full simulation was performed based on GEANT software [67]. As mentioned in the previous section, the spectator model was used in the simulation. It was already demonstrated in Fig. 7.1, that the energy of incident neutrons varies significantly in the quasi-free $np \to d\pi^0$ process. Since the cross section of this process depends rather strongly on the energy, it became necessary to either use very strict cuts on the neutron kinetic energy or account for the cross section energy dependence. Shrinking the allowed energy range for incident neutrons would also reduce the statistics and the luminosity measurement accuracy, which at higher energies would not be acceptable. Therefore, the second option was preferred.

The cross section of the $pp \to d\pi^+$, which is higher than that for $np \to d\pi^0$ by an isospin factor of two, was obtained from the SAID data base [66] as a function of two variables, T_n and $\theta_{\rm lab}$ of the fast and slow deuterons separately. These are shown in Fig. 7.3. The simulated events were weighted with this cross section in subsequent analyses.

The same track-reconstruction algorithm was used in the simulation and the data analysis. In order to get as precise a description of the experiment as possible, the dispersion of the hits in the MWPC, the background hits produced by accidental coincidences, and the noise in the multiwire chambers readout electronics, as obtained from the experimental data, were also included in the simulation [62]. The quality of the simulation may be judged from the distributions of the deuteron production angle in the laboratory system that are shown in Fig. 7.4.

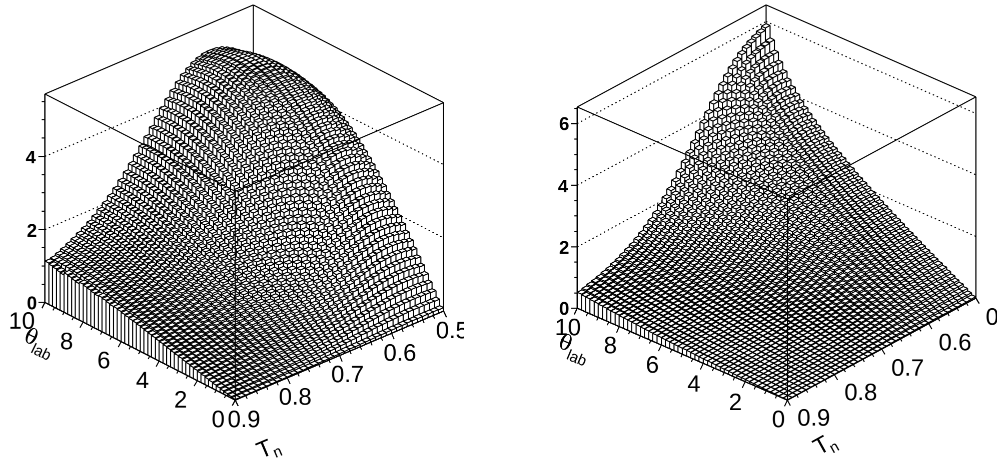

Figure 7.3: Differential cross section $d\sigma/d\vartheta$ (mbarn/radian) of the $np \to d\pi^0$ reaction for fast (left) and slow (right) deuterons as a function of the deuteron laboratory polar angle θ and kinetic energy of the incident neutron T_n.

7.2.3 Luminosity measurement

To determine the luminosity we used Eq. (7.1) and inserted detailed expressions for R and σ:

$$L = \frac{R}{\sigma} = \frac{R_{\text{exp}}\,(N_{\text{tot}}/N_{\text{acc}})}{\iint \frac{d\sigma}{d\vartheta}(\vartheta, T_n)\,d\vartheta\,dT_n}\,, \tag{7.2}$$

where R_{exp} is the count rate from the quasi-free $np \to d\pi^0$ reaction, corrected for the trigger dead time. N_{acc} is the number of counts in the simulation that pass all the criteria used in the experimental data processing and N_{tot} is the total number of simulated events. These are summed over the neutron kinetic energy, subject to the $p_{\text{sp}} < 60$ MeV/c cut, and over the given angular range.

The FD detector acceptance changes rapidly with polar angle. In order to minimise systematic errors, the total angular range was binned and the luminosity evaluated separately for each bin. Data at the acceptance edges (the smallest and the largest angles) were less reliable, due to the greater uncertainty in the evaluation of the acceptance, and showed systematic shifts in luminosity. Such angular intervals were discarded and the average recomputed.

The values of the average luminosities determined from the $np \to d\pi^0$ reaction are given in Table 7.1. The errors quoted include statistical ones from the experimental counts and those introduced by the background subtraction procedure. Uncertainties coming from the SAID database [66], which were estimated by studying the

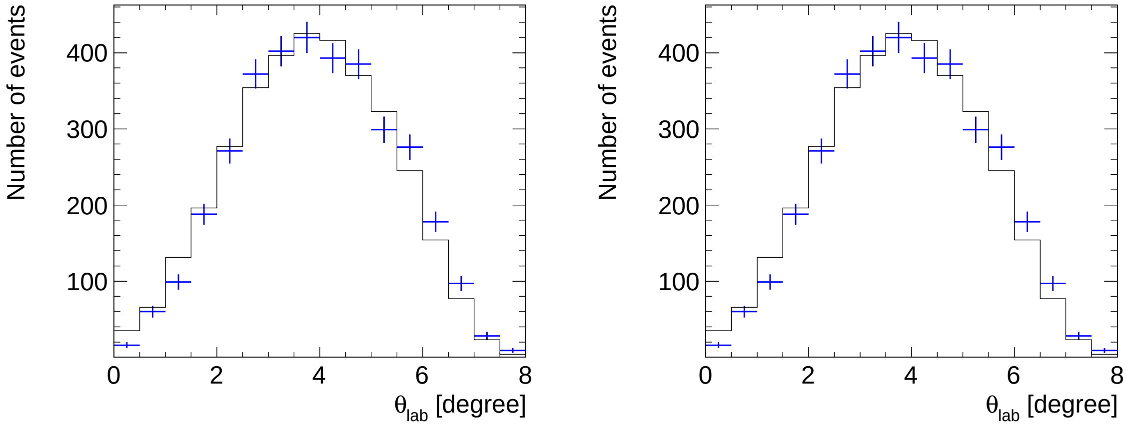

Figure 7.4: Simulated (solid histogram) and experimental angular distributions for the $dp \to p_{sp}d\pi^0$ reaction at $T_d = 1.2$ GeV. The left and right panels correspond to fast and slow deuterons, respectively.

experimental results in the relevant regions, are listed separately.

T_d [GeV]	Average luminosity [$\mathrm{cm}^{-2}\ \mathrm{s}^{-1}$]	Measurement uncertainty [%]	SAID uncertainty [%]
1.2	1.76×10^{30}	1.1	2.2
1.6	1.84×10^{31}	2.0	5.1
1.8	1.61×10^{31}	2.8	4.4
2.27	1.18×10^{30}	5.0	3.8

Table 7.1: Average luminosities achieved with the cluster-jet target at four different beam energies. Shown separately are the uncertainties associated with the measurement and with the experimental data used as input in the estimations.

7.3 The $dp \to \{pp\}_s n$ reaction

7.3.1 Reaction identification and background estimation

Having identified two fast protons in the final state and selected low E_{pp} events, the $dp \to \{pp\}_s n$ reaction was isolated on the basis of the missing-mass distributions, which are shown at three energies in Fig. 7.5. In addition to the dominant neutron peak, there are also many events for $M_X > 1080$ MeV/c^2 that must correspond to pion production (more about this channel is to be found in chapter 10). However, very few of these leak into the neutron region and the background from this under the neutron peak is at most at the per cent level. In addition, there is an accidental background arising from a different beam-target interaction (the same background as was mentioned for the $dp \to p_{\rm sp} d\pi^0$ reaction). In 2006 such background was negligible. But in 2005 the luminosity was much higher, which resulted in a significantly increased accidental background. Hence, the level of the background had to be estimated and subtracted from the final cross section results.

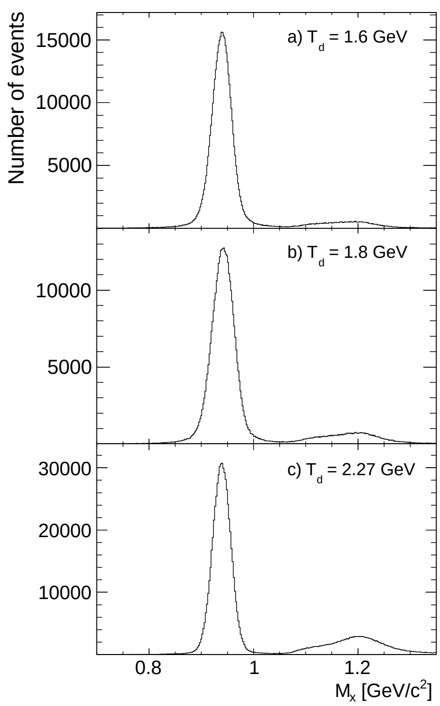

Figure 7.5: The missing-mass M_X distributions for the $dp \to \{pp\}_s X$ reaction at three deuteron beam energies. The background under the neutron peak is negligible.

The accidental background for the $dp \to \{pp\}_s n$ reaction was studied using the arrival time difference between the two protons. It is clearly seen in Fig. 6.2 that the peaks in the $\Delta T_m - \Delta T_c$ spectrum, corresponding to pp and dp pairs, are rather distant. This allowed us to use a broader cut on the pp peak during the reaction identification and maintain the background events outside the $(-3\sigma, +3\sigma)$ interval. In the final stage of the analysis such distributions were built again for the selected events being used in the cross section determination and fitted with a Gaussian plus constant function to estimate the background level. The large statistics of $dp \to \{pp\}_s n$ events made it possible to repeat this procedure for different q ranges/bins and obtain the background behaviour with momentum transfer. Results at $T_d = 1.8$ GeV, where the background level was the highest, are shown in Fig. 7.6 as an example. This background was then subtracted from the final cross section result.

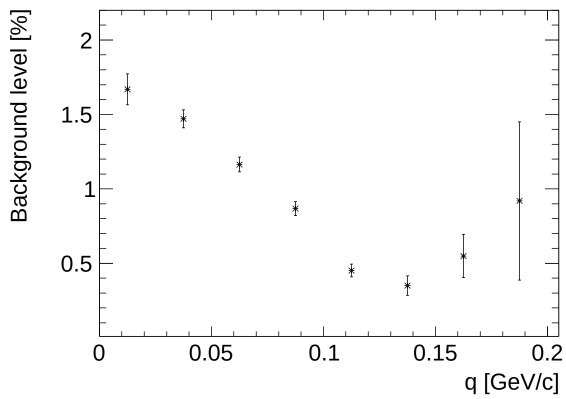

Figure 7.6: The accidental background for the $dp \to \{pp\}_s n$ reaction at different momentum transfers at $T_d = 1.8$ GeV. This was obtained using the time information from the FD hodoscope.

7.3.2 Monte Carlo simulation

The $dp \to \{pp\}_s n$ reaction has a three-body final state. Hence, five variables are needed to describe the kinematics of this process. In principle, the cross section and the detector acceptance are functions of the five independent variables. In order to simulate the process we used the following ones:

- E_{pp} – the excitation energy of the two protons. $E_{pp} = k^2/m_p = m_{2p} - 2m_p$, where k is a relative momentum of the protons.

- $\cos\theta_{pp}^{cm}$ – the cosine of the polar angle of the diproton in the overall cm system. It is directly related to the three-momentum transfer q.

- ϕ_{pp}^{cm} – the azimuthal angle of the diproton in the overall cm system.

- $\cos\theta_{k}^{cm}$ – the polar angle of the proton in cm system of two protons.

- ϕ_{k}^{cm} – the azimuthal angle of the proton in cm system of two protons.

However, within the impulse approximation, by far the most important of these for very low E_{pp} are the excitation energy E_{pp} in the final pp diproton and the momentum transfer q from the proton to the neutron. Since only the unpolarised state of the beam was used for the cross section determination, the ϕ_{pp}^{cm} dependence was omitted. Furthermore, in our conditions the E_{pp} excitation energy is so small that the ${}^1S_0$ state dominates and the contamination from higher partial waves is severely limited. As could be checked with the impulse approximation program, under these conditions the dependence on the $\cos\theta_{k}^{cm}$ and ϕ_{k}^{cm} was very weak and could be easily neglected.

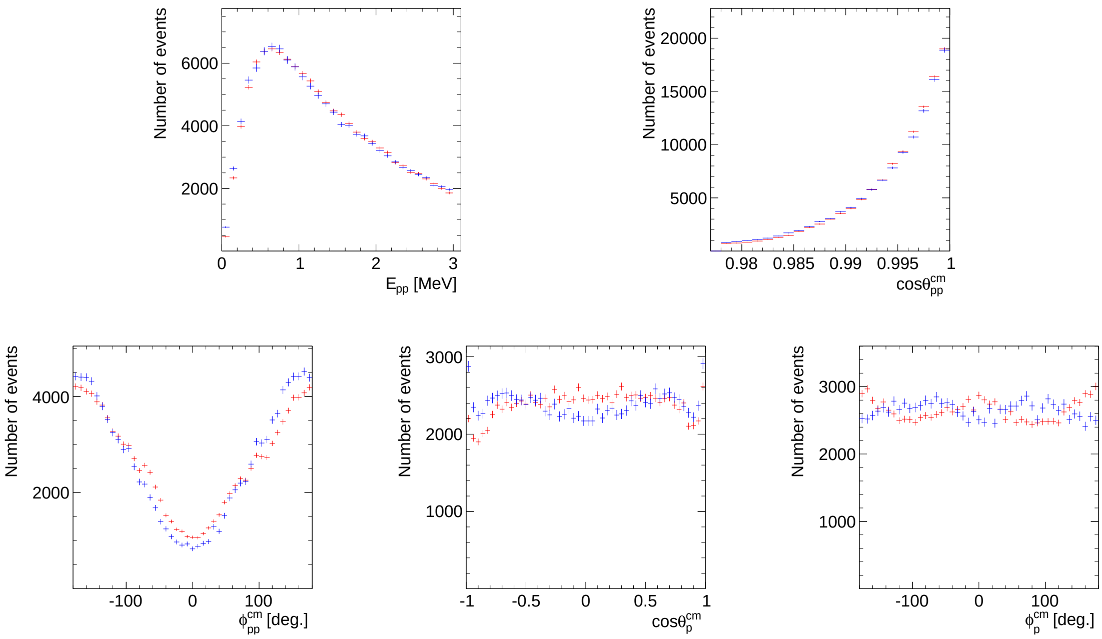

Figure 7.7: Simulated (blue) versus experimental (red) distributions of different kinematical parameters of the $dp \to \{pp\}_s n$ reaction at $T_d = 1.2$ GeV. Simulated events are weighted with $d^2\sigma(q, E_{pp})/dqdE_{pp}$.

It was shown in earlier studies at ANKE that the detector acceptance for the proton-proton pairs could be described sufficiently well [68]. The FD detector acceptance for the $dp \to \{pp\}_s n$ reaction was measured as function of q and E_{pp}. For this all the five variables were generated uniformly. Figure 7.7 shows simulated and experimental distributions of all these five variables. In order to account for migration effects between different bins, simulated events were weighted with a two dimensional differential cross section $d^2\sigma(q, E_{pp})/dqdE_{pp}$, obtained from the impulse approximation predictions. The resulting tracks were traced through ANKE using the GEANT software [67]. The total number of generated events N_{tot}, as well as accepted traced events N_{acc}, which passed all the cuts used in the data analyses, were stored in two-dimensional histograms. The acceptance coefficients for different q and E_{pp} bins were determined by

$$A(q, E_{pp}) = \frac{N_{\mathrm{acc}}(q, E_{pp})}{N_{\mathrm{tot}}(q, E_{pp})}\,. \tag{7.3}$$

In such a way, the two dimensional acceptance maps were obtained at all energies. An example of such map is shown in Fig. 7.8 at one particular energy.

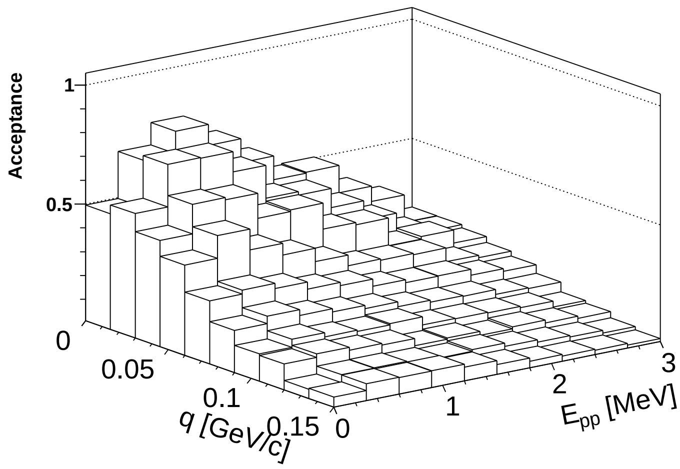

Figure 7.8: ANKE FD acceptance (q, E_{pp}) map for the $dp \to \{pp\}_s n$ reaction at $T_d =$ 1.2 GeV.

The optimal bin widths for q and E_{pp} were determined by considering the corresponding resolution in these variables. In order to determine the resolution in the excitation energy of the diproton and the transferred momentum, simulated events were analysed before and after passing the track-reconstruction algorithm. The differences between the original and reconstructed values of these observables were studied for different ranges. The resolutions in q and E_{pp} are about $4-8$ MeV/c and better than 0.3 MeV, respectively.

7.3.3 Differential cross section

The $dp \to \{pp\}_s n$ cross section determination was performed in a similar manner to the luminosity evaluation that used the $dp \to p_{\rm sp} d\pi^0$ reaction. It involved the same technique for correcting the experimental count rates. In accordance with Eq. (7.1), the two-dimensional differential cross section was evaluated in terms of the integrated luminosity $L_{\rm int}$ from:

$$\frac{d^2\sigma(q,E_{pp})}{dq\,dE_{pp}} = \frac{1}{L_{\rm int}}\,\frac{N_{\rm exp}(q,E_{pp})\,N_{\rm tot}(q,E_{pp})}{N_{\rm acc}(q,E_{pp})\,\Delta q\,\Delta E_{pp}}\,, \tag{7.4}$$

where $N_{\rm exp}(q,E_{pp})$ is the corrected number of experimental events for given values of q (measured in the laboratory system) and E_{pp}. $N_{\rm tot}(q,E_{pp})$ and $N_{\rm acc}(q,E_{pp})$ are the total and accepted numbers of simulated events respectively. Δq and ΔE_{pp} correspond to bin widths in momentum transfer and excitation energy, respectively.

The cross sections were further integrated over $E_{pp} < 3$ MeV in order to provide the $d\sigma/dq$ differential distribution presented in Fig. 7.9. This figure includes also the new results obtained at $T_d = 1.2$ GeV. In addition to the statistical errors arising from the experimental count rates that are shown, there are also overall systematic uncertainties arising from the luminosity determinations given in the Table 7.1. Within these uncertainties, the agreement with the theoretical impulse approximation predictions [38] at $T_d = 1.2$, 1.6, and 1.8 GeV is very encouraging and is in line with similar data analysed at 1.17 GeV [31]. In contrast, the unpolarised differential cross section at $T_d = 2.27$ GeV falls about 15% below the predictions based upon the current $np \to pn$ partial wave analysis [1]. As we shall see later, similar discrepancies are found in the spin observables of the $dp \to \{pp\}_s n$ reaction but only at this highest energy.

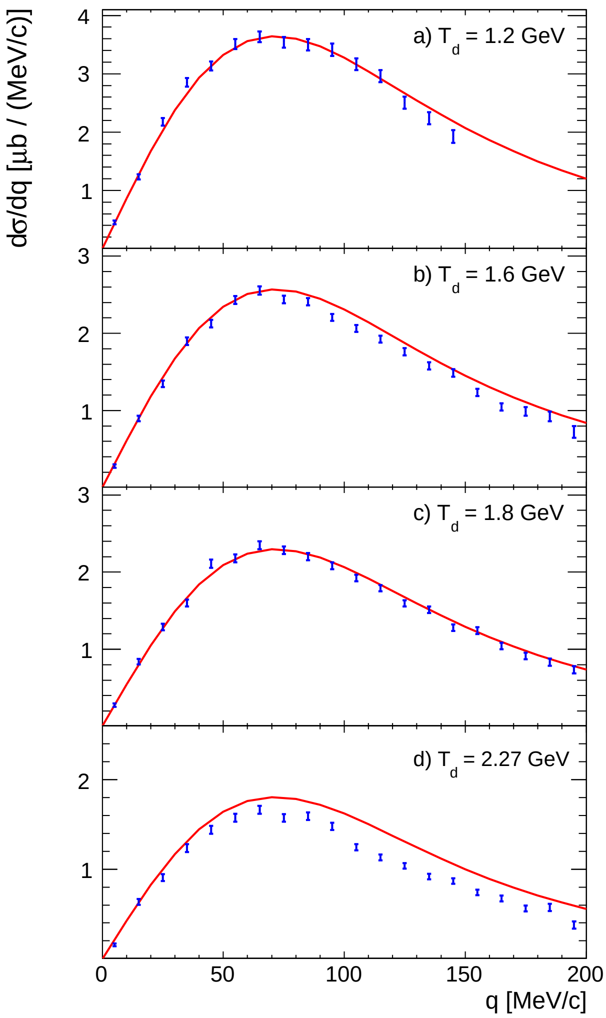

Figure 7.9: Differential cross sections for the $dp \to \{pp\}_s n$ reaction at four different energies compared with impulse approximation predictions based upon the current SAID $np \to np$ amplitude analysis [1] (numerical values are listed in Table B.2). The data are integrated over the $E_{pp} < 3$ MeV interval. Only statistical errors are shown; Systematic uncertainties are listed in Table 7.1.

Chapter 8

Polarimetry at ANKE

In order to measure different spin observables for the $\vec{d}p \to \{pp\}_s n$ or any other reaction, the first step has to be the identification of the polarisations of the various deuteron beam states used in the experiment. With complete efficiencies in the transition units, the polarisations should approach the ideal values given in Table 5.1. However, this is never the case in practice and the beam polarisation must be determined separately for each of the beam states used. The accuracy of the beam and/or target polarimetry, in principle, defines the precision of the measured spin observables. This chapter describes methods of measuring the deuteron beam and hydrogen target polarisations at ANKE.

8.1 Polarised cross section

At first it is necessary to define the "scattering frame", or the so-called Madison Frame, which will help us to simplify the presentation of complex polarisation effects. The scattering frame is a Cartesian coordinate system (x, y, z) with the z-axis along the momentum of the incident particle $\vec{p}_{\text{in}}$, the y-axis in the direction of $\vec{p}_{\text{in}} \times \vec{p}_{\text{out}}$, where the $\vec{p}_{\text{out}}$ is the momentum of the scattered particle, and the x-axis defined by a right-handed coordinate system.

Now we will discuss how the differential cross section depends on the polarisations of beam and target. This will be done for elastic scattering of polarised deuterons from the polarised protons, but all the derived dependence can be generalised for any polarised spin-1 particle scattering from polarised spin-$\frac{1}{2}$ particles. The differential

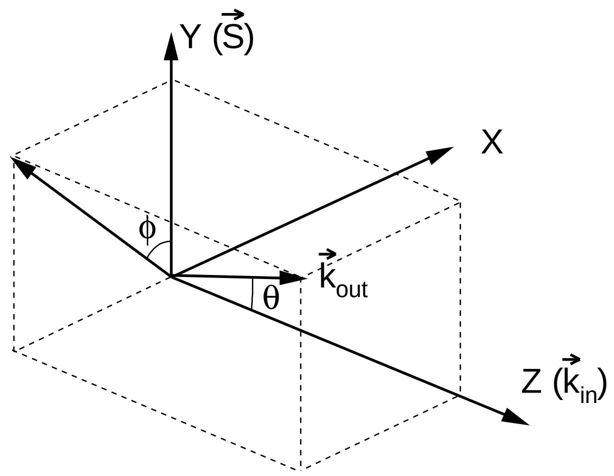

Figure 8.1

cross section $d\sigma$ for elastic scattering, in terms of the unpolarised differential cross section $d\sigma_0$, is given as follows [16, 69]:

$$
\begin{aligned}
\frac{d\sigma}{d\sigma_0} = 1 \quad &+ \quad Q_y A_y^p + \frac{3}{2} P_y A_y^d + \frac{2}{3} P_{xz} A_{xz} + \frac{1}{3}(P_{xx} A_{xx} + P_{yy} A_{yy} + P_{zz} A_{zz}) \\
&+ \quad \frac{3}{2}(P_x Q_x C_{x,x} + P_x Q_z C_{x,z} + P_y Q_y C_{y,y} + P_z Q_x C_{z,x} + P_z Q_z C_{z,z}) \\
&+ \quad \frac{1}{3}(P_{xx} Q_y C_{xx,y} + P_{yy} Q_y C_{yy,y} + P_{zz} Q_y C_{zz,y}) \\
&+ \quad \frac{2}{3}(P_{xy} Q_x C_{xy,x} + P_{xy} Q_z C_{xy,z} + P_{xz} Q_y C_{xz,y} + P_{yz} Q_x C_{yz,x} + \\
&\qquad P_{yz} Q_z C_{yz,z}) \ ,
\end{aligned} \tag{8.1}
$$

where

- Q_i - proton (target) polarisation components,
- P_i - deuteron (beam) vector polarisation components,
- P_{ik} - Cartesian moments of the deuteron (beam) tensor polarisation,

- A_y^p - proton analysing power,
- A_y^d - deuteron analysing power,
- A_{ik} - components of the tensor analysing power,
- $C_{i,k}$ - vector-vector spin correlation coefficients,
- $C_{ik,l}$ - tensor-vector spin correlation coefficients (i, k, l can be any of the x, y, z).

The A_y^p, A_y^d, A_{ik}, $C_{i,k}$, $C_{ik,l}$ observables are functions of scattering angle θ. In Eq. (8.1) the constraints of parity conservation have been taken into account. In addition, the following relations also apply here:

$$P_{xx} + P_{yy} + P_{zz} = A_{xx} + A_{yy} + A_{zz} = C_{xx,y} + C_{yy,y} + C_{zz,y} = 0\,. \tag{8.2}$$

In order to characterise an polarised ensemble of particles, an axis of rotational symmetry $\vec{s}$, also called the 'spin-alignment axis' should be known. Usually the spin-alignment axis of the polarised beam and/or target produced in atomic beam sources is defined by the experimental apparatus and is always fixed in the laboratory system. For spin-$\frac{1}{2}$ particles only two projections of the spin are available. If we denote by n^+ and n^- the populations of the two magnetic substates with projections $+1$ and -1 with respect to a quantisation axis in the direction of $\vec{s}$, the vector polarisation of the ensemble is then given by:

$$P_\xi = \frac{n^+ - n^-}{n^+ + n^-}\,. \tag{8.3}$$

For spin-1 particles the state with 0 projection is also possible, which leads to tensor polarisation components:

$$P_{\xi\xi} = \frac{n^+ + n^- - 2n^0}{n^+ + n^0 + n^-}\,, \tag{8.4}$$

where the n^0 is the population of the magnetic substates with projections 0. The equations (8.3) and (8.4) lead to the theoretical limits for the vector and tensor polarisation values of $-1 < P_\xi < +1$ and $-2 < P_{\xi\xi} < +1$, respectively.

The reaction frame is defined by the $\vec{p}_{\text{in}} \times \vec{p}_{\text{out}}$ and is therefore specific for each event. Since the orientation of the spin alignment axis $\vec{s}$ is fixed in the laboratory system, this makes the vector and tensor polarisation components vary from event to event in the reaction frame. In order to make relations between polarisations in different systems, let us consider that the spin alignment axis is determined as $\vec{s}(\beta,\phi)$ in the laboratory system (X,Y,Z). The reaction frame is rotated from the laboratory system around the Z-axis (direction of the $\vec{p}_{\rm in}$) by an azimuthal angle φ of the $\vec{p}_{\rm out}$, as demonstrated in Fig. 8.1. This will be referred as "fixed frame" in the future.

In the above example of elastic $\vec{d}\vec{p}$ scattering the polarisations of the deuteron beam and proton target, in the fixed frame, are specified by $\vec{P}(\beta_d,\varphi_d)$ and $\vec{Q}(\beta_p,\varphi_p)$ vectors, respectively. This leads to the following relations:

$$
\begin{aligned}
Q_x &= Q\sin\beta_p\cos(\phi_p-\varphi)\,, & P_{xy} &= \frac{3}{4}P_{\xi\xi}\sin^2\beta_d\sin 2(\phi_d-\varphi)\,,\\
Q_y &= Q\sin\beta_p\sin(\phi_p-\varphi)\,, & P_{yz} &= \frac{3}{4}P_{\xi\xi}\sin 2\beta_d\sin(\phi_d-\varphi)\,,\\
Q_z &= Q\cos\beta_p\,, & P_{xz} &= \frac{3}{4}P_{\xi\xi}\sin 2\beta_d\cos(\phi_d-\varphi)\,,\\
P_x &= P_\xi\sin\beta_d\cos(\phi_d-\varphi)\,, & P_{zz} &= \frac{1}{2}P_{\xi\xi}(3\cos^2\beta_d-1)\,.\\
P_y &= P_\xi\sin\beta_d\sin(\phi_d-\varphi)\,, & &\\
P_z &= P_\xi\cos\beta_d\,, & &
\end{aligned}
\tag{8.5}
$$

The stable spin axis is provided by the magnetic field at COSY, which is perpendicular to the beam orbit. Because of that, the COSY laboratory system is defined in a similar way to the above-mentioned fixed frame. In the single-polarised experiments of 2005 and 2006 only the deuteron beam was polarised. This significantly simplifies the differential cross section of Eq. (8.1). Taking into account that $\beta_d=\phi_d=\frac{\pi}{2}$ and using relations (8.2), Eq. (8.1) simplifies to:

$$
\begin{aligned}
\frac{d\sigma(\vartheta,\varphi)}{d\sigma_0(\vartheta)} = 1 \;&+\; \frac{3}{2}P_\xi A_y^d(\vartheta)\cos\varphi\\
&+\; \frac{1}{4}P_{\xi\xi}\left[A_{xx}(\vartheta)(1-\cos 2\varphi)+A_{yy}(\vartheta)(1+\cos 2\varphi)\right]\\
&+\; \frac{1}{4}P_{\xi\xi}Q\Big[(\frac{1}{2}C_{xx,y}(\vartheta)+\frac{1}{2}C_{yy,y}(\vartheta)+C_{xy,x}(\vartheta))\cos\varphi\\
&\qquad +(\frac{1}{2}C_{xx,y}(\vartheta)-\frac{1}{2}C_{yy,y}(\vartheta)+C_{xy,x}(\vartheta))\cos 3\varphi\Big]\,,
\end{aligned}
\tag{8.6}
$$

where ϑ is a polar angle. The vector (P_ξ) and tensor ($P_{\xi\xi}$) polarisations are aligned along the Y-axis (perpendicular to the COSY plane). We will denote them later as P_Y and P_{YY} for simplicity.

It can be seen from Fig.4.3 that the FD of the ANKE spectrometer has an asymmetric acceptance with respect to the azimuthal φ angle. The only way to measure the polarisation under such conditions is to compare the polarised and unpolarised data. This has some advantages over other methods. The ratio $d\sigma/d\sigma_0$ of Eq. (8.6) provides a direct relation between the polarisation and analysing powers of the reaction. By taking the ratio of the two data sets, most of the systematic effects, such as detector geometric acceptance and track reconstruction efficiency, cancel out. This is very important feature, not only for polarimetry purposes, but is also very useful while studying different spin observables. The main disadvantage of the method is that the polarisation is always measured with respect to the unpolarised state and can lead to some inefficiencies if a residual polarisation is present.

Generally, the luminosity L [cm^{-2} s^{-1}], which defines the counting rate of the given reaction R [s^{-1}] through its cross section σ, is a product of beam intensity I [s^{-1}] and target density n [cm^{-2}]:

$$L = I \cdot n = \frac{R}{\sigma}\,. \tag{8.7}$$

Hence, any change in the beam intensity or in the target density affects the luminosity and therefore the counting rate of the reaction. Considering Eq. (8.7), the cross section dependence on the polarisation of Eq. (8.6) can be applied directly to the counting rate ratios, but in this case it is necessary to normalise the polarised counting rate on the relative luminosity with respect to the unpolarised state, taking into account possible differences in data acquisition efficiencies between the two modes. Different methods of determination of the relative luminosities has been achieved at ANKE, and these are described in the next section.

8.2 The comparison of different normalisation methods

The standard method of the count normalisation, as used in the first experiment [31], is based on the Beam Current Transformer (BCT) signal provided by the COSY accelerator. The BCT signal is proportional to the COSY beam intensity and allows the measurement of relative beam intensities with a percent accuracy, since the orbit in the ring should be identical for the different polarisation modes. The cluster target [53] has demonstrated very high stability over many years of operation at COSY. The COSY polarised cycles during the single-polarised experiments in 2005 and 2006 lasted around five minutes. Since the density of the cluster target was considered to be very steady over such short periods of time, the relative beam intensities, provided by the BCT data, could be well approximated as the relative luminosities. Using the BCT signal, relative luminosities were determined by integrating the

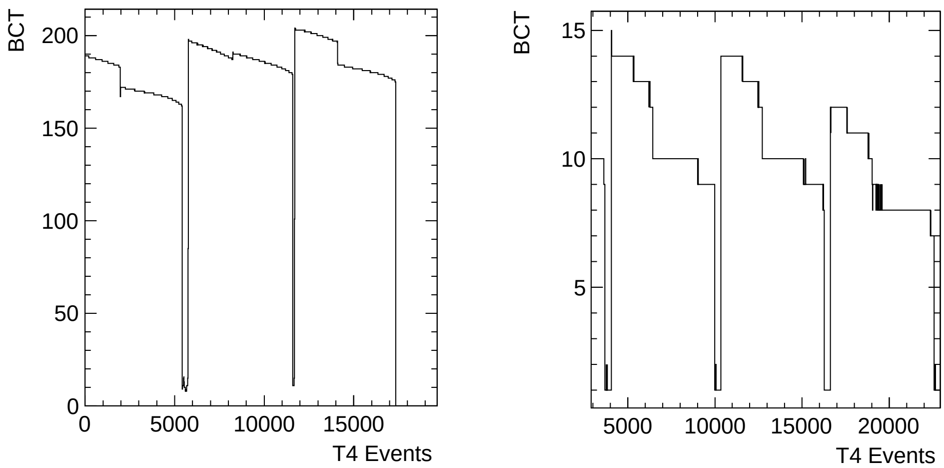

Figure 8.2: "Normal" BCT signal in the November 2003 beam time (left) and BCT signal in the November 2006 beam time (right)

beam current $I(t)$ over the total time:

$$\frac{L_{\rm pol}}{L_0} = \frac{\int I_{\rm pol}(t)dt}{\int I_0(t)dt} , \tag{8.8}$$

where $L_{\rm pol}$ and L_0 correspond to polarised and unpolarised integrated luminosities, respectively. In addition, experimental count rates were corrected for the DAQ efficiency for the selected trigger, separately for each polarisation mode, which was obtained by averaging the collected ($R_{\rm out}(t)$) and total ($R_{\rm in}(t)$) trigger rates, counted by scalers (see section 5.4 for more details).

$$\tau = \frac{\int R_{\rm out}(t)dt}{\int R_{\rm in}(t)dt} . \tag{8.9}$$

During the analysis of the November 2006 data an unrecoverable problem with the BCT signal was found. The problem with the digitisation of the BCT signal occurred due to technical reasons during the beam time. This resulted in a significantly poorer measurement accuracy (Fig. 8.2, right panel) of around 10 percent, which was largely insufficient for polarimetry and analysing power studies, and an alternative was required. The $dp \to p_{\rm sp} d\pi^0$ reaction (quasi–free $np \to d\pi^0$) counts at $\vartheta = 0°$ do not depend on the beam polarisation. The accuracy achieved when using this reaction depends mainly on the angular precision of the ANKE forward detector. This technique was investigated and found to be consistent with BCT, but it works well only at low energy ($T_d = 1.2$ GeV). The counting rate falls with energy so that at $T_d = 2.27$ GeV the statistics are almost one order less and do not provide any improvement in the accuracy achieved with the BCT method.

A much more robust method is provided by the $dp \to p_{\rm sp} X$ reaction. The number of single-track events is enormous (a few hundred million events in the 2006 beam time data) for all beam energies, which results in very small statistical uncertainty. The deuteron momentum density for beams polarised with $m = \pm 1$ and $m = 0$ is given by

$$\begin{aligned} \rho_{\pm 1}(\vec{p}) &= \bar{\rho}(p) + \Delta\rho(p)\, P_2(\cos\vartheta_s)\,, \\ \rho_0(\vec{p}) &= \bar{\rho}(p) - 2\Delta\rho(p)\, P_2(\cos\vartheta_s)\,, \end{aligned} \tag{8.10}$$

where, in terms of the $S-$ and $D-$state deuteron wave functions,

$$\begin{aligned} \bar{\rho}(p) &= 4\pi \left(\Psi_S(p)^2 + \Psi_D(p)^2\right)\,, \\ \Delta\rho(p) &= 4\pi \left(\sqrt{2}\Psi_S(p)\Psi_D(p) - \tfrac{1}{2}\Psi_D(p)^2\right)\,, \end{aligned} \tag{8.11}$$

where ϑ_s is the angle with respect to the quantisation axis, aligned along the Y direction. Equation (8.4) leads to

$$P_{YY} = \frac{2r - 2}{2r + 1}\,, \tag{8.12}$$

where r is a ratio of populations of substates ($|m| = 1$) and ($m = 0$).

The dependence of the Fermi motion on polarisation is therefore given by

$$\begin{aligned} \rho(\vec{p}) &= \tfrac{1}{6}\left[2\,(2 + P_{YY})\,\rho_{\pm 1}(\vec{p}) + (2 - 2P_{YY})\,\rho_0(\vec{p})\right] \\ &= \bar{\rho}(p) + P_{YY}\,\Delta\rho(p)\, P_2(\cos\vartheta_s)\,. \end{aligned} \tag{8.13}$$

This should be converted into angles with respect to the beam direction. For that we use

$$P_2(\cos\vartheta_s) = \tfrac{1}{2}(3\cos^2\vartheta_s - 1) = \tfrac{1}{2}(3y^2/r^2 - 1)\,, \tag{8.14}$$

where, for a standard spherical coordinate system,

$$y = \sin\vartheta\sin\varphi\,, \tag{8.15}$$

which leads to the final result:

$$\rho(\vec{p}) = \bar{\rho}(p) - W(\vartheta,\varphi)\,P_{YY}\,\Delta\rho(p)\,, \tag{8.16}$$

where,

$$W(\vartheta,\varphi) = \tfrac{1}{2}P_2(\cos\vartheta) + \tfrac{3}{4}\sin^2\vartheta\cos 2\varphi\,. \tag{8.17}$$

In order to investigate the $W(\vartheta,\varphi)$ term and estimate its influence on the data, $W(\vartheta,\varphi)$ was averaged over the ϑ and φ that were covered by our acceptance. For that, the experimental spectator momentum distribution was built with the $W(\vartheta,\varphi)$ weight and then normalised by the number of total events. Such an average is shown in Fig. 8.3 for unpolarised and polarised modes (modes 1 and 7 of Table 5.1), separately.

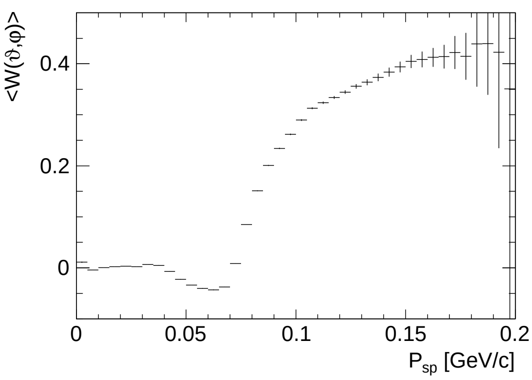

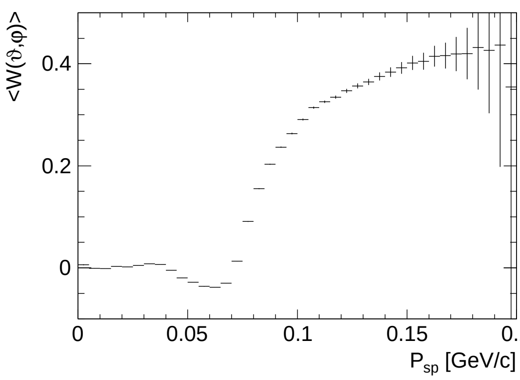

Figure 8.3: Averaged $W(\vartheta,\varphi)$ of Eq. (8.17) within FD acceptance. Left and right panels correspond to polarised modes 1 and 7 of Table 5.1, respectively.

Although the rates could in principle depend on the tensor polarisation of the deuteron beam, no such dependence was found up to proton spectator momenta of 40 MeV/c. Count rates corresponding to this range were used to determine relative luminosities. The new results are mainly in good agreement with the old ones (determined using the $dp \to p_{\rm sp} d\pi^0$ reaction) except for a few modes (Table 8.1).

During the 2005 beam time the BCT signal was reliable and this gave us the possibility of comparing the two calibration methods. Although, the new method is in good agreement with others, it benefits from the enormous statistics and, furthermore, provides information directly about the luminosity.

Pol. mode	BCT	$np \to d\pi^0$	$dp \to p_{\rm sp}X$
1	1.000 ± 0.000	1.000 ± 0.000	1.0000 ± 0.0000
2	0.511 ± 0.006	0.650 ± 0.132	0.5116 ± 0.0003
3	0.471 ± 0.005	0.454 ± 0.109	0.4735 ± 0.0003
4	0.485 ± 0.005	0.312 ± 0.116	0.4832 ± 0.0003
5	0.438 ± 0.005	0.340 ± 0.112	0.4379 ± 0.0003
6	0.394 ± 0.004	0.608 ± 0.107	0.3895 ± 0.0002
7	0.438 ± 0.005	0.578 ± 0.105	0.4358 ± 0.0003
8	0.427 ± 0.005	0.410 ± 0.117	0.4270 ± 0.0003

Table 8.1: The normalisation coefficients obtained using different calibration methods for the 2005 beam time data at $T_d = 1.6$ GeV for eight different polarisation modes.

8.3 Deuteron beam polarimetry

In the earlier work at 1.17 GeV [31], a variety of nuclear reactions with known analysing powers were measured and these were used to establish values for the polarisations. These showed that the analysing powers for the $\vec{d}p \to \{pp\}_s n$ reaction were well reproduced in the impulse approximation calculations [38]. Since the deuteron charge-exchange reaction can be so well identified and measured at ANKE, we use this reaction itself to measure the beam tensor polarisation at the neighbouring energy of 1.2 GeV, the necessary analysing powers being taken from the impulse approximation estimates.

Apart from the large counting rates, this approach has the advantage of being insensitive to the deuteron vector polarisation for small E_{pp} [5] and this was checked in earlier experiment [31]. By comparing the predictions of the current and SP96 SAID solutions [1], differences of less than 4% are found in the extracted values of P_{YY} at 600 MeV. This is consistent with the typical 5% uncertainty quoted in Ref. [31].

The numbers $N(q,\varphi)$ of diprotons produced in the $\vec{d}p \to \{pp\}_s n$ reaction at momentum transfer q and azimuthal angle φ with respect to the X-direction are given in terms of the beam polarisation by

$$\begin{aligned} \frac{N(q,\varphi)}{N_0(q)} = C_n \{1 + \tfrac{1}{4} P_{YY} [A_{xx}(q)(1 - \cos 2\varphi) + \\ A_{yy}(q)(1 + \cos 2\varphi)]\}, \end{aligned} \tag{8.18}$$

where $N_0(q)$ are the numbers for an unpolarised beam and C_n is the relative luminosity of the polarised beam, determined using the $dp \to p_{\rm sp}X$ reaction events.

The break-up data were divided into several bins of momentum transfer q and distributions in $\cos 2\varphi$ were constructed for each bin and polarisation mode. The ratios to the unpolarised state were fitted using Eq. (8.18), the theoretical predictions for A_{xx} and A_{yy} being taken at mean values of q in each bin. The validity of this approach was checked at $T_d = 1.17$ GeV in the earlier experimental studies at ANKE [40]. The beam polarisation in each state was taken as the weighted average over the different values of the momentum transfer. Tables 8.2 and 8.3 list the polarimetry results for the 2005 and 2006 data, respectively.

As already mentioned, the vector analysing power of the $\vec{d}p \to \{pp\}_s n$ reaction is predicted to vanish in the $^1S_0$ limit [5]. As a consequence, the vector polarisation of the beam is unimportant for the tensor analysing power studies carried out with the cluster target. This is no longer the case for the spin-correlation measurements with the polarised cell target. The P_Y vector polarisation of the beam was evaluated from the quasi–free $np \to d\pi^0$ events, also used for luminosity measurement. The procedure is very similar to that of the target polarimetry, which is described in the following section.

The maximum values of P_{YY} were $\approx 85\%$ of the ideal for the 2005 data. But, in the 2006 data, the maximum tensor polarisation dropped to $\approx 55\%$ of the ideal, with little change in the vector polarisation. To ensure an understanding of these two results, a simulation of the whole system of the COSY deuterium ion source was done. For this the efficiencies were simulated for each radio frequency transition unit and also for each of the quadrupole magnets. As a result we could obtain high values for the tensor polarisation with reasonable efficiencies for the separate elements of

Polarisation mode	Ideal values P_Y	Ideal values P_{YY}	P_Y $(np \to d\pi^0)$	P_{YY} $(dp \to \{pp\}n)$
1	0	0	–	–
2	$+\frac{1}{3}$	$+1$	0.26 ± 0.06	0.82 ± 0.03
3	$-\frac{2}{3}$	0	-0.52 ± 0.05	0.15 ± 0.04
4	$+\frac{1}{3}$	-1	0.14 ± 0.06	-0.73 ± 0.04
5	0	$+1$	-0.05 ± 0.05	0.85 ± 0.03
6	0	-2	0.08 ± 0.06	-0.78 ± 0.04
7	-1	0	-0.51 ± 0.05	0.01 ± 0.03
8	$+1$	$+1$	0.35 ± 0.06	0.84 ± 0.03

Table 8.2: Ideal and measured values of the beam polarisation during the 2005 beam time. Measurements were done at $T_d = 1.2$ GeV.

the polarised source, as well as for the whole system. Furthermore, this also provided the explanation of a strange behaviour of the polarisation state 7 in the 2005 data (Table 8.2). It seems that the rf transition unit responsible for the exchanging of deuteron hypefine states $|2\rangle \leftrightarrow |4\rangle$ failed during the experiment, leading to the zero tensor polarisation of the beam. However, the vector polarisation was not affected by this problem.

8.4 Hydrogen target polarimetry

In single-polarised experiments with the cluster-jet target, the $\vec{d}p \to \{pp\}_s n$ reaction is only sensitive to the tensor polarisation of the beam and the values of this could be established by using the $\vec{d}p \to \{pp\}_s n$ reaction itself at the 1.2 GeV calibration energy. In contrast, in order to determine the spin-correlation parameters $C_{x,x}$ and $C_{y,y}$, one has first to determine the vector polarisation of the deuteron beam as well as the polarisation of the hydrogen in the target cell. The basis of both measurements is the quasi-free $\vec{n}p \to d\pi^0$ reaction which, at small spectator momenta, is insensitive to the deuteron tensor polarisation.

However, the main complication connected with the quasi-free $np \to d\pi^0$ reac-

Polarisation mode	Ideal values P_Y	P_{YY}	P_Y $(np \to d\pi^0)$	P_{YY} $(dp \to \{pp\}n)$
1	0	0	–	–
2	$-\frac{2}{3}$	0	-0.272 ± 0.102	-0.002 ± 0.022
3	$+\frac{1}{3}$	-1	0.374 ± 0.116	-0.559 ± 0.023
4	$-\frac{1}{3}$	$+1$	-0.196 ± 0.104	0.464 ± 0.020
5	0	$+1$	0.179 ± 0.118	0.604 ± 0.020
6	-1	$+1$	-0.445 ± 0.101	0.496 ± 0.020
7	$+1$	$+1$	0.678 ± 0.128	0.394 ± 0.021
8	0	-2	-0.088 ± 0.109	-0.231 ± 0.023

Table 8.3: Polarimetry results for the 2006 beam time, analogous to those in Table 8.2.

tion arises due to Fermi motion of the nucleons in the deuteron, which results in the spread of kinetic energy of the incident neutron. As was mentioned in section 7.2, only events with proton spectators momenta below 60 MeV/c were used in the luminosity analyses. As was demonstrated by a Monte Carlo simulation (see Fig. 7.1), such a momentum region is well described by a spectator model. However, when the deuteron beam is polarised and the polarisation is intended to be measured by a quasi-free $np \to d\pi^0$ reaction, the following should be taken into account: if one integrates over all Fermi momenta inside the deuteron, the nucleon polarisation in the deuteron P_Y^n would be reduced from that of the deuteron P_Y^d by a factor

$$P_Y^n = \left(1 - \tfrac{3}{2}P_D\right) P_Y^d \,, \tag{8.19}$$

where P_D is the deuteron D-state probability. However, since the D-state effects vanish like $|p_{\rm sp}|^2$, the dilution of the polarisation signal by the deuteron D-state is negligible if only data with $p_{\rm sp} < 60$ MeV/c are used in the subsequent analyses. Such a cut preserves a large part of the statistics. Although, for the hydrogen target polarimetry such an effect is no longer relevant, the same momentum cut was retained in the analysis.

For an unpolarised deuteron beam incident on a polarised hydrogen target with spin-up ($\uparrow$) and spin-down ($\downarrow$), the asymmetry ratio ϵ between polarised $N^{\uparrow(\downarrow)}$ and unpolarised N^0 yields has the form:

$$\epsilon^{\uparrow(\downarrow)}(\vartheta,\varphi) = \frac{N^{\uparrow(\downarrow)}(\vartheta,\varphi)}{N^0(\vartheta)} = 1 + Q^{\uparrow(\downarrow)} A_y(\vartheta)\cos\varphi, \tag{8.20}$$

where ϑ and φ angles are polar and azimuthal angles, respectively, of the detected particle and Q is the target polarisation. The polar ϑ and azimuthal φ angles of the deuteron were determined according to the procedure described in section 7.2.

The cell introduces additional complications in the determination of the angles because of the spread of the interaction points along the cell axis. Since the $A_y(\vartheta)$ analysing power in the $np \to d\pi^0$ reaction changes very rapidly with angle, the reconstruction of the longitudinal vertex coordinate Z is therefore required for each event to correctly determine the scattering angle. For a two-track event, this can be done with the use of the arrival-time difference for two particles, measured in the scintillation hodoscope. In our kinematical conditions, where the deuteron is at least twice as slow as the proton, such a difference is a sensitive function of Z. The three-momenta of the two particles and the Y and Z coordinates of the vertex are found through an overall fit procedure that uses the information from both the wire chambers and the hodoscope.

Figure 8.4 shows the distribution of interaction points in the Y-Z plane. In addition to helping in the angular determination, the vertex reconstruction allows one to make cuts along the cell axis to minimise the background from the rest gas that is spread throughout the target chamber.

A second major complication arises from the scattering of the beam halo particles on the cell walls. This can produce additional background that would dilute the analysing power signal. As mentioned earlier, the dedicated beam development enabled the bulk of the beam to pass through the cell without hitting the walls. For this reason, additional runs were therefore recorded with unpolarised nitrogen gas target to simulate the shape of the background (see details in Refs. [56, 57]). The background subtraction was performed for each polarisation state by using the missing-mass distributions for the hydrogen and nitrogen data. One such example is shown in Fig. 8.5.

The target polarisation was measured using data taken with an unpolarised deuteron beam at $T_d = 1.2$ GeV. After vertex reconstruction, the $np \to d\pi^0$ data were binned in deuteron cm angles. The background subtraction was performed separately for each bin and distributions in $\cos\varphi$ built for both spin-up and spin-

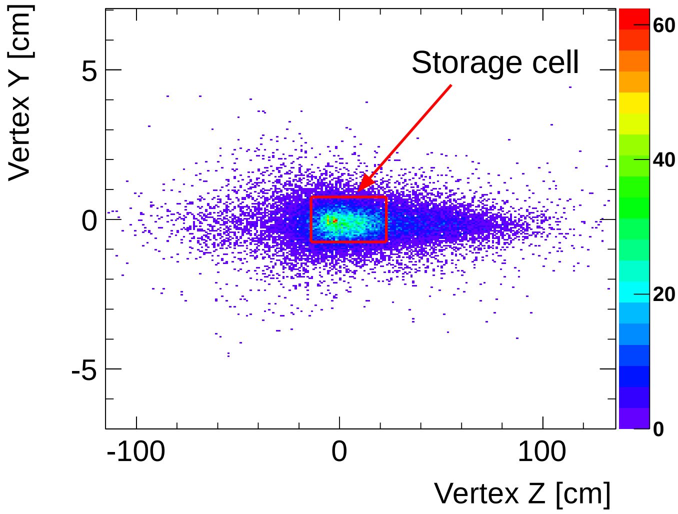

Figure 8.4: Vertex reconstruction in the YZ plane using correlated deuteron-proton pairs. The rectangle shows the physical dimensions of the cell ($Y \times Z = 15 \times 370$ mm^2).

down modes. Although the spin-$\uparrow$ and spin-$\downarrow$ hydrogen states should be produced with the same efficiencies in the ABS, there still remain some possibilities that allow slight differences in polarisation between the two modes. In order to check the polarisations of each mode independently, the unpolarised target data taken at the end of the 2009 beam time especially for this purpose were used. Comparing the asymmetries evaluated with respect to the unpolarised target data using Eq. (8.20), a 15% polarisation difference was found between the spin-$\uparrow$ and spin-$\downarrow$ modes. The final result was recalculated, using the weighted sum of the two data sets from different target polarisations as the unpolarised mode, in the following way:

$$\frac{N^{\uparrow}(\vartheta,\varphi) - N^{\downarrow}(\vartheta,\varphi)}{\alpha N^{\uparrow}(\vartheta,\varphi) + N^{\downarrow}(\vartheta,\varphi)} = Q^{\uparrow} A_y(\vartheta)\cos\varphi, \tag{8.21}$$

where

$$\alpha = \frac{|Q^{\downarrow}|}{|Q^{\uparrow}|} \approx 1.15\,, \tag{8.22}$$

as found from the comparison of the two asymmetries.

According to Eq. (8.21), the ratios of the difference to the sum of the data for the two polarised modes were than fitted with a linear function in $\cos\varphi$ and the value of the product QA_y deduced, which is shown in Fig. 8.6.

Isospin invariance requires the analysing powers in the $np \to d\pi^0$ and $pp \to d\pi^+$

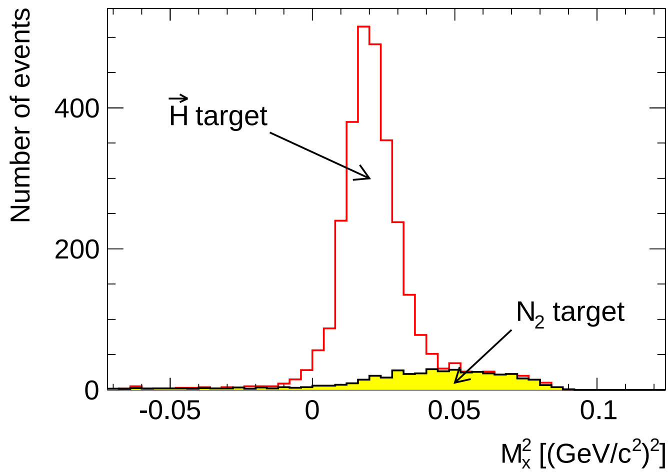

Figure 8.5: Comparison of the $(d, dp_{\rm sp})$ missing-mass-squared distributions at $T_d =$ 1.2 GeV when using a polarised hydrogen target or filling the cell with nitrogen gas.

reactions to be identical and there are numerous measurements of the proton analysing power $A_y(\vartheta)$ of the latter in the 600 MeV region [66]. The dispersion of the results introduces a $\approx 2.3\%$ uncertainty in the value of the polarisation and, since the relevant angular domains are different for the beam and target determinations, these are largely independent for P and Q.

As already mentioned in section 7.2, due to the Fermi motion, the kinetic energy spread of the incident neutron in the laboratory system is rather wide, having almost a 150 MeV width (Fig. 7.1). The analysing power from the SAID $pp \to d\pi^+$ database [66] has a significant energy dependence that is different at small and large cm angles. In order to take this into account, the analysing power was evaluated from the SAID database at different energies, with a 25 MeV step. This two-dimensional function $A_y(\vartheta, T)$ was then averaged over the energy and polar angle, using the experimental neutron kinetic energy (of Fig. 7.1) and pion ϑ^{π}_{cm} angle distributions as weights.

Taking the mean analysing power $\langle A_y \rangle$ in each ϑ^{cm}_d bin, the target polarisation was deduced from the measured QA_y product. This gave $Q^{\uparrow} = 0.61 \pm 0.02$ and $Q^{\downarrow} = -0.70 \pm 0.03$.

Using the quasi-free $np \to d\pi^0$ reaction, the vector polarisation of the deuteron beam (state 3 in Table 5.1) was determined in an analogous way. The weighted

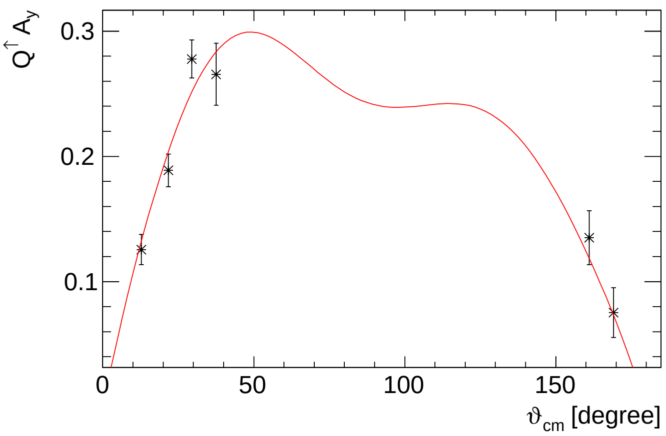

Figure 8.6: The product of QA_y, as evaluated from the experimental data. The curve corresponds to A_y from the SAID $pp \to d\pi^+$ database, further averaged over the energy (see the text) and scaled by the target polarisation of 0.61.

sums of target spin-$\uparrow$ and spin-$\downarrow$ modes were constructed, as follows:

$$\frac{\alpha N_3^{\uparrow}(\vartheta,\varphi) + N_3^{\downarrow}(\vartheta,\varphi)}{\alpha N_1^{\uparrow}(\vartheta,\varphi) + N_1^{\downarrow}(\vartheta,\varphi)} = 1 + P_Y A_y(\vartheta)\cos\varphi, \tag{8.23}$$

where indices 1 and 3 correspond to beam polarised states in Table 5.1. Using similar techniques as for the target polarimetry, the beam polarisation was determined to be $P_Y = -0.51 \pm 0.05$.

Chapter 9

Spin observables in the $dp \to \{pp\}_s n$ reaction

The primary aim of this work was to investigate the tensor analysing powers and spin-correlation coefficients of the $dp \to \{pp\}_s n$ reaction at different deuteron beam energies. Since these observables are directly linked to np charge exchange amplitudes within the impulse approximation, comparison of the experimental data with their theoretical estimates will indicate how precise the current np database is and make an useful contribution in further improving it. This chapter describes the procedure of evaluating different spin observables from the single and double-polarised experimental data. The results obtained and their interpretation are also presented.

In experiments with the unpolarised cluster-jet target, the $\vec{d}p \to \{pp\}_s n$ reaction is only sensitive to the tensor polarisation of the beam and the values of this could be established by using the $\vec{d}p \to \{pp\}_s n$ reaction itself at the 1.2 GeV calibration energy, as described in section 8.3. In contrast, in order to determine the spin-correlation parameters $C_{x,x}$ and $C_{y,y}$, one has first to determine the vector polarisation of the deuteron beam as well as the polarisation of the hydrogen in the target cell. This was done on the basis of the quasi-free $\vec{n}p \to d\pi^0$ reaction which, at small spectator momenta, is insensitive to the deuteron tensor polarisation. All the details on beam and target polarimetry are to be found in section 8.4.

9.1 Tensor analysing powers

The successful polarimetry of the deuteron beam, described in the previous chapter, allowed us to determine the tensor analysing powers of the $\vec{d}p \to \{pp\}_s n$ reaction. In order to ensure the reliability of the whole analysis procedure and consistency with impulse approximation predictions, this was first performed at 1.2 GeV. Although a single-polarised beam mode together with the unpolarised one is already sufficient to measure the analysing powers, as already mentioned, several configurations of the polarised deuteron beam were employed in the experiments, and these are listed in Table 5.1. This allowed us to measure A_{xx} and A_{yy} for each mode separately to check the systematics. Measuring these observables at the same energy where P_{YY} was determined, would help to locate any inconsistency either in the analyses or in the experimental data themselves. Furthermore, this would check the reproducibility of the results obtained at 1.17 GeV in an earlier experiment [31].

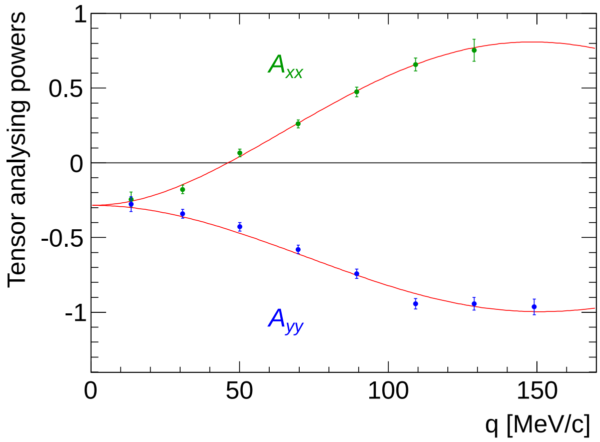

Figure 9.1: The tensor analysing powers of the $dp \to \{pp\}_s n$ reaction, measured at $T_d = 1.2$ GeV. Low E_{pp} data (< 3 MeV) was used. Curves correspond to the impulse approximation predictions based upon the current SAID $np \to np$ amplitudes [1].

The deuteron Cartesian tensor analysing powers A_{xx} and A_{yy} were extracted using Eq. (8.18) in much the same way as for the polarimetry, with the beam tensor polarisation P_{YY} being determined at $T_d = 1.2$ GeV. The ratios of the polarised to unpolarised corrected count rates were fitted in terms of the two free parameters A_{xx} and A_{yy}. The procedure was repeated for different polarisation states and the results averaged over these beam modes. The results obtained with the $E_{pp} < 3$ MeV data are shown in Fig. 9.1 together with theoretical predictions.

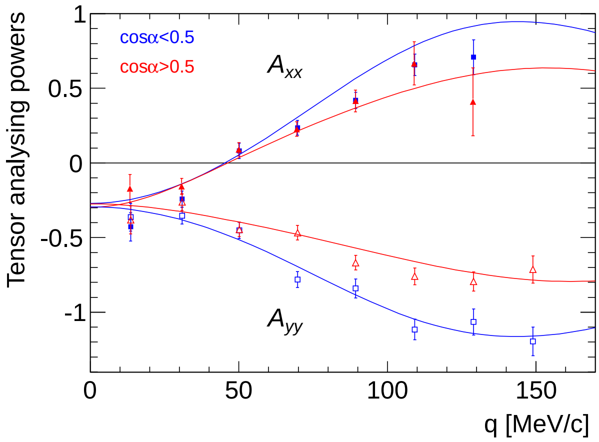

Figure 9.2: Tensor analysing powers at $T_d = 1.2$ GeV using $1 < E_{pp} < 3$ MeV data. Curves correspond to the impulse approximation predictions based upon the current SAID $np \to np$ amplitudes [1]. By choosing the angular domain of either $\cos\alpha < 0.5$, or $\cos\alpha > 0.5$ between the momentum transfer and the pp system relative momenta in the Breit frame, contributions from S and P waves are separated.

The contamination from the P-wave dilutes tensor analysing power signal. At very small E_{pp}, the diproton is mainly in $^1S_0$ state and then the contribution from the P state is negligible. This results in a maximal tensor analysing power signal. In contrast, when the relative momentum of the diproton increases, contributions from the P-wave become significant, diluting the A_{xx} and A_{yy}. In order to observe this effect on the experimental data, a larger E_{pp} cut has to be introduced. But the ANKE forward detector acceptance drops rapidly with E_{pp}, resulting in very poor statistics above 5 MeV. Another possibility is to introduce the cut on the angle between the momentum transfer and the pp system relative momenta in the Breit frame, which distinguishes the S and P waves. The corresponding results must differ for different angles. Analyses were done for $\cos\alpha < 0.5$ and $\cos\alpha > 0.5$ separately to look for the effect. The tensor analysing power dilution was clearly identified, as can be seen in Fig. 9.2.

The results for the tensor analysing powers at higher energies are shown in Fig. 9.3 at three beam energies as functions of the momentum transfer. The agreement between the experimental data and the impulse approximation predictions is very good at $T_n = 800$ and 900 MeV. At these energies the SAID np amplitudes [1] used as input in the calculations are considered to be reliable but at $T_n = 1.135$ GeV, which corresponds to the maximum deuteron energy available at COSY, the agreement is much worse. Since there are also severe discrepancies in the unpolarised cross

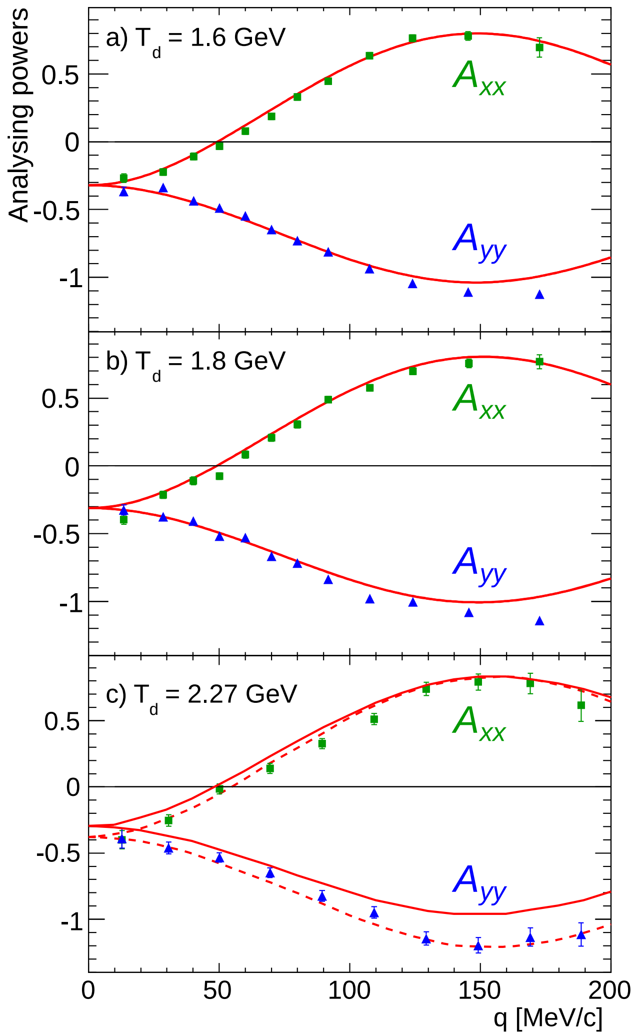

Figure 9.3: Tensor analysing powers A_{xx} (squares) and A_{yy} (triangles) of the $\vec{d}p \to \{pp\}_s n$ reaction at three beam energies for low diproton excitation energy, $E_{pp} < 3$ MeV (numerical values are listed in Table B.1), compared to impulse approximation predictions based upon the current SAID $np \to np$ amplitudes [1]. The dashed curves at 2.27 GeV correspond to a uniform reduction of the spin-longitudinal $\varepsilon(q)$ amplitude by 25%. The error bars include the uncertainties from the relative luminosity C_n and the beam polarisations determined at 1.2 GeV. In addition, at the higher energies there is an overall uncertainty of up to 4% due to the use of the polarisation export procedure.

section at this energy, it is natural to question whether there might be deficiencies in the SAID np analysis at this energy.

The experimental value of $A_{xx} = A_{yy}$ in the forward direction ($q \approx 0$) is significantly more negative than the predictions using the SAID np amplitudes at

1.135 GeV. However, it can be seen from Eq. (3.11) that a relative reduction in the ε amplitude might improve the predictions.

The problem with the SAID implementation of the ε amplitude at 1.135 GeV can be identified more explicitly also in a different way. The ratio of Eq. (3.13) of the transition form factors from deuteron to diproton, involving deuteron S and D states, is close to unity in the forward direction (small momentum transfers). This then suggests the following dependences, using Eq. (3.11):

$$
\begin{aligned}
(1-A_{yy})/(1+A_{xx}+A_{yy}) &\approx (|\beta|^2+|\gamma|^2)/|\varepsilon|^2\,, \\
(1-A_{xx})/(1+A_{xx}+A_{yy}) &\approx |\delta|^2/|\varepsilon|^2\,, \\
(1-A_{xx})/(1-A_{yy}) &\approx |\delta|^2/(|\beta|^2+|\gamma|^2)\,.
\end{aligned}
$$

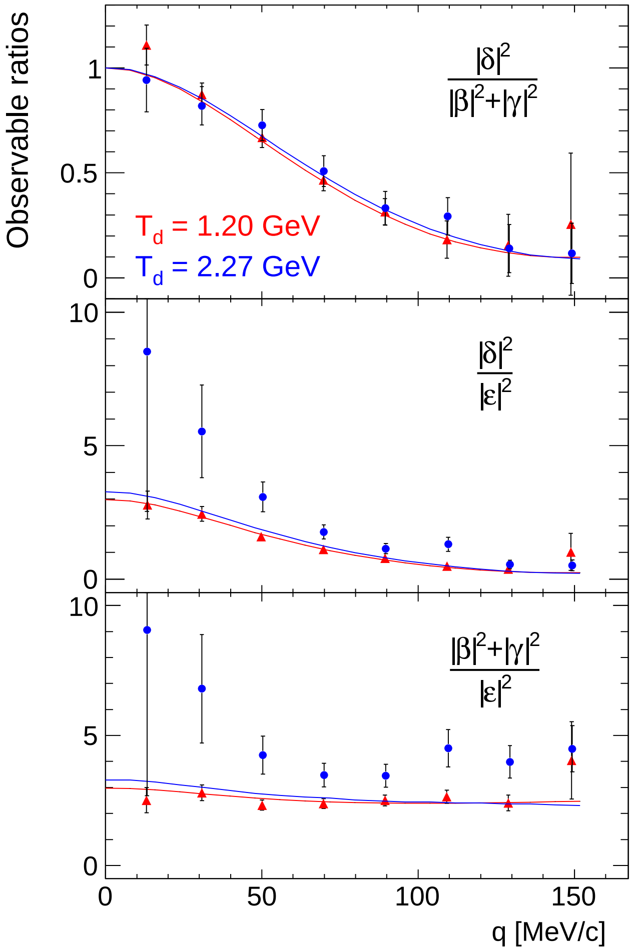

Figure 9.4: Measured ratios of observables as functions of momentum transfer for two different beam energies. Solid lines correspond to impulse approximation predictions.

The variation of these quantities with q are presented in Fig. 9.4 for the 1.2 and 2.27 GeV data. Whereas at the lower energy all the ratios are well described by the model, at the higher it is seen that it is only $|\delta|^2/(|\beta|^2 + |\gamma|^2)$ which is well understood. It seems that the SAID program currently overestimates the values of $|\varepsilon|$ at small q. To check this possibility, the predictions were recomputed with the $\varepsilon(q)$ amplitude being reduced uniformly by 25%. Fortunately, this gave the much better overall agreement with the data that is demonstrated by the dashed curves in the lower panel of Fig. 9.3. This therefore suggests that the current SAID amplitudes [1] might overestimate the relative strength of the $\varepsilon(q)$ at small q but further proof is required and this is furnished by the measurements of the spin correlations, described in the next section.

9.2 Spin-correlation parameters

The single-polarised experiments of 2005 and 2006 allowed us to obtain useful data on tensor polarisations of the $\vec{d}p \to \{pp\}_s n$ reaction. However, in order to completely exploit the potential of this reaction in np amplitude studies, as a logical continuation, a double-polarised experiment was also carried out in 2009 (see section 5.2). Its primary aim was to study the spin-correlation parameters $C_{x,x}$ and $C_{y,y}$ of the same reaction to determine the relative phases of the spin-spin amplitudes [60]. Furthermore, the double-polarised data at $T_d = 2.27$ GeV gave an excellent opportunity to check whether the suspected ε deficiencies in the SAID amplitudes at highest beam energy were reflected also in the spin correlations.

In the $\vec{d}\vec{p} \to \{pp\}_s n$ events the background subtraction was carried out in the same way as for the $dp \to p_{\rm sp} d\pi^0$ reaction, with the nitrogen gas data simulating the shape of the background, as illustrated in Fig. 9.5. Similar to the tensor analysing powers, the spin-correlation parameters are also functions of the momentum transfer q. Hence, in the analysis the data were binned in intervals in q and the background subtraction procedure was performed for each q bin separately.

In order to simplify as much as possible the evaluation of the spin-correlation parameters from the $\vec{d}\vec{p} \to \{pp\}_s n$ reaction, no tensor polarised deuteron beam modes were used (see Table 5.1). In this case the ratio of the polarised $N(q,\varphi)$ to unpolarised $N_0(q)$ yields of Eq. (8.1) reduces to:

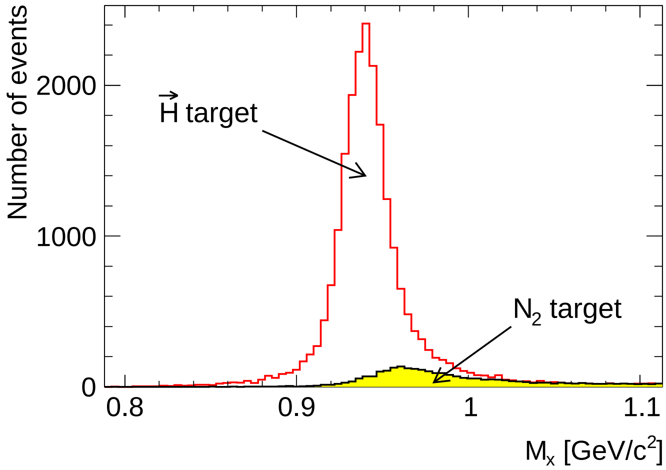

Figure 9.5: Comparison of the (d, pp) missing-mass distributions at $T_d = 1.2$ GeV beam energy when using a polarised hydrogen target or filling the cell with nitrogen gas.

$$\frac{N(q,\varphi)}{N_0(q)} = 1 + QA_y^p(q)\cos\varphi + \tfrac{3}{2}P_Y A_y^d(q)\cos\varphi + \tfrac{3}{4}P_Y Q[(1+\cos 2\varphi)C_{y,y}(q) + (1-\cos 2\varphi)C_{x,x}(q)]. \tag{9.1}$$

As already mentioned in section 5.2, the polarisation of the hydrogen target was flipped between spin ↑ and spin ↓ every five seconds throughout the whole COSY cycle. Since the target density provided by the ABS (section 4.3) is precisely the same in the two states, the achieved luminosities of Eq. (8.7) depend solely on the beam intensity. The intensity of the COSY beam largely depends on the injection and the procedure of further accelerating the beam (*cooling, stacking, etc.*), and can vary significantly from cycle to cycle. But it changes very slowly within a cycle. Therefore, within the five seconds the intensity of the beam remains practically unchanged and the resulting average beam intensities in the two target states are practically the same. Choosing such a small flipping time for the ABS polarisation states allowed us to completely eliminate the need for the count normalisation on the relative luminosities and to evaluate asymmetries directly between the two polarised states of the target.

Although the experiment was designed for the study of spin correlations, analysing the combination of polarised target and unpolarised deuteron beam gave a possi-

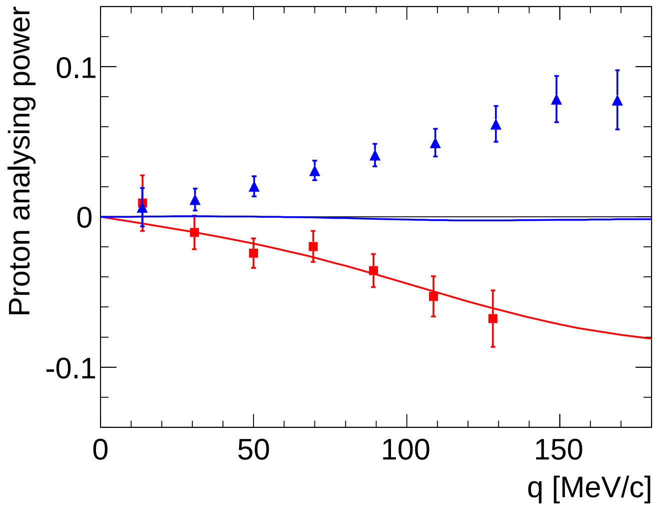

Figure 9.6: Proton analysing powers A_y^p for the $dp \to \{pp\}_s n$ reaction at $T_d = 1.2$ (red squares) and 2.27 GeV (blue triangles) for $E_{pp} < 3$ MeV (numerical values are listed in Table B.3). The error bars do not include the 5% uncertainties arising from the target polarisation. Curves correspond to the theoretical predictions. Note that at 2.27 GeV the A_y^p prediction is very small and hardly visible on this scale.

bility to obtain the dependence of the target analysing power A_y^p on q. Using the asymmetry between the two target modes, the A_y^p was obtained from the fit of the $\cos\varphi$ dependence in

$$\frac{N^{\uparrow}(q,\varphi) - N^{\downarrow}(q,\varphi)}{\alpha N^{\uparrow}(q,\varphi) + N^{\downarrow}(q,\varphi)} = QA_y^p(q)\cos\varphi. \tag{9.2}$$

Results are presented in Fig. 9.6 at 1.2 and 2.27 GeV. Despite the smallness of the signal, the measured values of A_y^p at 1.2 GeV are in a perfect agreement with impulse approximation predictions. In contrast, at 2.27 GeV the corresponding predictions are so small that they can hardly be distinguished from the x-axis on this scale. Equation (3.11) then suggests that there must be a serious problem also with the SAID determination of the spin-orbit amplitude $\gamma(q)$ at 1.135 GeV.

In impulse approximation A_y^d vanishes [5], which is consistent with earlier ANKE measurements at 1.17 GeV [31], and this simplifies the determination of $C_{x,x}$ and $C_{y,y}$ using data with polarised beam and polarised target.

$$\frac{N^{\uparrow}(q,\varphi) - N^{\downarrow}(q,\varphi)}{\alpha N^{\uparrow}(q,\varphi) + N^{\downarrow}(q,\varphi)} = \tfrac{3}{4}P_Y Q[(1+\cos 2\varphi)C_{y,y}(q) + (1-\cos 2\varphi)C_{x,x}(q)]. \tag{9.3}$$

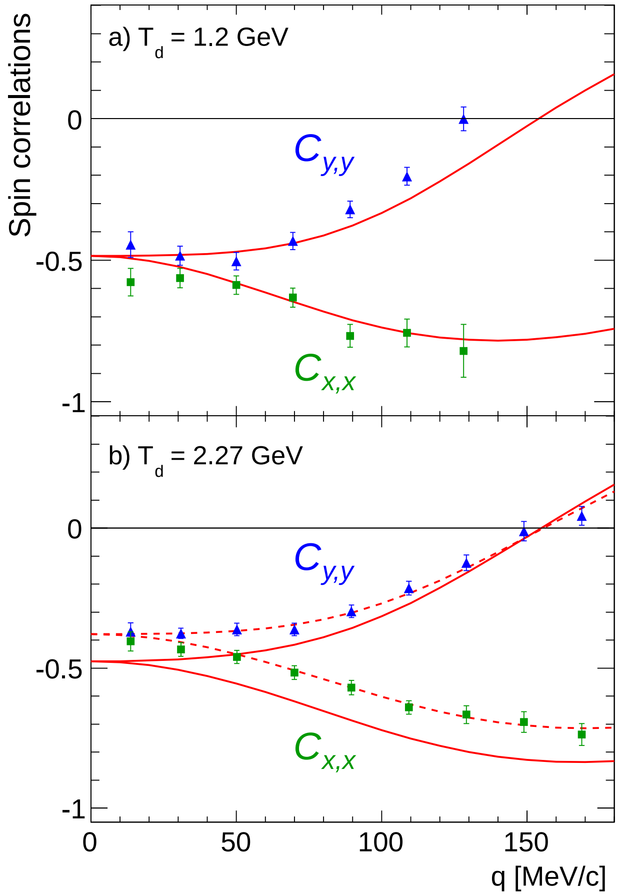

Figure 9.7: The spin-correlation coefficients $C_{x,x}$ and $C_{y,y}$ for the $dp \to \{pp\}_s n$ reaction at $T_d = 1.2$ and 2.27 GeV for $E_{pp} < 3$ MeV (numerical values are listed in Table B.4). The error bars do not include the 11% uncertainties in the combined beam and target polarisations. The curves are impulse approximation predictions; dashed curves at 2.27 GeV correspond to $|\varepsilon(q)|$ being reduced by 25%.

After binning the normalised counts in intervals in q, the $\cos 2\varphi$ dependence in Eq. (9.3) allowed us to extract the $C_{x,x}$ and $C_{y,y}$ coefficients separately. Note, that the resolutions in both E_{pp} and q in the cell-target data are similar to those achieved with the cluster target.

The spin-correlation data for an $E_{pp} < 3$ MeV cut are compared with theoretical predictions in Fig. 9.7. The good agreement with the experimental points at $T_d =$ 1.2 GeV shows that the two relative phases between the spin-spin amplitudes are well predicted by the SAID program at this energy. It can, however, not come as a complete surprise to find that there are serious discrepancies at $T_d = 2.27$ GeV but, as shown by the dashed line, these largely disappear if the SAID $\varepsilon(q)$ amplitude is scaled uniformly by a factor of 0.75, *i.e.*, by the same factor that brought agreement for the A_{xx} and A_{yy} observables!

Chapter 10

Measurements with pion production

The experiments reviewed in this work have provided useful data, not only on the reactions of primary importance, but also on variety of other processes that satisfied the same triggering conditions of the experiment. Some of these side processes, called by-products, are described in this chapter.

One of the most important by-product was the deuteron-proton charge-exchange channel with pion production in the $\vec{d}p \to \{pp\}_s\Delta^0$ reaction, which could be isolated on the basis of the missing mass. The single-polarised data allowed us to measure this reaction and obtain differential cross sections and tensor analysing powers at $T_d = 1.6$, 1.8 and 2.27 GeV.

Another reaction of importance is the well known quasi-free $np \to d\pi^0$ reaction, which was widely used in our analysis for the luminosity determination and also in the beam and target polarimetry. In addition, we managed to measure the spin-correlation parameters of this reaction using the double-polarised data of 2009.

10.1 The $dp \to \{pp\}_s\Delta^0$ reaction

It was first demonstrated at SATURNE that the $\Delta(1232)$ can be excited in the $\vec{d}p \to \{pp\}_s\Delta^0$ charge-exchange reaction at a deuteron beam energy $T_d = 2.0$ GeV [70, 71, 72]. In analogy to the final neutron case, it is expected that the highly inelastic deuteron charge-exchange measurements correspond to a spin transfer from the initial neutron to final proton in the $\vec{n}p \to \vec{p}\Delta^0$ process with a spectator proton. This would give valuable information on the spin structure in the excitation of the Δ isobar.

The missing-mass spectra of the $dp \to \{pp\}X$ events, presented in Fig. 7.5, clearly show a lot of strength at higher M_X, above the πN threshold. This must be associated with the production of a single pion, meaning that ANKE data provide valuable information also on the Δ channel of the deuteron charge-exchange reaction.

The one-pion-exchange (OPE) model, which contains direct (D) and exchange (E) terms, was successfully used for describing the unpolarised cross section of the $pp \to \Delta^{++}n$ reaction in Ref. [73]. An implementation of the model for the $dp \to \{pp\}_s N\pi$ reaction is shown in Fig. 10.1. It should be noted that in impulse approximation the direct diagram contains the same triangle loop as in the $dp \to \{pp\}_s n$ reaction, *i.e.*, the same $d \to \{pp\}_s$ form factors.

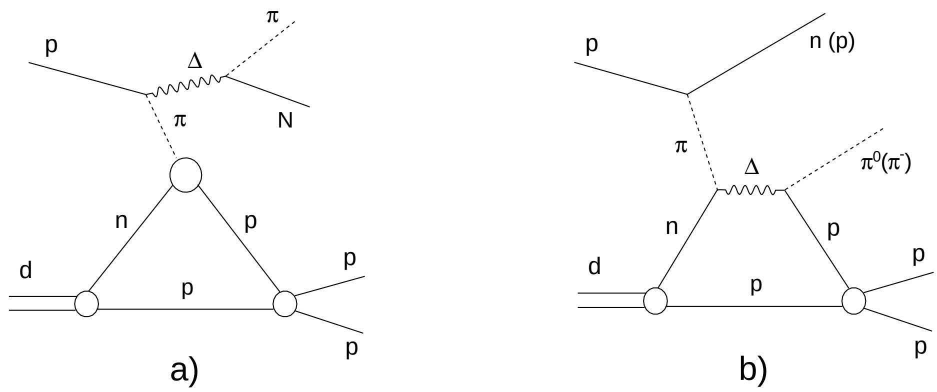

Figure 10.1: The one-pion-exchange contribution to $\Delta(1232)$ production in the deuteron charge-exchange break-up reaction. (a) The direct (D) term. (b) The exchange (E) term.

10.1.1 Differential cross section

The differential cross section determination procedure for the $dp \to \{pp\}_s\Delta^0$ reaction has many similarities to that for the $dp \to \{pp\}_s n$ (see section 7.3). Despite the different mass region, this channel was identified in exactly the same way as for the neutron case, using the time information from the forward hodoscope (see section 4.2). The luminosity, as well as the beam polarisation, was already determined while investigating the $dp \to \{pp\}_s n$ reaction. Although all these further simplified the analyses of the $dp \to \{pp\}_s \Delta^0$ reaction, other problems are important here, associated with the ANKE acceptance corrections in the cross section as well as in the tensor analysing powers.

In order to evaluate the ANKE acceptance for the $dp \to \{pp\}_s \Delta^0$ reaction, Monte Carlo simulations were performed at $T_d = 1.6$, 1.8 and 2.27 GeV. Events were generated according to the simple one-pion-exchange mechanism of Fig. 10.1a. By dividing the numbers of reconstructed events by the total, two-dimensional acceptance maps were obtained in ϑ_{pp} and M_X. The angular acceptance limit of the ANKE FD for diprotons from the $dp \to \{pp\}_s \Delta^0$ reaction changes slightly with energy and M_X, reaching 4.5° in the laboratory system. However, as was observed, the acceptance drops very rapidly above 3°. In order to avoid potentially unsafe regions, a cut of $\vartheta_{pp} < 3°$ was applied at all energies, to both the simulation and the data.

In the cross section analyses of the neutron channel the acceptance was determined as a function of E_{pp}. In contrast, the acceptance is here averaged over this observable. In this case, due to finite resolutions, it becomes very important to consider the event migration, which depends on the cross section behaviour with respect to E_{pp}. The strong S-wave final-state interaction (FSI) between the two measured protons was taken into account according to the Migdal-Watson approach [74, 75], using the pp $^1S_0$ scattering amplitude [76].

Unlike the neutron case, direct production of the Δ isobar necessarily involves relatively high momentum transfers. Hence, the P-wave contribution becomes important. This effect is clearly observed in the comparison between the uncorrected experimental and simulated E_{pp} distributions for all events shown in Fig. 10.2. The Migdal-Watson approach, which considers only the S-wave term (shown as magenta stars), falls well below the data for $E_{pp} > 1$ MeV. Since any FSI will be much weaker in the P-waves, it is reasonable to think that the weight for this contribution is proportional to the square of the pp relative momentum, *i.e.*, the diproton excitation energy. By fitting the coefficients of the two known shapes together, it was found that for all beam energies the P-wave contribution is about 15% of the total event rate for $0 < E_{pp} < 3$ MeV.

The experimental two-dimensional data in ϑ_{pp} and M_X were normalised on the luminosity (Table 7.1), corrected for different factors (discussed in section 7.3), and for the obtained two-dimensional acceptance maps. The resulting $dp \to \{pp\}_s X$

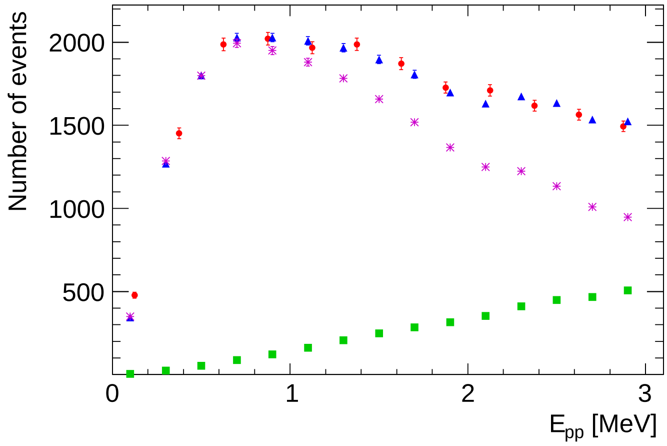

Figure 10.2: Experimental (red dots) and simulated (magenta stars) E_{pp} distributions, summed over all three beam energies. The fitted value of the non-interacting P-wave (green squares) corresponds to a total contribution of 15% over this E_{pp} range. The overall simulation is shown by blue triangles.

missing-mass cross sections are shown in Fig. 10.3 for $E_{pp} < 3$ MeV. In the mass range accessible at COSY, single-pion production is dominated by the formation and decay of the $\Delta(1232)$ isobar. It is therefore reassuring that the spectra at all three beam energies are maximal for $M_X \approx 1.2$ GeV/c^2.

Expressions for the two-dimensional cross section for the direct Δ production (Fig. 10.1a) are given explicitly in Ref. [73]. Details about the resulting one-dimensional cross section, and also the calculation of the exchange (E) mechanism, are to be found in Refs. [77, 78].

As is clearly seen in Fig. 10.3, there is a lot of strength at all energies that is underestimated enormously by the simple direct one-pion-exchange model for the $np \to p\,\Delta^0$ amplitude. The model provides a satisfactory description of the data only at high M_X, though it must be stressed that this calculation neglects the 15% P-state contribution shown in Fig. 10.2. This failure must be more general than the specific implementation of the model because the Δ is a p-wave pion-nucleon resonance. There can therefore be little strength at low M_X and this suggests that one should search for other mechanisms that might dominate near the πN threshold.

We were not the first who encountered this problem. In the pioneering SATURNE experiment [79] one pion exchange was only successful at high M_X. To investigate this further, the authors compared the small-angle hydrogen target data, $p(d,pp)X$, with quasi-free production in deuterium, $d(d,pp)X$. The two data sets

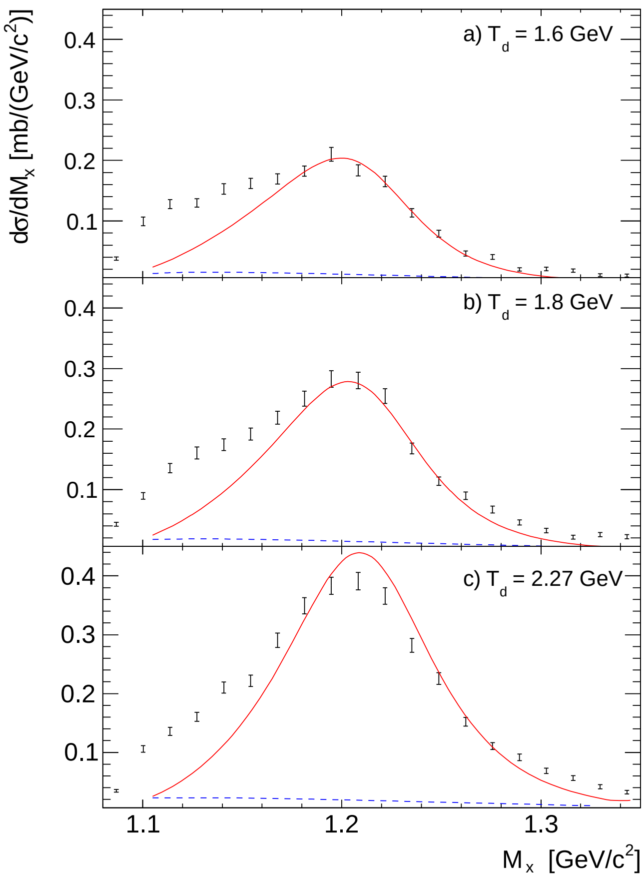

Figure 10.3: Unpolarised differential cross section for the $dp \to \{pp\}X$ reaction with $E_{pp} < 3$ MeV for $M_X > M_N + M_\pi$ at three deuteron beam energies (numerical values are listed in Table B.5). The data are summed over the interval $0 < \vartheta_{\text{lab}} < 3^\circ$ in the diproton laboratory polar angle. Only statistical errors are shown. The solid (red) curves correspond to the one-pion-exchange predictions for the direct mechanism of Fig. 10.1a. The dashed (blue) lines show the contribution of the exchange (E) mechanism of Fig. 10.1b.

explicitly showed different behaviour at low M_X and threfore provided some hints on possible contributions at this mass region.

The direct Δ production mechanism, shown in Fig. 10.1a, involves a vertex with πN initial state. In the case of a hydrogen target, this corresponds to the $\pi^- p$. In addition, by replacing the hydrogen target by deuterium the $nn \to \Delta^- p$ channel is also excited, which involves the $\pi^- n$ initial state. Let us denote the πN states by $|II_3\rangle$, where I is a total isospin and I_3 is its projection. In this case the $\pi^- n$ would correspond to the pure $|3/2\ -3/2\rangle$ state, while the $\pi^- p$ would involve two states with $|3/2\ -1/2\rangle$ and $|1/2\ -1/2\rangle$. The relative rates of these two reactions can be estimated by using the Clebsch-Gordan coefficients:

$$\frac{\sigma_{nn\to p\Delta^-}}{\sigma_{np\to p\Delta^0}} = \frac{3|M_{3/2}|^2}{|M_{3/2}+2M_{1/2}|^2}\,, \tag{10.1}$$

where $M_{3/2}$ and $M_{1/2}$ are amplitudes corresponding to the states with $I = \frac{3}{2}$ and $I = \frac{1}{2}$, respectively. However, at πN CM energies close to the Δ mass the $I = \frac{3}{2}$ state dominates ($|M_{3/2}| \gg |M_{1/2}|$). This leads to the following approximation for the relative rates in hydrogen and deuterium data:

$$\sigma_{D_2}/\sigma_{H_2} \approx 4\,. \tag{10.2}$$

Taking this into account, the authors divided their deuterium data by factor of 4 to compare with that obtained with hydrogen. In order to make this comparison even more informative, we extracted their data at $T_d = 2$ GeV at $\vartheta = 0.5^\circ$ and, using equations (10.1) and (10.2), evaluated cross sections for $I = \frac{3}{2}$ and $\frac{1}{2}$ separately.

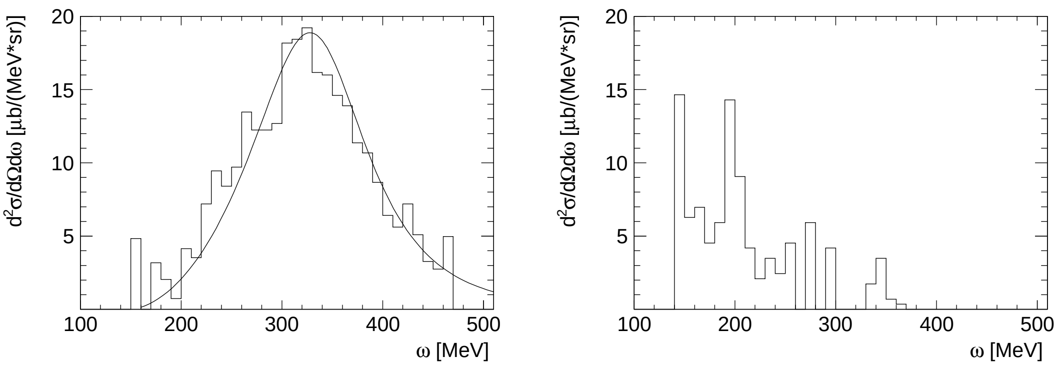

Figure 10.4: SATURNE data at $T_d = 2$ GeV at $\vartheta = 0.5^\circ$, presented with respect of beam energy loss $\omega = E_d - E_{pp}$, which is closely related to M_X. The pure $I = \frac{3}{2}$ cross section (left) is reasonably well described by the direct one-pion-exchange predictions (solid curve). The strength arising from $I = \frac{1}{2}$ πN interaction, deduced by comparing the hydrogen and deuterium data, is shown in the right panel.

The direct mechanism of the one-pion-exchange model seems to describe the $I = \frac{3}{2}$ data very well. Hence, it will be reasonable to conclude that the excess of events at low M_X is mainly to be associated with πN pairs in the $I = \frac{1}{2}$ state rather than the $I = \frac{3}{2}$ of direct Δ production [72].

An attempt has been made to suppose the culprit being the s-wave πN and roughly estimate its contribution to direct production. For this the p-wave one-pion-exchange model predictions were modified as:

$$\left(\frac{d\sigma}{dm}\right)_s \approx \left(\frac{d\sigma}{dm}\right)_p \times \frac{2\sigma(S_{11}) + \sigma(S_{31})}{\sigma(P_{33})} \times \frac{p_0^2}{p^2}, \tag{10.3}$$

where $\sigma(S_{11})$, $\sigma(S_{31})$, and $\sigma(P_{33})$ are the SAID predictions for the πN elastic cross sections in the three partial waves noted, and p_0 and p are the momenta of the final and intermediate pion, respectively. Such an estimate indicates only a very tiny extra strength at low M_X, as seen in Fig. 10.5, and this would have to be increased by several orders of magnitude in order to agree with the experimental data. One must therefore seek an alternative explanation to direct isobar production to describe the data.

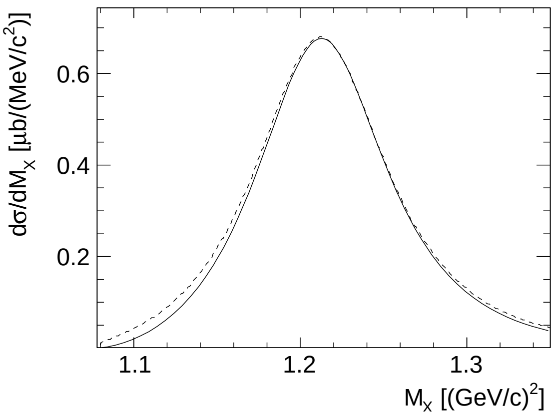

Figure 10.5: Differential cross section predictions for the $dp \to \{pp\}_s\Delta^0$ reaction at $T_d = 2.27$ GeV. Simple estimation of s-wave contribution (dashed) using SAID amplitudes gives little additional effect over the p-wave (solid).

While trying to find a reasonable explanation of this problem at low M_X, we noticed some similarities between the $dp \to \{pp\}X$ reaction and the inclusive $dp \to dX$ [80] or $\alpha p \to \alpha X$ [81] measurements that were dedicated to the search for the excitation of the $N^*(1440)$ Roper resonance. Due to conservation laws, the isospin of the unobserved state X in these cases must be $I = \frac{1}{2}$ but this does not have to be an N^* resonance. These data show the largest strength at very low values of M_X, with only a small enhancement arising from the $N^*(1440)$. The authors explained this with the excitation of the $\Delta(1232)$ isobar inside the projectile deuteron or α-particle [82, 83]. Although the mechanism is driven by the $\Delta(1232)$, the pion and nucleon that make up the state X are produced at different vertices and so X is not required to be in a p-wave and to have isospin $I = \frac{3}{2}$.

The exchange diagram (E) for the $dp \to \{pp\}_s X$ reaction is shown in Fig. 10.1b. The corresponding predictions, presented in Fig. 10.3, demonstrate some strength at low M_X, but the overall magnitude is still far too small to provide an adequate description of the data in this region [77]. The relative reduction compared to the $dp \to dX$ or $\alpha p \to \alpha X$ calculations [82, 83] arises primarily from the spin-flip that is inherent in the $d \to \{pp\}_s$ transition. We therefore turn to the measurement of the tensor analysing powers for more clues.

10.1.2 Tensor analysing powers

As already mentioned, by studying the $dp \to \{pp\}_s n$ spin observables, the first stage of the determination of the tensor analysing powers in the $dp \to \{pp\}_s X$ reaction, including beam polarimetry and count normalisation on relative luminosities, had been accomplished. However the Δ channel analyses required additional measures to be taken, to which we now turn.

The polarised to unpolarised count ratio for $dp \to \{pp\}_s X$ events is expected to be the similar to that for $dp \to \{pp\}_s n$. The main difference here is that the analysing powers might, in principle, be functions of mass as well as of the momentum transfer. The three-momentum transfer can be usefully split into longitudinal $\vec{q}_z$ and transverse parts $\vec{q}_t$, so that in general $\vec{q} = (q_t \cos\varphi, q_t \sin\varphi, q_z)$. The longitudinal component of the momentum transfer may be written in terms of q_t and the missing mass M_X.

Similarly to the $dp \to \{pp\}_s n$ reaction (Eq. 8.18), when only the tensor polarisation is considered, the numbers $N(q_t, M_X, \varphi)$ of diprotons detected as a function of q_t, M_X, and φ are given in terms of the beam polarisation P_{yy} by

$$\frac{N(q_t, M_X, \varphi)}{N_0(q_t, M_X)} = C_n 1 + \tfrac{1}{2} P_{yy} \left[A_{xx}(q_t, M_X) \sin^2\varphi + A_{yy}(q_t, M_X) \cos^2\varphi \right]. \qquad (10.4)$$

Due to limited statistics, it was not possible to measure A_{xx} and A_{yy} as functions of two variables. Data were binned instead in either M_X or in q_t, summing over the full range of the other variable. Since the acceptance A is also a function of two variables, in such a scenario we would measure the weighted averages of A_{xx} and

A_{yy}, with the acceptance being applied as a weight

$$\begin{aligned}\langle A_{xx}(q_t)\rangle &= \frac{\int A(q_t, M_X)A_{xx}(q_t, M_X)dM_X}{\int A_{xx}(q_t, M_X)dM_X},\\ \langle A_{yy}(q_t)\rangle &= \frac{\int A(q_t, M_X)A_{yy}(q_t, M_X)dM_X}{\int A_{yy}(q_t, M_X)dM_X}.\end{aligned}\tag{10.5}$$

In order to minimise such effects in the analysis, the polarised and unpolarised data were weighted with the inverted two-dimensional acceptance that was evaluated for the extraction of the unpolarised cross section.

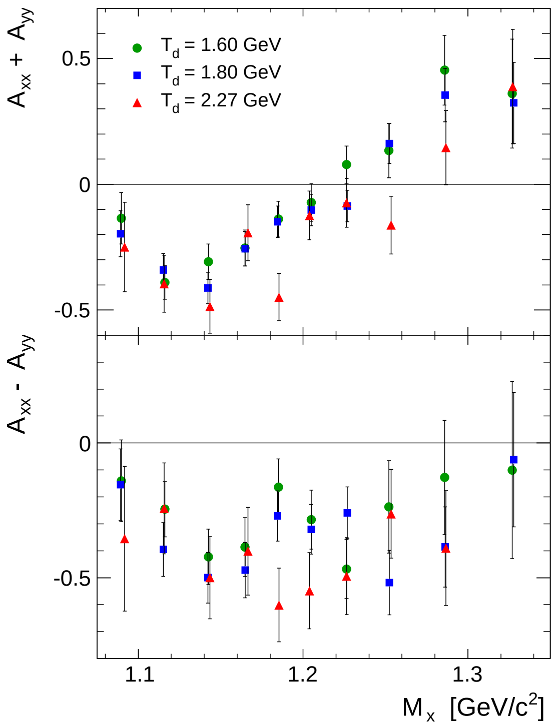

Figure 10.6: The sum and difference of the Cartesian tensor analysing powers for the $\vec{d}p \to \{pp\}_s X$ reaction with $E_{pp} < 3$ MeV at three different beam energies. The data are corrected for the detector acceptance and summed over the range $0° < \vartheta_{\text{lab}} < 3°$ in diproton laboratory polar angle. Though the error bars are dominantly statistical, they include also the uncertainties from the beam polarisation and relative luminosity C_n. In addition, there is an overall uncertainty of up to 4% due to the use of the polarisation export technique (see section 5.3).

After summing the acceptance-corrected data over the momentum transfer, the sum and difference of the deuteron Cartesian tensor analysing powers A_{xx} and A_{yy} were obtained, which are presented as functions of the missing mass M_X in Fig. 10.6.

[These combinations are proportional to the spherical tensor components T_{20} and T_{22}.] No significant changes in the results were found when considering the stronger cut $E_{pp} < 2$ MeV, which might reduce any dilution of the analysing power signals by the P-waves apparent in Fig. 10.2.

The possible existence of two mass regions, where different mechanisms might dominate, is also reflected in the behaviour of the tensor analysing powers shown in Fig. 10.6. It is interesting to note that the minimum in $A_{xx} + A_{yy}$ is at $M_X \approx 1.15$ GeV/c^2, which is precisely the region where there is the biggest disagreement with the cross section predictions of Fig. 10.3. Furthermore, the values of $A_{xx} + A_{yy}$ seem to be remarkably stable, showing a behaviour that is independent of beam energy. Hence, whatever the mechanism is that drives the reaction, it seems to be similar at all energies. The error bars on $A_{xx} - A_{yy}$ are larger since in this case, according to Eq. (8.18), the slope in $\cos 2\varphi$ has to be extracted from the data. As a consequence it is harder to draw as firm conclusions on the analysing power differences.

Although the direct Δ production model of Fig. 10.1a fails to describe the differential cross section data of Fig. 10.3 near the pion production threshold, the situation is much more satisfactory at high M_X. To investigate this region further, the data have been summed over the range $1.19 < M_X < 1.35$ GeV/c^2 and the tensor analysing powers A_{xx} and A_{yy} evaluated separately as functions of the transverse momentum transfer q_t. The results at the three energies are shown in Fig. 10.7.

Within the experimental uncertainties, the values of both A_{xx} and A_{yy} at fixed q_t seem to be largely independent of the beam energy. This is consistent with a similar feature found for the data at fixed M_X shown in Fig. 10.6. This suggests that there is a common reaction mechanism at all three energies. Another important point to note is that the signs of A_{xx} and A_{yy} are opposite to those measured in the $\vec{d}p \to \{pp\}_s n$ reaction, presented in section 9.1. Though, unlike the neutron channel case, they tend to be very small at $q_t \approx 0$.

The theoretical calculations, shown as curves in Fig. 10.7, are implemented for the direct one-pion-exchange mechanism in the $^1S_0$ limit [78]. However, neither of the resulting predictions agrees even qualitatively with the experimental data, which show very small analysing powers for $q_t \approx 0$. Nevertheless, if one looks instead at the combination $A_{xx} - A_{yy}$ it seems the one-pion-exchange model does give a plausible description of the data. In particular it predictes that $A_{yy} > A_{xx}$ for Δ production.

A simple average over the three beam energies of the experimental data is

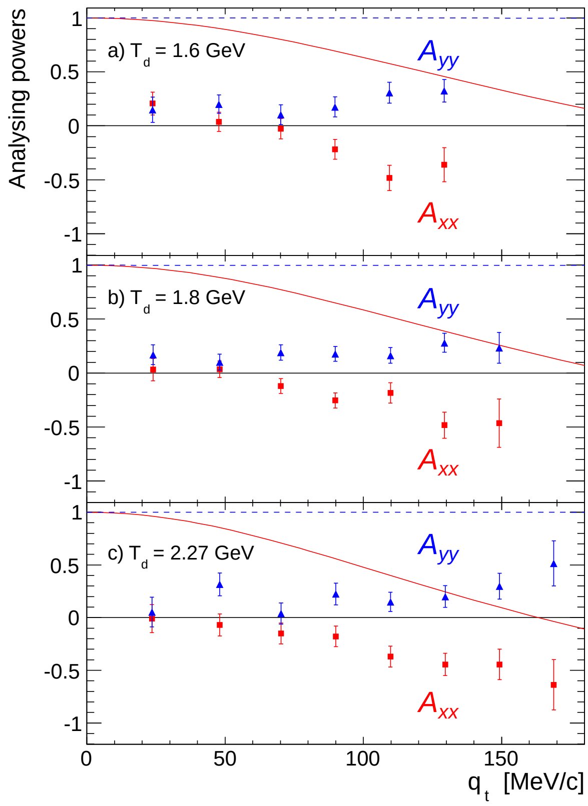

Figure 10.7: Acceptance-corrected tensor analysing powers A_{xx} and A_{yy} of the $\vec{d}p \to \{pp\}_s X$ reaction with $E_{pp} < 3$ MeV at three deuteron beam energies as a function of the transverse momentum transfer q_t (numerical values are listed in Table B.6). Only high mass data ($1.19 < M_X < 1.35$ GeV/c^2) are considered. Though the error bars are dominantly statistical, they include also the uncertainties from the beam polarisation and relative luminosity C_n. In addition, there is an overall uncertainty of up to 4% due to the use of the polarisation export technique. The one-pion-exchange predictions are shown by the blue dashed line for A_{yy} and red solid for A_{xx}.

shown in Fig. 10.8, together with the one-pion-exchange predictions for the spherical analysing power $T_{22} = (A_{xx} - A_{yy})/2\sqrt{3}$. Since no strong energy dependence of the tensor analysing powers was found in the data, the energies were combined to improve the statistics.

In summary, the results achieved clearly show that the rich features of the $pn \to \Delta^0 n$ amplitude cannot be reproduced by considering only π exchange. In addition to a possible direct $\Delta^0(1232)$ peak, there is a surprising amount of production in the s-wave πN region, as we saw in the data. This could not be explained in terms of Δ excitation in the projectile deuteron. Strength in this region could also arise

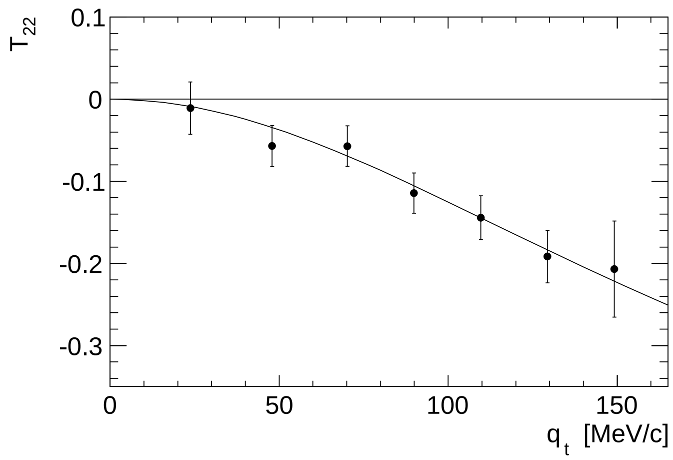

Figure 10.8: Spherical tensor analysing power $T_{22} = (A_{xx} - A_{yy})/2\sqrt{3}$ for the $\vec{d}p \to \{pp\}_s X$ reaction with $E_{pp} < 3$ MeV, averaged over the three beam energies studied. Though the error bars are dominantly statistical, they include also the uncertainties from the beam polarisation and relative luminosity C_n. In addition, there is an overall uncertainty of up to 4% due to the use of the polarisation export technique. When the same approach is applied to the predictions of the simple one-pion-exchange model of Fig. 10.1a, the good agreement shown by the curve is achieved.

from higher-order diagrams involving a ΔN residual interaction [84], which have been neglected here.

10.1.3 Comparison with other experiments

The SPESIV spectrometer at SATURNE had high resolution but very small angular acceptance. The $T_d = 2$ GeV data were therefore taken at discrete values in the laboratory diproton production angle, typically in steps of $\approx 2°$. The limited acceptance also meant that only a linear combination of A_{xx} and A_{yy} (the "polarisation response") could be determined and it was only at the larger angles that this approached a pure A_{yy} measurement. The ANKE data have been analysed in much finer angular bins but the M_X distribution in the Δ region of the cross section and polarisation response is quite similar to that measured at SATURNE at $\vartheta_{\text{lab}} = 2.1°$ [70, 72], which is in the middle of the ANKE angular range. The comparison of the ANKE results for this quantity with those from Saclay is shown in Fig. 10.9. Taking into account the error bars and the difference in beam energy, it seems that these two experiments are consistent with each other.

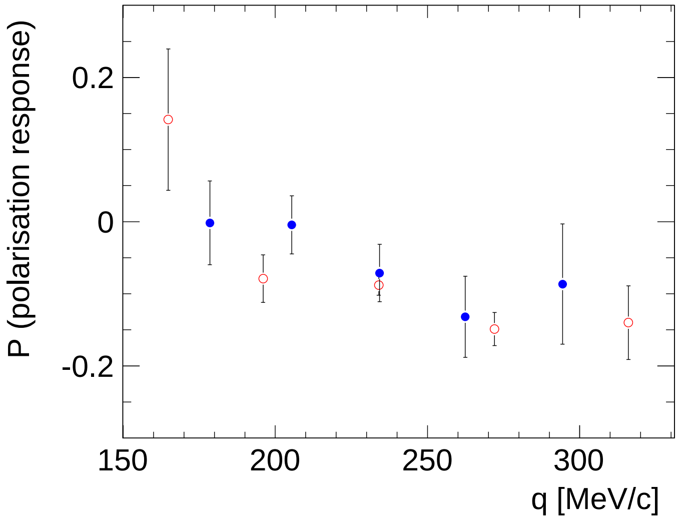

Figure 10.9: The comparison of the ANKE results at $T_d = 2.27$ GeV (blue points) with results produced at Saclay at $T_d = 2.0$ GeV (red circles). Results are shown in terms of the full momentum transfer.

10.2 Spin-correlation parameters in the $np \to d\pi^0$ reaction

The double-polarised data, obtained in 2009, provide an excellent possibility to study spin-correlation parameters of any reaction that we are able to identify. One of the most important of these is quasi–free $np \to d\pi^0$ which was widely used in all our data analysis in luminosity measurement and in beam/target polarimetry. As was described in sections 6.3 and 8.4, it has a reasonably high counting rate, at least at 1.2 GeV, and is clearly identified at ANKE.

The $pp \to d\pi^+$ reaction has been used for a long time to test countless phenomenological models of pion production at intermediate energies, some of which are summarised in Refs. [84, 85]. Furthermore, the reaction has also been frequently discussed within the framework of chiral perturbation theory [86]. Many measurements of the cross section, analysing powers, spin correlations and spin transfers exist. For these data the partial wave analyses have been carried out for proton beam energies up to 1.3 GeV [66].

Isospin invariance requires that the cross section for $np \to d\pi^0$ should be half of that for $pp \to d\pi^+$ but all the spin observables should be identical for the two reactions. However, there have been relatively few measurements of the neutron-induced cross section [87, 88] and even less is known about the spin dependence. Hence, ANKE is able to improve the situation by providing useful data on $np \to d\pi^0$ at small angles, which are largely absent from the existing data.

Equation (8.6) for the $np \to d\pi^0$ reaction gives the following dependence on the pion azimuthal angle φ_π is

$$\begin{aligned} \frac{d\sigma}{d\Omega} &= \left(\frac{d\sigma}{d\Omega}\right)_0 \left[1 + (PA_y^P(\vartheta_\pi) + QA_y^Q(\vartheta_\pi))\cos\varphi_\pi \right. \\ &\left. \qquad + PQ\left(A_{y,y}(\vartheta_\pi)\cos^2\varphi_\pi + A_{x,x}(\vartheta_\pi)\sin^2\varphi_\pi\right)\right], \qquad (10.6) \end{aligned}$$

where P and Q are vector polarisations of the incident neutron and target proton, respectively. It should be noted that

$$A_y^P(\vartheta_\pi) = -A_y^Q(\pi - \vartheta_\pi) \qquad (10.7)$$

As was already mentioned in section 7.2, the Fermi motion of the neutron in the deuteron introduces an incident angle that can be several degrees in the laboratory system. A second effect, caused especially by the longitudinal component of the Fermi momenta, is that in a quasi-free reaction the c.m. energy $\sqrt{s}$ is not unambiguously fixed by the incident deuteron beam energy. Although in our case the effective neutron energy $T_{\text{neutron}} = [s - (m_p + m_n)^2]/2m_p$ is constructed for every event, the limited statistics and the finite resolution mean that data must be grouped over a relatively wide energy range. Under such circumstances, as a result, we get weighted averages of the observables, where the neutron kinetic energy times the acceptance applies as a weight.

The distributions in effective neutron beam energy for all the $dp \to p_{\text{spec}} dX$ events that fall within the $\pm 2.5\sigma$ of the π^0 peaks in Fig. 8.5, and are limited by the $P_{\text{spec}} < 106$ MeV/c, are shown in Fig. 10.10. In the data analysis the wings of the distribution were cut and only data in the region $500 < T_{\text{neutron}} < 700$ MeV were retained.

For the $\vec{d}\vec{p} \to \{pp\}_s n$ studies the vector polarisation P of the beam was determined using the $np \to d\pi^0$ reaction, as described in section 8.4. The results obtained at $T_d = 1.2$ GeV demonstrated good agreement with impulse approximation predictions. Since it is mainly the PQ product of the beam and target polarisations that determines the precision of a spin correlation, we decided to use the $\vec{d}\vec{p} \to \{pp\}_s n$

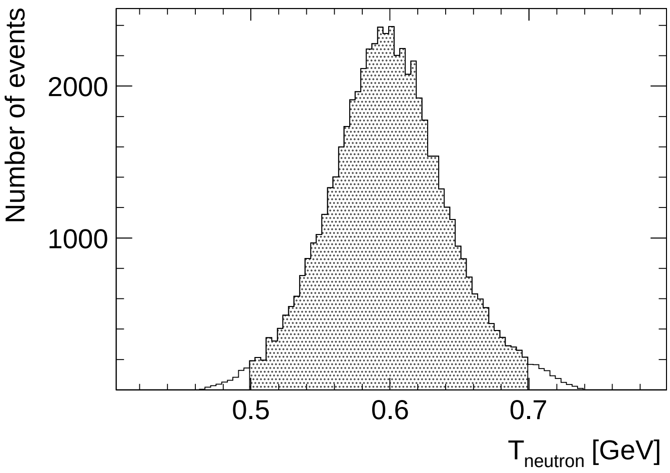

Figure 10.10: Effective neutron beam energy for the quasi-free $np \to dX$ reaction obtained with a 106 MeV/c spectator momentum cut for those events that fall within the $\pm 2.5\sigma$ of the π^0 peak. Data within the shaded area, corresponding to $500 < T_{\text{neutron}} < 700$ MeV, were retained in the analysis.

events and determine the PQ directly.

Using the predictions [38] for the transverse spin correlation at small momentum transfers in the $\vec{d}\vec{p} \to \{pp\}_s n$ reaction the value of $PQ = 0.372 \pm 0.010$ was obtained. The error bar here includes the uncertainty in the correction coming from the difference between $|Q_\uparrow|$ and $|Q_\downarrow|$. In addition, there might be systematic uncertainties in the model and in the neutron-proton charge-exchange amplitudes [1] used in the estimations. The contribution of these uncertainties in the value of PQ might be up to 10%.

The procedures for extracting the values of the spin correlations are very similar to those used for the $\vec{d}\vec{p} \to \{pp\}_s n$ reaction (see section 9.2). In both cases the φ_π dependence of Eq. (10.6) has to be fitted in order to extract $A_{x,x}$ and $A_{y,y}$ separately. The results in this case, shown in Fig. 10.11, are in reasonable agreement with the predictions of the SAID $pp \to d\pi^+$ partial wave analysis [66] averaged over the neutron energy distribution shown in Fig. 10.10. Note that near 600 MeV the energy dependence of the spin correlations, as predicted by SAID, are nearly linear. Hence, the averaging the predictions over our energy range (200 MeV width) gives a tiny difference from that at our effective energy of 598.3 MeV, which is very close to the central energy.

We have plotted other available data in the vicinity of 600 MeV. There are no measurements at all of $A_{x,x}$ for $\vec{n}\vec{p} \to d\pi^0$ in this energy domain and those for $A_{y,y}$ are generally at larger angles [89, 90], as shown in Fig. 10.11b. The large negative values obtained in the forward direction are to be expected because at 600 MeV there is sufficient energy to produce a $\Delta(1232)$ plus a nucleon at rest in the c.m. frame and such an intermediate state would lead to $A_{x,x} = -1$.

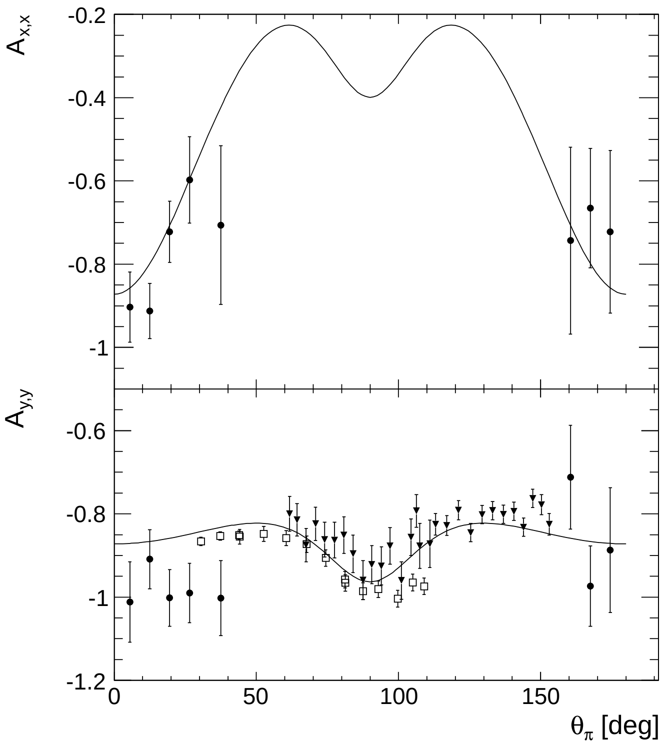

Figure 10.11: The values of $A_{x,x}$ and $A_{y,y}$ measured in the $\vec{n}\vec{p} \to d\pi^0$ at energies around 600 MeV as a function of the pion polar angle ϑ_π in the c.m. frame (numerical values are listed in Table B.7). Only statistical errors are shown. The results are compared with the SAID predictions [66], which have been weighted with the measured energy distribution. Also shown are the PSI $\vec{p}\vec{p} \to d\pi^+$ results at 578 MeV (closed triangles) [89] and those of LAMPF at 593 MeV (open squares) [90].

The results for the $A_{x,x}$ and $A_{y,y}$ spin-correlation coefficients for the $\vec{n}\vec{p} \to d\pi^0$ reaction are published in Ref. [91] together with other ANKE data at 353 MeV. The two measurements, one close to threshold where the s-wave pion production is important and the other in a region where p-wave production is dominant, being largely driven by the S-wave $\Delta(1232)N$ intermediate state, are consistent with the current SAID solution for $pp \to d\pi^+$. However, our measurements cover the small angle region that is largely absent from existing $\vec{n}\vec{p} \to d\pi^0$ data. No sign is found for any breaking of isospin invariance.

Chapter 11

Summary and Conclusions

We have measured the unpolarised differential cross section and the Cartesian tensor analysing powers in the $\vec{d}p \to \{pp\}_s n$ reaction for small momentum transfers between the proton and neutron by using a hydrogen cluster target in combination with a tensor polarised deuteron beam. The cross section data demonstrated good agreement with the impulse approximation predictions, based on the current SAID solution for the np amplitudes, at $T_n = 600$, 800, and 900 MeV. These amplitudes suffer from much bigger ambiguities at higher energies and the corresponding cross section prediction is about 15% too high compared to our results at 2.27 GeV ($T_n = 1.135$ GeV). It should be noted that the overall normalisation uncertainty of 6% is the worst at this energy, but it is still smaller than the observed discrepancy. The suspicion must fall on the SAID solution, which predicts an unpolarised $np \to pn$ cross section that may be up to 10% too large [2], of which the spin-dependent contribution is also about 10% too large [8].

Like the cross section data, the description of A_{xx} and A_{yy} is also very good at the three lower energies but much poorer at 2.27 GeV. Generally speaking, the impulse approximation should perform better as the energy is raised. Hence, attention is once again focussed on the SAID np amplitudes. The strength of $|\varepsilon(0)|^2$ in np charge exchange relative to $|\beta(0)|^2 = |\delta(0)|^2$ is determined by the spin-transfer parameters $K_{LL}(0)$ and $K_{NN}(0)$, but there are no measurements of these quantities in the relevant angular and energy region. This questions the precision of the SAID program when providing np amplitudes for the estimation of deuteron tensor analysing powers. To fit our data, we have reduced the SAID prediction for $\varepsilon(q)$ uniformly by 25% and this reproduces the results much better. Although this might be improved further by introducing a q-dependence in this factor, the present data do not justify such a refinement.

By using the double-polarised data, achieved by replacing the unpolarised hydrogen cluster-jet target by a polarised hydrogen gas cell, it was possible to measure the spin-correlation coefficients $C_{x,x}$ and $C_{y,y}$ in the $\vec{d}\vec{p} \to \{pp\}_s n$ reaction, but only at 1.2 and 2.27 GeV. The comparison with theory at 1.2 GeV is similar to that for the other observables, while at 2.27 GeV a reduction of the order of 25% seems to be required in the ε input.

We were also able to measure the proton analysing power in the reaction, which was not the primary aim of the experiment, though the data obtained gave this possibility. As with the other observables, impulse approximation reproduces well the small A_y^p signal at 1.2 GeV but fails completely at 2.27 GeV. This suggests that the SAID solution for the γ-amplitude is also unreliable at the higher energy.

In summary, the fact that the impulse approximation with the current SAID input reproduces well all our data below 1 GeV per nucleon gives us confidence that the charge-exchange methodology works well. However, the discrepancies seen at the higher energy suggest the reduction in the strength of the spin-spin amplitudes, especially in the longitudinal direction but an increase in the spin-orbit contribution. It is therefore evident that the charge exchange on the deuteron contains valuable information on the neutron-proton amplitudes. The challenge is to get this used inside the SAID program.

Resent studies of deuteron charge-exchange on hydrogen at ANKE have been also extended into the pion-production regime, as described in chapter 10. Interesting results have been obtained on the differential cross section and tensor analysing powers of the $dp \to \{pp\}_s\Delta^0$ reaction. In addition to a possible direct $\Delta^0(1232)$ peak, the obtained data clearly show a surprising amount of production in the s-wave πN region. Attempts to explain this in terms of Δ excitation in the projectile deuteron give much too low cross sections. In addition, the higher-order diagrams involving a ΔN residual interaction [84] can also be taken into account to describe the data at low M_X region. Although the other observables that will be measured in the future may cast more light on the reaction mechanism, further theoretical work is needed in order that these data may be reliably related to the $\vec{n}p \to \vec{p}\Delta^0$ reaction. We therefore hope that our data will provide further impetus to the construction of more refined $np \to p\Delta^0$ models.

The experiments reported here extend up to the maximum deuteron energy of $T_d = 2.27$ GeV available at COSY. In order to investigate even higher energies at this facility, an experiment should be undertaken in inverse kinematics with a polarised proton incident on a polarised deuterium gas cell [56, 57]. In this case the two slow protons, ejected at large angles in the laboratory system, have to be detected in the Silicon Tracking Telescopes [92]. This will allow the studies reported here to be continued up to 2.8 GeV per nucleon [93, 94, 95].

Chapter 12

Outlook

12.1 Continuation of the np programme at ANKE

The experimental work described in this thesis is a successful continuation of the extensive np programme at ANKE that aims to study different spin observables by using polarised beams and targets at COSY. The investigation of the $dp \to \{pp\}_s X$ reaction demonstrates interesting results for both the neutron ($X = n$) and the Delta ($X = \Delta^0$) channels, especially at higher energies where relatively little is known about the np charge–exchange amplitudes. Hence, ANKE can provide useful experimental data, capable of improving the existing np database in the small-angle region. Moreover, the data obtained in the Δ channel can be used as a valuable constraint in modelling the $np \to p\,\Delta^0$ amplitudes in the future.

Although very successful, the basic limitation in this approach is set by the maximum deuteron energy that can be achieved in COSY, which means that the np interaction could only be studied up to a neutron kinetic energy of about 1.15 GeV. It was therefore always envisaged that the continuation of the programme would be in inverse kinematics, with a proton beam incident on a polarised deuterium gas cell. We have therefore suggested to extend the energy range up to about 2.9 GeV by using a polarised proton beam incident on a polarised deuterium target and detecting two slow protons in an array of solid state telescopes. The interaction vertex is then very well located within the long target, making it unnecessary to measure the fast neutron in the ANKE facility to identify the $\vec{d}(\vec{p}, pp)n$ reaction. Eventually this approach might be extended to the production of the $\Delta^0(1232)$ isobar with some of its decay products being detected in ANKE.

12.2 Deuterium commissioning run

In June 2012, we conducted an experiment [94] for the commissioning of the polarised internal deuterium gas target at ANKE and the starting of an initial research programme. The ANKE detection system used in these measurements included two Silicon Tracking Telescope (STT) system positioned to the left and right of the storage cell target.

One of the main aims of the commissioning run was the determination of the vector and tensor polarisations of the deuterium storage cell gas target by studying various nuclear reactions. The experiment was done using about $6 - 8 \times 10^9$ stored unpolarised protons with a beam energy of $T_p = 600$ MeV and a (vector and tensor) polarised deuterium gas target of density $n_d \leq 10^{13}$ cm^{-2}. This resulted in an average luminosity value of $L \approx 5 - 7 \times 10^{28}$ cm^{-2} s^{-1}. The data-taking lasted for around 10 days.

The storage cell that was used in this experiment was similar to that used in double-polarised experiment in 2009 (see section 4.3). The beam was also developed quite similarly, employing electron cooling and stacking injection.

The ABS source [54] was prepared to produce two mixed (vector and tensor) and two pure (only tensor) polarisation modes. The unpolarised gas was provided by the UGSS system [56]. The polarisation mode of the target was changed every ten seconds.

The vector polarisation of the deuterium target was measured with the quasi-free $p\vec{p} \to d\pi^+$ reaction, for which the analysing power predictions were taken from the SAID database. In contrast, the $p\vec{d}$ elastic scattering depends strongly on both the vector and tensor polarisations of the deuterium target. Fortunately the vector and tensor analysing powers of this reaction have been measured with polarised deuteron beams at Argonne [96] for $T_d = 1194$ MeV, at SATURNE [97, 98] for $T_d = 1198$ MeV, and at ANKE [99] for $T_d = 1170$ MeV. The ANKE acceptance is sufficient to allow us to extract the analysing powers for the deuterium target from this reaction at $T_p = T_d/2$.

12.3 Breakup process in inverse kinematics $\vec{d}(\vec{p}, pp)X$

As mentioned in the introduction, the main aim is the study of the $pd \to \{pp\}_s n$ break up, where both slow protons are detected in the STT. Such data are shown in Fig. 12.1. It seems that the design of the current silicon tracking telescopes unfortunately does not allow one to access the region where E_{pp} and q are simultaneously small. The STT have three layers and, in order to get a good kinematic determination, the proton has to pass through the first, which requires a minimum energy of ≈ 2.5 MeV, *i.e.* a momentum of ≈ 70 MeV/c. If the protons are detected in the same STT, then E_{pp} can be small but the momentum transfer must be at least twice the 70 MeV/c. If the protons are detected in separate STT, q can be small but the excitation energy E_{pp} must be at least twice 2.5 MeV.

To check the quality of the breakup data, since the target polarisation had already been determined, we tried to evaluate tensor analysing powers. Although we had measured these observables in the dp kinematics before, these could provide an additional check of the whole procedure. However, in pd kinematics, as we already saw in Fig. 12.1, small E_{pp} data are only available at relatively large momentum transfers, extending the previously investigated q range up to 400 MeV/c.

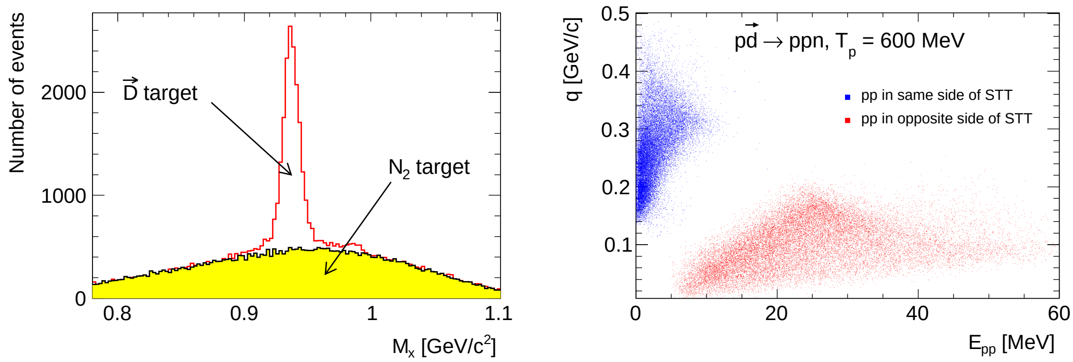

Figure 12.1: The left panel represents the missing-mass spectra of two slow protons being detected in the STT when using a polarised deuterium target or filling the cell with nitrogen gas, at $T_p = 600$ MeV. The three-momentum transfer q versus the pp excitation energy for those events that fall within the $\pm 3\sigma$ of the neutron peak is shown in the right panel.

Using exactly the same technique, as for the $(\vec{d}, pp)$ case described in section 9.1, the values of A_{yy} obtained are presented in Fig. 12.2 (*preliminary result*). New data are shown together with the old, obtained in the $(\vec{d}, pp)$ kinematics at $T_d =$

1.2 GeV. Impulse approximation predictions are shown as solid curves on the figure. Unfortunately, the azimuthal φ angle coverage is limited to very small ($\varphi \approx 0°$) and very large ($\varphi \approx \pm 180°$) angles due to the current setup of the STTs, leading to insufficient data for determining both transverse components of the tensor analysing power.

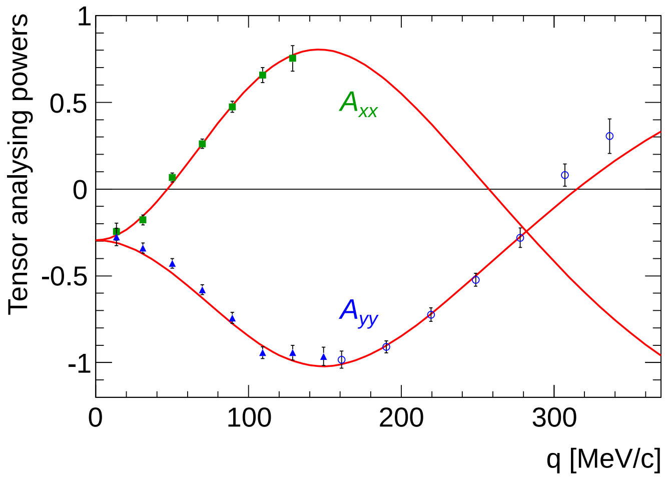

Figure 12.2: Tensor analysing powers A_{xx} (green squares) and A_{yy} (blue triangles) of the $\vec{d}p \to \{pp\}_s n$ reaction ($q < 160$ MeV/c) from the old ANKE measurements using polarised deuteron beam at $T_d = 1.2$ GeV [40]. The new *preliminary* results on A_{yy} (blue circles) were obtained in inverse kinematics ($q > 160$ MeV/c), using the polarised deuterium target and unpolarised proton beam at $T_p = 600$ MeV.

The agreement between the new and the old data is very encouraging, as is the success of the impulse approximation in this q region. All these seem very promising in the studies of np charge-exchange amplitudes at higher energies and higher momentum transfers. Hence, the logical continuation of these studies will be to undertake a double-polarised experiment, which will allow measurements of spin-correlation parameters in the $\vec{d}(\vec{p}, pp)X$ reaction at the maximum proton beam energy of 2.8 GeV at COSY. For this purpose a new experiment was proposed [95], which has already been accepted and will be undertaken in 2014. We hope that the new experiment will provide more interesting data and more clues for the understanding of the nucleon-nucleon interaction.

12.4 Predictions for the breakup spin observables at higher momentum transfers

One of the energies employed in the new experiment will be $T_p = 1.15$ GeV, which will provide a connection with our earlier data at $T_d = 2.3$ GeV, where we found significant deficiencies in the current np database. In order to allow estimates of counting rates for the $p\vec{d} \to \{pp\}_s n$ reaction, the impulse approximation program was run out to larger values of the momentum transfer using the standard SAID np charge-exchange amplitudes as input. The results at 1.135 GeV are shown in Fig. 12.3, where the usual $E_{pp} < 3$ MeV cut was imposed.

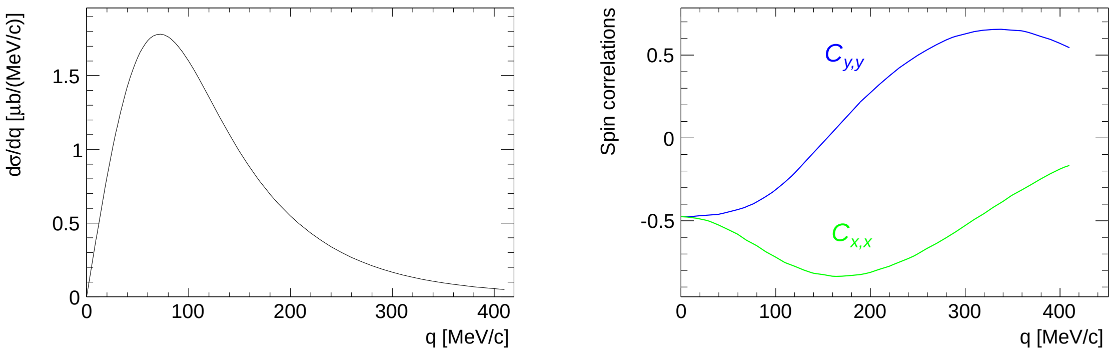

Figure 12.3: Impulse approximation predictions for the differential cross section (left panel) and transverse spin correlation parameters (right panel) for the $p\vec{d} \to \{pp\}_s n$ reaction at $T_p = 1.135$ GeV for three-momentum transfers up to $q = 400$ MeV/c.

Although the values of A_{xx}, A_{yy}, $C_{x,x}$, and $C_{y,y}$ are expected to be quite significant, this must be balanced against the much smaller cross section predicted at large q. The changes in the analysing power signals arising from double scattering in the deuteron are small for the kinematics of our earlier experiments but certainly cannot be neglected at the larger momentum transfers shown in Fig. 12.3. Such effects can be taken into account in the modelling [5].

Acknowledgements

I would here like to express my gratitude to those who supported me in successfully accomplishing the mission, called PhD study.

First of all, I would like to thank Prof. Dr. H. Ströher for providing the great opportunity to work in his group in the Nuclear Physics Institute of the Forschungszentrum Jülich, and creating such a nice working atmosphere for me. Many presentations that I have made during these years have been heavily influenced by his perceptive comments and very useful suggestions.

I would like to thank my supervisors Prof. Dr. M. Nioradze and Dr. M. Tabidze for releasing the PhD programme I have applied for, and also for very usefull and interesting lectures they were giving during my study. This helped me a lot later in the data analysis. I appreciate their trust and support during all of this time.

I am also grateful to Dr. A. Kacharava for being my advisor in Jülich and provided ceaseless help in structuring and writing papers and this thesis. In addition, I would like to thank him and his family for their hospitality and their support in everyday life.

I would like to thank Dr. D. Chiladze for introducing me to many useful techniques in the data analysis. His suggestions were very useful, especially in the beginning when everything was very new and seemed very difficult. I have had many conversations with Dr. S. Dymov, which provided insight about Monte Carlo simulation, which was very important for the data analysis. Considering that the programming was always a very interesting subject for me, all these together helped very much to improve my programming skills.

My greatest debt is to Prof. Dr. C. Wilkin, whose thoughtful advice was always giving me the right direction in solving many problems during my PhD study. Despite him being a theorist, his suggestions relating the experimental part, have many times shown a way forward.

I would like to thank Dr. F. Rathmann for providing very interesting lectures about the polarisation principles and polarised sources, as well as the polarimetry techniques, and also for taking care of my exam in this subject. A good understanding of these aspects helped me a lot in my work.

I would like to express my gratitude to my Georgian colleagues Dr. N. Lomidze, Dr. G. Macharashvili and Dr. G. Devidze, with whom I have had many interesting discussions, which helped me to acquire knowledge in many aspects of physics. I was feeling their support and assistance at all times. In addition, I would like to thank Dr. G. Devidze for very interesting lectures in the theory of fundamental interactions.

This thesis would not have been possible without the assistance of members of the ANKE collaboration, COSY crew, and IKP staff, who created a very friendly atmosphere to work in.

I also want to thank my friends and relatives who were always interested with my work. That helped me to always remain motivated and keep going.

And finally, I want to say a special thank to my family for their love and care. It was really difficult being so far from home. I thank my family for their patience and understanding and I devote this work to them.

Publications

The experimental techniques and the results presented in this thesis have been published in three refereed papers

- D. Mchedlishvili *et al.* Eur. Phys. J. **A 49**, 49 (2013).
  The neutron-proton charge-exchange amplitudes measured in the $\boldsymbol{dp \to ppn}$ **reaction.**

- D. Mchedlishvili *et al.* Phys. Lett. **B** (2013).
  Excitation of the $\boldsymbol{\Delta(1232)}$ isobar in deuteron charge exchange on hydrogen at 1.6, 1.8, and 2.3 GeV
  (http://dx.doi.org/10.1016/j.physletb.2013.08.018)

- V. Shmakova, D. Mchedlishvili *et al.* Phys. Lett. **B** (2013).
  First measurements of spin correlations in the $\boldsymbol{\vec{n}\vec{p} \to d\pi^0}$ **reaction.**
  (arXiv:1307.4950)

Appendix A

Principles of polarisation

This section describes the polarisation aspects of beams of spin-1/2 and spin-1 particles. It is taken largely from Ref. [50] and is provided here for completeness.

In quantum mechanics all spin angular momentum operators S_i satisfy the equation:

$$S_i S_j - S_j S_i = \epsilon_{ijk} S_k \, , \tag{A.1}$$

where ϵ_{ijk} is the totally antisymmetric tensor.

These spin operators are hermitian and their trace is 0. We have three components in a Cartesian coordinate system S_x, S_y, and S_z which defines the vector $\vec{S}$. Their eigenvalues and eigenfunctions satisfy:

$$\vec{S}^2 \left| sm \right\rangle = s\left(s+1\right)\hbar \left| sm \right\rangle \ , \tag{A.2}$$

$$S_z \left| sm \right\rangle = m\hbar \left| sm \right\rangle \ \ m = -s, -s+1, ..., +s \, , \tag{A.3}$$

where $\left| sm \right\rangle$ is the eigenfunction of $\vec{S}^2$ and one of its projection, conventionally chosen to be the z projection. It depends on two quantum numbers: spin quantum number s and magnetic quantum number m. The number of values of m is $(2s+1)$.

When $s = 1/2$, we then have two values $m = -1/2$ or $m = +1/2$. We can write the spin operator in terms of matrices with the Pauli definition:

$$\vec{S} = \tfrac{1}{2}\hbar\vec{\sigma} \, , \tag{A.4}$$

where

$$\sigma_x = \begin{pmatrix} 0 & 1 \\ 1 & 0 \end{pmatrix} \quad \sigma_y = \begin{pmatrix} 0 & -i \\ i & 0 \end{pmatrix} \quad \sigma_z = \begin{pmatrix} 1 & 0 \\ 0 & -1 \end{pmatrix} \tag{A.5}$$

The set of these three Pauli matrices and unit matrix form a complete set of hermitian matrices for $s = 1/2$. Every hermitian operator in these space is linear combination of these operators.

A.1 Spin 1/2

The above describes a single particle with $\langle S_z \rangle = \pm\frac{1}{2}\hbar$ and corresponding $\langle \sigma_z \rangle = \pm 1$. It is, however, impossible to describe things in such a way when there is ensemble of particles (for example a beam). To represent such ensemble in quantum mechanics, it is convenient to define the density matrix:

$$\rho = \sum_{i=1}^{n} p_i \left| sm_i \right\rangle \left\langle sm_i \right| \,, \tag{A.6}$$

with:
$n \equiv$ number of the pure states (here $n = 2$);
$p_i \equiv$ probability of i state in the ensemble.

It helps to describe polarisation with three components p_i ($i = x, y, z$) which are the expectation values of the Pauli operators $\langle \sigma_i \rangle$. We can write it in the short way:

$$p_i = \langle \sigma_i \rangle = \mathrm{Trace}\left(\rho \sigma_i\right) \,. \tag{A.7}$$

These are the components of a vector $\vec{p} = (p_x, p_y, p_z)$. The polarisation $\vec{p}$ is the vector polarisation of the ensemble of particles with spin 1/2. Here we should be carefully because in quantum mechanics only one component can be measured. Taking this to be the z-component:

$$p_z^* = \langle \sigma_z \rangle = \mathrm{Trace}\left(\rho \sigma_z\right) = p_+ \left\langle + \middle| \sigma_z \middle| + \right\rangle + p_- \left\langle - \middle| \sigma_z \middle| - \right\rangle = p_+ - p_- \,. \tag{A.8}$$

When $p_z^* = 0$, it means that $p_+ = p_-$ and the probabilities of $|1/2, +1/2\rangle$ and

$|1/2, -1/2\rangle$ states are equal. The state with $m = +1/2$ is populated with the same number of particles N_+ as the $m = -1/2$ states N_-.

If $p_+ > p_-$, it means that there are more particles in state $|1/2, +1/2\rangle$, and $N_+ > N_-$. So we have polarisation along the z axis:

$$p_z^* = p_+ - p_- = \frac{N_+}{N_{tot}} - \frac{N_-}{N_{tot}} = \frac{N_+ - N_-}{N_+ + N_-}\,, \tag{A.9}$$

from which we evidently get:

$$-1 \leq p_z^* \leq +1\,. \tag{A.10}$$

If all particles in the beam are in the state $m = 1/2$, then we get polarisation of the beam $p_z^* = 1$, or if all particles are in the state $m = -1/2$, we have $p_z^* = -1$.

A.2 Spin 1

There are three possible eigenvalues of S_z with its eigenfunctions from Eq. (A.3). So, we have three pure state for the spin 1 particles:

$$|s = 1; m = 1\rangle \quad |s = 1; m = 0\rangle \quad |s = 1; m = -1\rangle\;. \tag{A.11}$$

The spin operator $\vec{S}$ is therefore a 3×3-matrix and one can write them like the Pauli operators:

$$S_x = \frac{1}{\sqrt{2}}\begin{pmatrix} 0 & 1 & 0 \\ 1 & 0 & 1 \\ 0 & 1 & 0 \end{pmatrix} \quad S_y = \frac{i}{\sqrt{2}}\begin{pmatrix} 0 & -1 & 0 \\ 1 & 0 & -1 \\ 0 & 1 & 0 \end{pmatrix} \quad S_z = \begin{pmatrix} 1 & 0 & 0 \\ 0 & 0 & 0 \\ 0 & 0 & -1 \end{pmatrix} \tag{A.12}$$

These three operators together, with 3×3 unit matrix, comprise four hermitian operators, which are linear independent. It is however evident that nine are needed to 'span' the 3×3 space. Each spin operator has to have zero trace and each will be orthogonal to the unit matrix U which means that its expectation value will be zero for an unoriented ensemble. One can construct from the available matrices:

$$S_{ij} = \frac{3}{2}(S_i S_j + S_j S_i) - 2U\delta_{ij}\,, \qquad (\text{with } i, j = x, y, z)\,. \tag{A.13}$$

With this one obtains six matrices but, since Trace(S) = 0, we get only five linear independent matrices:

$$p_{ij} = \langle S_{ij} \rangle = \mathrm{Trace}(\rho S_{ij})\,. \tag{A.14}$$

We can define p_{ij} in a similar way to p_i:

$$p_{zz} = \langle S_{zz} \rangle = \mathrm{Trace}(\rho S_{zz})\,. \tag{A.15}$$

It is possible to compose a 3×3 matrix from the different components of p_{ij}, which is a second rank tensor, and defines a tensor polarisation of the beam. The definition of the vector polarisation is the same Eq. (A.12), but we can write p^*_{zz} with the occupation number of three spin states:

$$p^*_{zz} = \langle S_{zz} \rangle = \mathrm{Trace}(\rho S_{zz}) = p_+ + p_- - 2p_0\,. \tag{A.16}$$

If all three states are occupied equally in the beam, $p_+ = p_- = p_0 = 1/3$, then we have an unpolarized beam with $p^*_{zz} = 0$ and $p^*_z = 0$. In general

$$p^*_{zz} = p_+ + p_- - 2p_0 = \frac{N_+ + N_- - 2N_0}{N_{tot}}\,. \tag{A.17}$$

From this it follows that:

$$-2 \le p^*_{zz} \le 1\,. \tag{A.18}$$

For illustration see Fig. A.1. Knowing the tensor polarisation gives us information

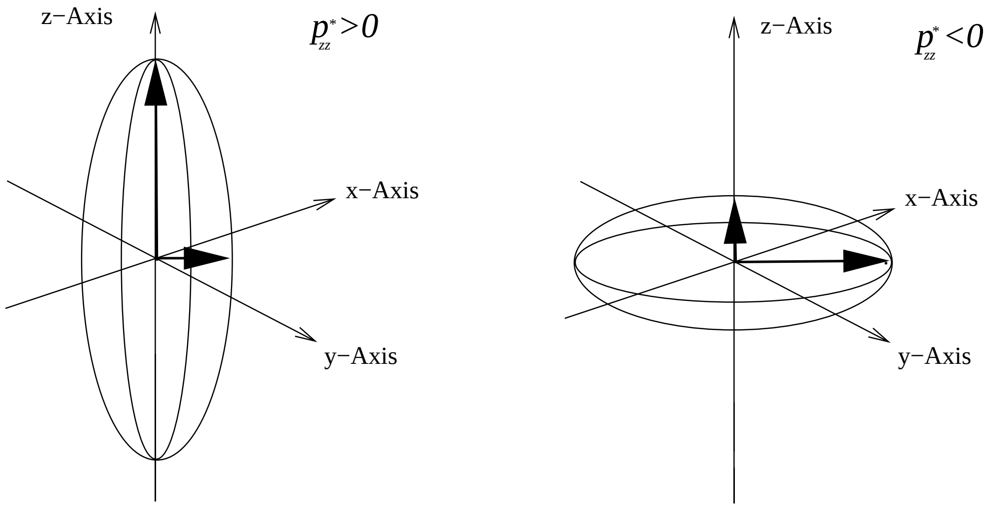

Figure A.1: Positive and negative tensor polarisations about the relation between $N_+ + N_-$ and N_0. The vector polarisation (relation between N_+ and N_-), together with intensity $N_{tot} = N_+ + N_- + N_0$, gives us all the information about the occupation of the states.

Appendix B

Numerical values

	q [MeV/c]	A_{xx}	A_{yy}
1.6 GeV	13.5	-0.269 ± 0.033	-0.366 ± 0.032
	28.6	-0.224 ± 0.024	-0.339 ± 0.024
	40.2	-0.109 ± 0.025	-0.437 ± 0.025
	50.1	-0.032 ± 0.024	-0.490 ± 0.023
	60.1	0.077 ± 0.022	-0.545 ± 0.022
	70.0	0.186 ± 0.023	-0.647 ± 0.022
	79.9	0.331 ± 0.024	-0.730 ± 0.022
	91.8	0.445 ± 0.020	-0.811 ± 0.019
	107.6	0.635 ± 0.024	-0.937 ± 0.021
	124.0	0.764 ± 0.025	-1.045 ± 0.022
	145.3	0.780 ± 0.033	-1.109 ± 0.023
	172.6	0.696 ± 0.071	-1.123 ± 0.028
1.8 GeV	13.5	-0.395 ± 0.036	-0.324 ± 0.038
	28.6	-0.212 ± 0.027	-0.376 ± 0.026
	40.2	-0.110 ± 0.029	-0.408 ± 0.029
	50.1	-0.076 ± 0.025	-0.518 ± 0.026
	60.1	0.084 ± 0.027	-0.530 ± 0.026

	70.0	0.208 ± 0.026	-0.666 ± 0.024
	79.9	0.306 ± 0.027	-0.717 ± 0.024
	91.8	0.489 ± 0.023	-0.836 ± 0.021
	107.7	0.576 ± 0.025	-0.978 ± 0.022
	124.1	0.699 ± 0.026	-1.002 ± 0.022
	145.6	0.756 ± 0.031	-1.081 ± 0.025
	172.6	0.768 ± 0.051	-1.140 ± 0.027
2.27 GeV	13.3	-0.405 ± 0.069	-0.399 ± 0.074
	30.9	-0.256 ± 0.044	-0.468 ± 0.044
	50.3	-0.022 ± 0.038	-0.544 ± 0.036
	69.9	0.135 ± 0.037	-0.657 ± 0.036
	89.7	0.325 ± 0.038	-0.830 ± 0.040
	109.6	0.509 ± 0.042	-0.958 ± 0.044
	129.3	0.734 ± 0.050	-1.147 ± 0.050
	149.4	0.784 ± 0.061	-1.200 ± 0.059
	169.2	0.780 ± 0.077	-1.135 ± 0.070
	188.9	0.608 ± 0.120	-1.116 ± 0.088

Table B.1: Tensor analysing powers A_{xx} and A_{yy} of the $\vec{d}p \to \{pp\}_s n$ reaction at three beam energies for low diproton excitation energy, $E_{pp} < 3$ MeV, as shown in Fig. 9.3. Though the error bars are dominantly statistical, they include also the uncertainties from the relative luminosity C_n and the beam polarisations determined at 1.2 GeV. In addition, at the higher energies there is an overall uncertainty of up to 4% due to the use of the polarisation export procedure.

q [MeV/c]	$d\sigma/dq$ [μb/(MeV/c)]			
	1.2 GeV	1.6 GeV	1.8 GeV	2.27 GeV
5	0.452 ± 0.030	0.279 ± 0.022	0.276 ± 0.023	0.155 ± 0.016
15	1.234 ± 0.044	0.895 ± 0.035	0.839 ± 0.037	0.635 ± 0.034
25	2.177 ± 0.063	1.345 ± 0.041	1.290 ± 0.043	0.907 ± 0.038
35	2.852 ± 0.073	1.896 ± 0.050	1.598 ± 0.046	1.235 ± 0.044
45	3.133 ± 0.076	2.127 ± 0.049	2.108 ± 0.054	1.442 ± 0.044
55	3.511 ± 0.087	2.432 ± 0.052	2.178 ± 0.051	1.575 ± 0.044
65	3.636 ± 0.092	2.555 ± 0.052	2.349 ± 0.052	1.663 ± 0.044
75	3.541 ± 0.092	2.439 ± 0.049	2.283 ± 0.048	1.572 ± 0.041
85	3.500 ± 0.098	2.409 ± 0.048	2.200 ± 0.046	1.594 ± 0.042
95	3.413 ± 0.105	2.206 ± 0.045	2.083 ± 0.044	1.479 ± 0.040
105	3.163 ± 0.101	2.062 ± 0.044	1.921 ± 0.042	1.244 ± 0.035
115	2.961 ± 0.104	1.923 ± 0.045	1.791 ± 0.042	1.133 ± 0.032
125	2.504 ± 0.102	1.762 ± 0.046	1.595 ± 0.041	1.036 ± 0.032
135	2.240 ± 0.105	1.580 ± 0.046	1.513 ± 0.043	0.919 ± 0.031
145	1.925 ± 0.108	1.488 ± 0.049	1.280 ± 0.041	0.868 ± 0.032
155		1.233 ± 0.048	1.240 ± 0.044	0.740 ± 0.032
165		1.046 ± 0.048	1.043 ± 0.042	0.673 ± 0.033
175		0.988 ± 0.054	0.912 ± 0.042	0.561 ± 0.033
185		0.922 ± 0.062	0.834 ± 0.046	0.574 ± 0.042
195		0.723 ± 0.075	0.733 ± 0.047	0.376 ± 0.040
205			0.568 ± 0.047	0.439 ± 0.079
215				0.342 ± 0.070

Table B.2: Differential cross sections for the $dp \to \{pp\}_s n$ reaction at four different energies, as shown in Fig. 7.9. The data are integrated over the $E_{pp} < 3$ MeV interval. Only statistical errors are shown; Systematic uncertainties are listed in Table 7.1.

	q [MeV/c]	A_y^p
1.2 GeV	13.7	$(9.2 \pm 18.4) \times 10^{-3}$
	30.6	$(-1.0 \pm 1.1) \times 10^{-2}$
	50.0	$(-2.4 \pm 1.0) \times 10^{-2}$
	69.4	$(-2.0 \pm 1.0) \times 10^{-2}$
	89.1	$(-3.6 \pm 1.1) \times 10^{-2}$
	108.7	$(-5.3 \pm 1.3) \times 10^{-2}$
	128.2	$(-6.8 \pm 1.9) \times 10^{-2}$
2.27 GeV	13.7	$(6.4 \pm 12.8) \times 10^{-3}$
	30.9	$(1.2 \pm 0.7) \times 10^{-2}$
	50.2	$(2.0 \pm 0.7) \times 10^{-2}$
	70.0	$(3.1 \pm 0.7) \times 10^{-2}$
	89.6	$(4.1 \pm 0.8) \times 10^{-2}$
	109.4	$(4.9 \pm 0.9) \times 10^{-2}$
	129.2	$(6.2 \pm 1.2) \times 10^{-2}$
	149.0	$(7.8 \pm 1.5) \times 10^{-2}$
	168.8	$(7.8 \pm 2.0) \times 10^{-2}$

Table B.3: Proton analysing powers A_y^p for the $dp \to \{pp\}_s n$ reaction at $T_d = 1.2$ and 2.27 GeV for $E_{pp} < 3$ MeV, as shown in Fig. 9.6. The error bars do not include the 5% uncertainties arising from the target polarisation.

	q [MeV/c]	$C_{x,x}$	$C_{y,y}$
1.2 GeV	13.7	-0.579 ± 0.047	-0.446 ± 0.044
	30.6	-0.564 ± 0.032	-0.485 ± 0.031
	50.0	-0.588 ± 0.021	-0.504 ± 0.020
	69.4	-0.633 ± 0.026	-0.432 ± 0.024
	89.1	-0.768 ± 0.036	-0.321 ± 0.027
	108.7	-0.759 ± 0.052	-0.204 ± 0.034
	128.2	-0.823 ± 0.105	-0.001 ± 0.048
2.27 GeV	13.7	-0.405 ± 0.034	-0.370 ± 0.032
	30.9	-0.433 ± 0.024	-0.376 ± 0.022
	50.2	-0.460 ± 0.023	-0.362 ± 0.018
	70.0	-0.516 ± 0.024	-0.361 ± 0.022
	89.6	-0.570 ± 0.025	-0.297 ± 0.022
	109.4	-0.641 ± 0.028	-0.214 ± 0.024
	129.2	-0.666 ± 0.032	-0.124 ± 0.028
	149.0	-0.693 ± 0.036	-0.011 ± 0.035
	168.8	-0.737 ± 0.047	0.044 ± 0.041

Table B.4: The spin-correlation coefficients $C_{x,x}$ and $C_{y,y}$ for the $dp \to \{pp\}_s n$ reaction at $T_d = 1.2$ and 2.27 GeV for $E_{pp} < 3$ MeV, as shown in Fig. 9.7. The error bars do not include the 11% uncertainties in the combined beam and target polarisations.

M_X [GeV/c^2]	$d\sigma/dM_X$ [mb/(GeV/c^2)]		
	1.6 GeV	1.8 GeV	2.27 GeV
1.087	$(3.79 \pm 0.28) \times 10^{-2}$	$(4.25 \pm 0.32) \times 10^{-2}$	$(3.48 \pm 0.21) \times 10^{-2}$
1.100	$(9.92 \pm 0.72) \times 10^{-2}$	$(8.95 \pm 0.54) \times 10^{-2}$	$(1.06 \pm 0.06) \times 10^{-1}$
1.114	$(1.28 \pm 0.07) \times 10^{-1}$	$(1.36 \pm 0.08) \times 10^{-1}$	$(1.36 \pm 0.07) \times 10^{-1}$
1.127	$(1.30 \pm 0.07) \times 10^{-1}$	$(1.61 \pm 0.10) \times 10^{-1}$	$(1.60 \pm 0.08) \times 10^{-1}$
1.141	$(1.53 \pm 0.09) \times 10^{-1}$	$(1.74 \pm 0.10) \times 10^{-1}$	$(2.10 \pm 0.09) \times 10^{-1}$
1.154	$(1.62 \pm 0.08) \times 10^{-1}$	$(1.92 \pm 0.10) \times 10^{-1}$	$(2.22 \pm 0.10) \times 10^{-1}$
1.168	$(1.69 \pm 0.08) \times 10^{-1}$	$(2.19 \pm 0.11) \times 10^{-1}$	$(2.91 \pm 0.12) \times 10^{-1}$
1.181	$(1.82 \pm 0.09) \times 10^{-1}$	$(2.50 \pm 0.12) \times 10^{-1}$	$(3.49 \pm 0.14) \times 10^{-1}$
1.195	$(2.10 \pm 0.11) \times 10^{-1}$	$(2.83 \pm 0.14) \times 10^{-1}$	$(3.83 \pm 0.15) \times 10^{-1}$
1.208	$(1.84 \pm 0.09) \times 10^{-1}$	$(2.80 \pm 0.14) \times 10^{-1}$	$(3.91 \pm 0.15) \times 10^{-1}$
1.222	$(1.65 \pm 0.09) \times 10^{-1}$	$(2.55 \pm 0.12) \times 10^{-1}$	$(3.66 \pm 0.14) \times 10^{-1}$
1.235	$(1.13 \pm 0.07) \times 10^{-1}$	$(1.68 \pm 0.09) \times 10^{-1}$	$(2.82 \pm 0.12) \times 10^{-1}$
1.249	$(7.88 \pm 0.57) \times 10^{-2}$	$(1.14 \pm 0.07) \times 10^{-1}$	$(2.25 \pm 0.10) \times 10^{-1}$
1.262	$(4.62 \pm 0.41) \times 10^{-2}$	$(9.00 \pm 0.63) \times 10^{-2}$	$(1.52 \pm 0.07) \times 10^{-1}$
1.276	$(4.04 \pm 0.41) \times 10^{-2}$	$(6.71 \pm 0.57) \times 10^{-2}$	$(1.11 \pm 0.06) \times 10^{-1}$
1.289	$(1.99 \pm 0.27) \times 10^{-2}$	$(4.55 \pm 0.43) \times 10^{-2}$	$(9.17 \pm 0.57) \times 10^{-2}$
1.303	$(2.08 \pm 0.29) \times 10^{-2}$	$(3.21 \pm 0.38) \times 10^{-2}$	$(6.88 \pm 0.46) \times 10^{-2}$
1.316	$(1.79 \pm 0.27) \times 10^{-2}$	$(2.14 \pm 0.30) \times 10^{-2}$	$(5.65 \pm 0.42) \times 10^{-2}$
1.330	$(1.04 \pm 0.22) \times 10^{-2}$	$(2.55 \pm 0.35) \times 10^{-2}$	$(4.15 \pm 0.35) \times 10^{-2}$
1.343	$(9.81 \pm 2.36) \times 10^{-3}$	$(2.21 \pm 0.34) \times 10^{-2}$	$(3.25 \pm 0.31) \times 10^{-2}$

Table B.5: Unpolarised differential cross section for the $dp \to \{pp\}X$ reaction with $E_{pp} < 3$ MeV for $M_X > M_N + M_\pi$ at three deuteron beam energies, as shown in Fig. 10.3. The data are summed over the interval $0 < \theta_{\text{lab}} < 3^\circ$ in the diproton laboratory polar angle. Only statistical errors are shown. Systematic uncertainties are listed in Table 7.1.

	q_t [MeV/c]	A_{xx}	A_{yy}
1.6 GeV	23.8	0.21 ± 0.11	0.15 ± 0.12
	47.8	0.04 ± 0.09	0.20 ± 0.09
	70.2	-0.03 ± 0.09	0.10 ± 0.09
	89.8	-0.22 ± 0.09	0.17 ± 0.09
	109.4	-0.48 ± 0.12	0.31 ± 0.10
	129.3	-0.36 ± 0.16	0.32 ± 0.10
1.8 GeV	23.9	0.03 ± 0.10	0.17 ± 0.09
	48.0	0.04 ± 0.08	0.10 ± 0.07
	70.2	-0.12 ± 0.07	0.19 ± 0.07
	89.9	-0.25 ± 0.07	0.18 ± 0.07
	109.8	-0.18 ± 0.09	0.16 ± 0.07
	129.3	-0.48 ± 0.12	0.28 ± 0.09
	149.1	-0.46 ± 0.22	0.23 ± 0.14
2.27 GeV	23.5	-0.01 ± 0.13	0.05 ± 0.14
	48.0	-0.07 ± 0.10	0.31 ± 0.11
	70.2	-0.15 ± 0.10	0.04 ± 0.10
	90.0	-0.18 ± 0.10	0.22 ± 0.10
	109.8	-0.37 ± 0.10	0.15 ± 0.09
	129.6	-0.44 ± 0.10	0.20 ± 0.10
	149.3	-0.44 ± 0.14	0.30 ± 0.12
	168.9	-0.64 ± 0.24	0.52 ± 0.21

Table B.6: Acceptance-corrected tensor analysing powers A_{xx} and A_{yy} of the $\vec{d}p \to \{pp\}_s X$ reaction with $E_{pp} < 3$ MeV at three deuteron beam energies as functions of the transverse momentum transfer q_t, as shown in Fig. 10.7. Only high mass data ($1.19 < M_X < 1.35$ GeV/c^2) are considered. Though the error bars are dominantly statistical, they include also the uncertainties from the beam polarisation and relative luminosity C_n. In addition, there is an overall uncertainty of up to 4% due to the use of the polarisation export technique.

θ_π [deg]	$A_{x,x}$	$A_{y,y}$
5.5	-0.90 ± 0.08	-1.01 ± 0.10
12.5	-0.91 ± 0.07	-0.91 ± 0.07
19.5	-0.72 ± 0.07	-1.00 ± 0.07
26.5	-0.60 ± 0.10	-0.99 ± 0.07
37.5	-0.71 ± 0.19	-1.00 ± 0.09
160.5	-0.74 ± 0.22	-0.71 ± 0.12
167.5	-0.67 ± 0.14	-0.97 ± 0.10
174.5	-0.72 ± 0.20	-0.89 ± 0.15

Table B.7: The values of $A_{x,x}$ and $A_{y,y}$ measured in the $\vec{n}\vec{p} \to d\pi^0$ reaction at energies around 600 MeV as functions of the pion polar angle θ_π in the c.m. frame, as shown in Fig. 10.11. Only statistical errors are shown.

Bibliography

[1] R. A. Arndt, I. I. Strakovsky, and R. L. Workman. *Physics Review C*, 62(034005), 2000.

[2] G. Bizard et al. *Nuclear Physics B*, 85:14, 1975.

[3] J. Ball et al. *European Physical Journal C*, 5:51, 1989.

[4] I. Pomeranchuk. *Doklady Akademii Nauk*, 77:249, 1951.

[5] D. V. Bugg and C. Wilkin. *Nuclear Physics A*, 467:575, 1987.

[6] F. Lehar and C. Wilkin. *Physics of Particles and Nuclei Letters*, 7(4):235, 2010.

[7] N. W. Dean. *Physics Review D*, 5:1661, 2832, 1972.

[8] V. I. Sharov et al. *European Phusical Journal A*, 39:267, 2009.

[9] D. V. Bugg and C. Wilkin. *Physics Letters B*, 154:243, 1985.

[10] R. A. Arndt, J.S. Hyslop III, and L.D. Roper. *Physics Review D*, 35:128, 1987.

[11] B. Pagels. *Untersuchung der quasielastischen Ladungsaustauschreaktion nd $\rightarrow$ pnn im Neutronenergiebereich von 290 bis 570 MeV.* PhD thesis, Universität Freiburg im Breisgau, 1988.

[12] R.J. Glauber and V. Franco. *Physics Review*, 156:1685, 1967.

[13] F. Lehar and C. Wilkin. *European Physical Journal A*, 37:143, 2008.

[14] J. Bystrický, F. Lehar, and P. Winternitz. *Journal of Physics (Paris)*, 39:1, 1978.

[15] R.J.N. Phillips. *Reports on Progress in Physics,* 22:562, 1959;
idem Proceedings of the Physical Society A, 74:652, 1959;
idem Nuclear Physics, 53:650, 1964.

[16] G.G. Ohlsen. *Reports of Progress in Physics*, 35:717, 1972.

[17] M.W. McNaughton et al. *Physics Review C*, 45:2564, 1992.

[18] D.J. Mercer et al. *Physics Review Letters*, 71:684, 1993.

[19] H. Sakai et al. *Physics Review C*, 35:344, 1987.

[20] M.A. Pickar et al. *Physics Review C*, 42:20, 1990.

[21] M. Zeier et al. *Nuclear Physics A*, 654:541, 1999. PhD thesis, Universität Basel, 1997.

[22] P.W. Lisowski, R.C. Byrd, R.L. Walter, and T.B. Clegg. *Nuclear Physics A*, 334:45, 1980.

[23] L.P. Robertson et al. *Nuclear Physics A*, 134:545, 1969.

[24] H. Sakai et al. *Physics Letters B*, 177:155, 1986.

[25] N.W. Reay, E.H. Thorndike, D. Spalding, and A.R. Thomas. *Physics Review*, 150:806, 1966.

[26] J.S. Chalmers et al. *Physics Letters B*, 153:235, 1985.

[27] P.J. Riley et al. *Physics Letters B*, 103:313, 1981.

[28] T. Sams et al. *Physics Review C*, 51:1945, 1995.

[29] T. Motobayashi et al. *Nuclear Physics A*, 481:207, 1988.

[30] S. Kox et al. *Nuclear Physics A*, 556:621, 1993.

[31] D. Chiladze et al. *European Physical Journal A*, 40:23, 2009.

[32] D. Mchedlishvili et al. *European Physical Journal A*, 49:49, 2013.

[33] D. Adams et al. *Acta Polytechnica (Prague)*, 36:11, 1996.

[34] A. de Lesquen et al. *European Physical Journal C*, 11:69, 1999.

[35] M.W. McNaughton et al. *Physics Review C*, 53:1092, 1996.

[36] A. Ahmidouch et al. *European Physical Journal C*, 2:627, 1998.

[37] D.V. Bugg et al. *Physics Review C*, 21:1004, 1980.

[38] J. Carbonell, M.B. Barbaro, and C. Wilkin. *Nuclear Physics A*, 529:653, 1991.

[39] M.B. Barbaro and C. Wilkin. *Journal of Physics G*, 15:L69, 1989.

[40] D. Chiladze et al. *Physics Letters B*, 637:170, 2006.

[41] R. A. Arndt et al. *Physics Review C*, 50:2731, 1994.

[42] S. Barsov et al. *Nuclear Instruments and Methods A*, 462:364, 2001.

[43] R. Maier et al. *Nuclear Instruments and Methods A*, 390:1, 1997.

[44] H. J. Stein et al. Proc. 18^{th} Conf. Charged Particle Accelerators (RUPAC 2002).

[45] H. J. Stein et al. *Atomic Energy*, 94:24, 2003.

[46] D. Prasuhn et al. *Nuclear Instruments and Methods A*, 441:167, 2000.

[47] R. Weidmann et al. *Review of Scientific Instruments*, 67:1357, 1996.

[48] O. Felden et al. Proc. 9^{th} Int. Workshop on Polarized Sources and Targets, Nashville, 2001, eds. V.P. Derenchuk and B. von Przewoski, Nashville, USA, 2001, (World Scientific, Singapore, 2002) p. 200.

[49] W. Haeberli. *Annual Review of Nuclear and Particle Science*, 17:373, 1967.

[50] D. Chiladze. *Polarised Charge–Exchange Reaction $dp \to (pp)n$ Studies at the ANKE-COSY Spectrometer*. PhD thesis, Forschungszentrum Jülich, 2008.

[51] A. Lehrach et al. *AIP Conference Proceedings*, 675:153, 2003.

[52] A. Kacharava et al. *Nuclear Instruments and Methods A*, 376:356, 1996.

[53] A. Khoukaz et al. *European Physical Journal D*, 5:275, 1999.

[54] M. Mikirtychyants et al. *Nuclear Instruments and Methods A*, 721:83, 2013.

[55] R. Engels et al. *Review of Scientific Instruments*, 74(11):4607, 2013.

[56] K. Grigoryev et al. *AIP Conference Proceedings*, 915:979, 2007.

[57] K. Grigoryev et al. *Nuclear Instruments and Methods A*, 599:130, 2009.

[58] R. Engels et al. *AIP Conference Proceedings*, 980:255, 2008.

[59] M. Mikirtychyants et al. *Journal of Physics: Conference Series*, 295(012148), 2011.

[60] A. Kacharava et al. Measurement of the $\vec{d}\vec{p} \to \{pp\}_s n$ charge-exchange reaction with polarised beam and target. *COSY proposal*, (172), 2007.

[61] V. Kamerdzhiev et al. *Nuclear Instruments and Methods A*, 532:285, 2004.

[62] S. Dymov et al. *Particles and Nuclei Letters*, 1:40, 2004.

[63] S. Dymov. *Investigation of the deuteron breakup by protons of 0.6-0.9 GeV with emission of a forward proton pair.* PhD thesis, JINR Dubna, 2007.

[64] I. Fröhlich et al. *Proceedings of Science*, 076(ACAT2007), 2007.

[65] M. Lacombe et al. *Physics Letters B*, 101:139, 1981.

[66] R. A. Arndt, I. I. Strakovsky, R. L. Workman, and D. V. Bugg. *Physics Review C*, 48:1926, 1993.

[67] S. Agostinelli et al. *Nuclear Instruments and Methods A*, 506:250, 2003.

[68] S. Dymov et al. *Physics Review C*, 81(044001), 2010.

[69] B. v. Przewoski et al. *Physics Review C*, 74(064003), 2006.

[70] C. Ellegaard et al. *Physics Review Letters*, 59:974, 1987.

[71] C. Ellegaard et al. *Physics Letters B*, 231:365, 1989.

[72] T. Sams. *The nuclear spin isospin responce - The $(\vec{d},p)$ reaction at intermediate energies.* PhD thesis, Niels Bohr Institute Copenhagen, 1991. http//www.physics.dk/Sams1990.pdf.

[73] V. Dmitriev, O. Sushkov, and C. Gaarde. *Nuclear Physics A*, 459:503, 1986.

[74] K. M. Watson. *Physics Review*, 88:1163, 1952.

[75] A. B. Migdal. *Zh. Eksp. Theor. Fiz.*, 28:3, 1953.

[76] B. J. Morton et al. *Physics Review*, 169:825, 1968.

[77] Yu. Uzikov, J. Haidenbauer, and C. Wilkin. The charge-exchange reaction $dp \to \{pp\}_s N\pi$ in the Δ-isobar region. ANKE internal report 97, 2013. http//www.collaborations.fz-juelich.de/ikp/anke.

[78] D. Mchedlishvili et al. *Physics Letters B*, 2013. http://dx.doi.org/10.1016/j.physletb.2013.08.018.

[79] C. Ellegaard et al. *Physics Letters B*, 154:110, 1985.

[80] J. Banaigs et al. *Physics Letters B*, 45:535, 1973.

[81] H. P. Morsch et al. *Physics Review Letters*, 69:1336, 1992.

[82] R. Baldini Celio et al. *Nuclear Physics A*, 379:477, 1982.

[83] P. Fernández de Córdoba et al. *Nuclear Physics A*, 586:586, 1995.

[84] H. Garcilazo and T. Mizutani. πNN Systems. World Scientific, Singapore, 1990.

[85] C. Hanhart. *Physics Reports*, 397:155, 2004.

[86] A. A. Filin et al. *Physics Review C*, 85(054001), 2012.

[87] D. A. Hutcheon et al. *Physics Review Letters*, 64:618, 1990.

[88] A. K. Opper et al. *Physics Review Letters*, 91:212302, 2003.

[89] E. Aprile et al. *Nuclear Physics A*, 415:365, 1984.

[90] W. B. Tippens et al. *Physics Review C*, 36(1413), 1987.

[91] V. Shmakova et al. *Physics Letters B*, ???:???, 2013.

[92] R. Schleichert et al. *IEEE Transactions on Nuclear Science*, 50:301, 2003.

[93] A. Kacharava, F. Rathmann, and C. Wilkin. Spin physics from COSY to FAIR. *COSY proposal*, (152), 2005. arXiv:nucl-ex/0511028.

[94] D. Chiladze, A. Kacharava, and C. Wilkin. *COSY proposal*, (212), 2012.

[95] D. Mchedlishvili, S. Barsov, and C. Wilkin. Measurement of spin observables in $\vec{p}\vec{d}$ elastic and inelastic scattering with polarised beam and target at anke–cosy. *COSY proposal*, (218), 2013.

[96] M. Haji-Said et al. *Physics Review C*, 36(2010), 1987.

[97] J. Arvieux et al. *Nuclear Physics A*, 431:613, 1984.

[98] J. Arvieux et al. *Nuclear Instruments and Methods A*, 273:48, 1988.

[99] D. Chiladze et al. *Physics Review Special Topics - Accelerators and Beams*, 9(050101), 2006.